

Seismic Transport Properties of Fractured Rocks



UNIVERSITY OF
LIVERPOOL

Thesis submitted in accordance with the requirements of the
University of Liverpool for the degree of Doctor of Philosophy

by

Oshaine Omar Blake

March 2011

Dedicated to

Bernard Blake (my Dad) and Cynthia Roberts (my grandma)

Contents

LIST OF TABLES	IV
LIST OF FIGURES	V
ABSTRACT.....	XV
ACKNOWLEDGEMENTS.....	XVII
1 INTRODUCTION.....	1
1.1 NATURE OF PROBLEM.....	1
1.1.1 <i>Influence of confining pressure on seismic wave velocity</i>	1
1.1.2 <i>Mechanisms involved in attenuation</i>	4
1.1.3 <i>Static and dynamic elastic properties</i>	4
1.2 AIM.....	6
1.3 THESIS STRUCTURE.....	7
2 EXPERIMENTAL APPARATUS AND METHODS	9
2.1 INTRODUCTION	9
2.2 UNIAXIAL SAMPLE ASSEMBLY	10
2.3 HYDROSTATIC SAMPLE ASSEMBLY.....	12
2.4 PREPARATION OF SAMPLES FOR TESTING	23
2.5 ULTRASONIC MEASUREMENT SYSTEM	26
2.5.1 <i>Generation and detection of P and S waves</i>	26
2.5.2 <i>Pulser/receiver</i>	32
2.5.3 <i>Switchbox</i>	34
2.5.4 <i>Cabling</i>	35
2.5.5 <i>Data presentation</i>	35
2.6 UNDERSTANDING ULTRASONIC P AND S WAVE SIGNALS.....	36
2.6.1 <i>P and S wave signals</i>	37
2.6.2 <i>S wave misorientation</i>	46
2.6.3 <i>Elastic wave Coupling</i>	47
2.7 STATIC AND DYNAMIC ELASTIC PROPERTY MEASUREMENTS.....	49

2.8	P AND S WAVE, AND SHEAR WAVE SPLITTING VELOCITY MEASUREMENT	51
2.9	ATTENUATION MEASUREMENT	60
2.9.1	<i>The spectral ratio technique</i>	60
2.9.2	<i>The Rise Time Technique</i>	63
3	QUANTIFYING AND COMPARING THE EVOLUTION OF DYNAMIC AND STATIC ELASTIC PROPERTIES AS CRYSTALLINE ROCK APPROACHES FAILURE DURING MULTI-CYCLE UNIAXIAL LOADING	65
3.1	ABSTRACT	65
3.2	INTRODUCTION	66
3.3	METHODOLOGY	68
3.4	RESULTS	73
3.4.1	<i>Young's modulus</i>	75
3.4.2	<i>Poisson's ratio</i>	78
3.5	DISCUSSION	81
3.5.1	<i>Differences between static and dynamic elastic properties</i>	84
3.6	CONCLUSION	92
4	QUANTIFYING THE EFFECT OF VARYING DAMAGE HISTORY IN CRYSTALLINE ROCKS ON THE P AND S WAVE VELOCITIES AND ELASTIC PROPERTIES UNDER HYDROSTATIC CONFINING PRESSURE.....	93
4.1	ABSTRACT	93
4.2	INTRODUCTION	94
4.3	EXPERIMENTAL METHODOLOGY	96
4.4	RESULTS	101
4.4.1	<i>Uniaxial Compressive condition</i>	101
4.4.2	<i>Hydrostatic confining condition</i>	103
4.5	DISCUSSION	106
4.5.1	<i>The effect of P and S wave velocities and elastic properties subjected to uniaxial compressive condition</i>	106
4.5.2	<i>The effect of P and S wave velocities and elastic properties subjected to hydrostatic confining condition</i>	108

4.5.3	<i>Comparison between the effect of P and S wave velocities subjected to hydrostatic confining and uniaxial compressive condition.....</i>	<i>108</i>
4.6	CONCLUSION	110
5	ATTENUATION MEASUREMENTS OF CRYSTALLINE ROCKS UNDER HYDROSTATIC CONFINING AND UNIAXIAL COMPRESSIVE CONDITIONS	111
5.1	ABSTRACT	111
5.2	INTRODUCTION	112
5.3	EXPERIMENTAL METHODOLOGY	113
5.4	RESULTS	120
5.5	DISCUSSION	124
5.6	CONCLUSION	127
6	SUMMARY AND FURTHER WORK.....	128
6.1	SUMMARY OF RESULTS	128
6.2	IMPLICATIONS FOR USE OF SEISMIC WAVES TO ACCESS ROCK FRACTURE STATE IN THE CRUST	129
6.3	SCOPE FOR FURTHER WORK	131
7	REFERENCES.....	133
8	APPENDIX	149
8.1	ELECTRONIC COPY OF LABVIEW PROGRAM USED TO DISPLAY AND PROCESS THE RECORDED P AND S WAVE DATA.	149
8.2	ELECTRONIC COPY OF 'ISF TO CSV' CONVERSION SCRIPT.	150

List of Tables

Table 3-1. Summary of experiments.....	72
Table 4-1. Summary of experiments.....	100
Table 5-1. Summary of experiments.....	117

List of figures

Figure 1-1. Summary of the relationship between static and dynamic Young's modulus from the literature.....	6
Figure 2-1. Uniaxial sample assembly. a) Top platen (I). b) Bottom platen. c and d) Top platen (II). e) Complete uniaxial sample assembly.	11
Figure 2-2. Uniaxial apparatus	12
Figure 2-3. Schematic diagram of uniaxial apparatus.....	12
Figure 2-4. Hydrostatic sample assembly showing section through electrical feed lead-through.	14
Figure 2-5. Hydrostatic sample assembly showing section through high pressure pore fluid pipe.	15
Figure 2-6. Piezoelectric ceramic arrangements on top (a) and bottom (c) platens. b) orientation marker on top platen, d) Orientation of the polarization of S1 and S11 wave piezoelectric ceramics to the polarization of S wave piezoelectric piezoelectric ceramic.....	17
Figure 2-7. A typical section through the sample assembly inside the vessel of the hydrostatic apparatus. 1:2 scale. [after <i>Armitage</i> , 2008].....	19
Figure 2-8. Hydrostatic apparatus. a) Ultrasonic system attached. b) Side view of hydrostatic apparatus with shielding removed. c) Sample assembly in vessel.....	20
Figure 2-9. Gas booster used to supply compressed gas pore fluid to the hydrostatic flow rig	21
Figure 2-10. Schematic diagram of the hydrostatic apparatus. The dotted lines show electrical connections for control and feedback from motors and transducers. Thick solid lines show high pressure pipe system, thin solid	

lines show low pressure pipe system. Green coloured lines show the ultrasonic system (after Armitage, 2008).....22

Figure 2-11. Coring and cutting the ends of a rock sample. a) Coring drill. b) Cores from a Westerly granite sample. c) Diamond blade saw24

Figure 2-12. Squaring and surface finishing of cores. a) Grinding machine. b) Cored sample fixed in V-block. c) Radial and axial strain gauge glued to core.25

Figure 2-13 Schematic of piezoelectric ceramic for compression(a) and shear waves (b) (after Strassburger, 1982)27

Figure 2-14. Piezoelectric ceramic, backing and copper sheet arrangement. a) Cut into halves b) Cut into thirds.....29

Figure 2-15. The effect of backing material on piezoelectric ceramics signals. Computer simulated piezoelectric ceramic signals with backing material of different elastic wave impedance: a) frequency response of the piezoelectric ceramic; b) transient response of the piezoelectric ceramic. $Z_P = 28 \text{ MRayl}$. Z_P is the elastic wave impedance of the piezoelectric ceramic, Z_B is the elastic wave impedance of the backing material (after Safari and Akdoğan, 2008). c) Measured signal through mild steel sample using the through-transmission method. P-P refers to pulsing with the P wave piezoelectric ceramic and receiving with another P piezoelectric ceramic and S-S refers to pulsing with S wave piezoelectric ceramic and receiving with another S wave piezoelectric ceramic. The red rectangles highlights the wave train of the P and S wave arrivals. Fast Fourier transform of the wave trains are shown to the right. The elastic wave impedance of both the backing material and piezoelectric ceramic is $\sim 29.7 \text{ MRayls}$31

Figure 2-16. A highly simplified circuit representation of a “spike” pulser/receiver (after Schmerr Jr and Song, 2007).....33

Figure 2-17. Signal-to-noise ratio improvement by summing or ‘stacking’ ultrasonic waves using a Tektronix TDS 3032B oscilloscope. a) A single

signal. b) Stacking 4 signals. c) Stacking 32 signals. d) Stacking 512 signals. The P wave arrival is clearly seen in (d) after 21 μ s.34

Figure 2-18. P or S wave arrival. The polarity of the first maximum is dependent on the pulser wave input. The polarity of the first maximum of S wave arrival is also dependent on the angle between the polarization direction of the pulsing S wave piezoelectric ceramic and the polarization direction of the receiving S wave piezoelectric ceramic.36

Figure 2-19. P and S wave arrangement on both ends of the mild steel sample.....40

Figure 2-20. Mild steel sample placed in the ultrasonic measurement system. The dimensions of the sample adhered to the standard for using ultrasonic testing to determine pulse velocities (ASTM, 1997a). The sample was designed to fit in a standard uniaxial compressional apparatus.40

Figure 2-21. Recorded waveforms from measurements made on a mild steel sample that adhered to the ASTM standards (ASTM, 1997a). The arrows indicate the first deflection of the P or S wave arrival. The hatched area represents the region of uncertainty in picking the S wave arrival. a) P-P trace. b) P-S trace. c) S-P trace. d) S-S trace41

Figure 2-22. Typical pulser/receiver settings that give an excellent excitation and reception of the piezoelectric ceramics.42

Figure 2-23. 17-4 PH (chromium-copper precipitation hardening) stainless steel sample (part A and part B) placed in the ultrasonic measurement system. The dimensions of the sample do not adhere to the standard for using ultrasonic testing to determine pulse velocities (ASTM, 1997a). The sample was designed to fit in a standard uniaxial compressional apparatus. The fundamental frequency of the piezoelectric ceramics are 1MHz.....42

Figure 2-24. Recorded waveforms from measurements made on a 17-4 PH stainless steel sample that falls outside of the ASTM standards (ASTM, 1997a) and without backing material on the piezoelectric ceramic.

Impedance mismatch between the 75 ohm high frequency cable and the pulser/receiver (50 ohm) was present in the ultrasonic measurement system. The arrows indicate the first deflection of the P or S wave arrival. The hatched area represents the region of uncertainty in picking the S wave arrival.....43

Figure 2-25. Mild steel sample cut into two (a) and 4 (b). Top platen (I) and top platen (II) are components of the uniaxial apparatus.....44

Figure 2-26. P-P traces (left) and S-S traces (right) of the mild steel uncut, cut into two parts, and cut in four parts.45

Figure 2-27. Amplitude of the first maximum of P and S wave arrival during rotation of the top platen (I) and keeping the bottom platen fixed. Misorientation is the angle between the polarization direction of the pulsing S wave and the polarization direction of the receiving S wave.....46

Figure 2-28. Couplant (right) vs no couplant (left) of signals from the top platen (I) and bottom platen. The couplant used is multi-purpose grease. An axial load of 70KN was applied to the top platen (I) and bottom platen.48

Figure 2-29. Full Wheatstone Bridge configuration for axial and radial strain measurement.....50

Figure 2-30. Platen region of interest of the uniaxial sample assembly. Mild steel sample of the same deminsion as the test samples is placed between the top (I or II) and bottom to account for changes in the length of the region of interest as a function of differential stress.52

Figure 2-31. P and S wave travel times through the top platen (I) and bottom platen as a function of differential stress.....52

Figure 2-32. P and S wave travel times throught the top platen (II) and bottom platen as a function of differential stress.53

Figure 2-33. P and S Travel time through the top and bottom platens as a function of confining pressure.53

Figure 2-34. Schematic illustration of shear-wave splitting in stress-aligned54

Figure 2-35. S wave piezoelectric ceramics arrangement for shear wave splitting measurement. Pulse with S wave piezoelectric ceramic on bottom platen. Receive with S1 and S11 piezoelectric ceramics on top platen (II)...55

Figure 2-36. S-S traces of shear wave splitting of mylonitic gneiss 1B. The waveform changes as the sample is rotated between 0° and 180°. The fast S wave (S1) can be accurately picked at the first deflection. The slow S wave (S2) can be picked at the first maximum. In some traces the fast or slow wave is within the noise level and cannot be seen.56

Figure 2-37. S-S traces of shear wave splitting of mylonitic gneiss 2B. The waveform changes as the sample is rotated between 0° and 180°. The fast S wave (S1) and slow S wave (S2) can be accurately picked at the first deflection. In some traces the fast or slow wave is within the noise level and cannot be seen.....57

Figure 2-38. S-S traces of shear wave splitting of mylonitic gneiss 3B. The waveform changes as the sample is rotated between 0° and 180°. The fast S wave (S1) can be accurately picked at the first deflection. The slow S wave (S2) can be picked at the first maximum.58

Figure 2-39. Shear wave splitting of Westerly granite with microcracks oriented parallel to the axial loading direction. S-S1 traces are on the left. S-S11 traces are on the right. The Westerly granite sample with induced microcrack damage was taken up to 88MPa differential stress. The hatched area represents the region of uncertainty in picking the slow S wave arrival. The difference between the fast and slow wave arrival times increases as the differential stress increases.....59

Figure 2-40. Attenuation characteristics of the sample and reference at different hydrostatic confining pressure. Left: The magnitude of the fast Fourier transform of the first 2 periods of the P (a) and S wave (c) arrivals. Right: The spectral amplitude ratio of the reference to the sample of the P (b) and S wave (d). The linear portion is taken between 0.8MHz to 1.7MHz where a linear least square fit line is drawn through the data points. This verifies the linearity assumption made in the calculation.62

Figure 2-41. The rise time, τ , of a typical wave. (after Gladwin and Stacey, 1974)63

Figure 3-1. Schematic diagram of experimental arrangement (a), and arrangement of P and S wave piezoelectric ceramic within the loading top and bottom platens (b).....68

Figure 3-2. P and S wave arrival of sample WG-SDD. a) recorded trace when pulsing with P wave piezoelectric crystal and receiving with an identical P wave transducer located on the other side of the sample. b) trace obtained pulsing with S wave piezoelectric crystal and receiving with S wave transducer.72

Figure 3-3. Stress-strain curve (a) and P (b) and S wave velocity (c) of sample WG-SDD under increasing-amplitude cyclic loading experiments. Green arrows indicate the change in radial, volumetric and axial strains and P and S wave velocity as the cycle number increases. Volumetric strain = axial strain + (2*radial strain). Solid and dotted lines represent loading and unloading respectively. The P and S wave velocity measurement error is less than 0.3%. The approximate positions of the stages of crack development in brittle rock under uniaxial compression (Bieniawski, 1967a; Bieniawski, 1967b; Bieniawski, 1967c; Brace et al., 1966) are shown in (d) along with schematic illustration of crack orientation and growth.....74

Figure 3-4. Area bounded by the loading and unloading velocity, from 3MPa to 107MPa differential stress, as a function of number of cycles. The area depicts microfracture damage.75

Figure 3-5. Static and dynamic Young’s modulus evolution with increasing differential stress (a, c) and number of cycles (b, d) of sample WG-SDD. The static Young modulus is compared to the dynamic Young’s modulus (e, f). The dash line represents line of equality.....77

Figure 3-6. Variation of the linear relationship parameters as a function of cycles.....78

Figure 3-7. Static and dynamic Poisson’s ratio evolution with increasing differential stress (a, c) and number of cycles (b, d) of sample WG-SDD. The static Poisson’s ratio is compared to the dynamic Poisson’s ratio (e, f). The dash line represents line of equality.80

Figure 3-8. Photomicrographs of Westerly granite under cross-polarized light. (a) undeformed sample. (b) deformed sample. (c) and (d) magnified photomicrographs of deformed sample showing large intragranular and transgranular microcracks in grains of quartz. Thin sections were taken along the YZ plane (parallel to loading direction). IG—intragranular microcrack; TG—transgranular microcrack (after Heap and Faulkner, 2008).82

Figure 3-9. (a) Summary of the relationship between static and dynamic Young’s modulus from the literature and present study. (b) Change in the present study’s static vs. dynamic Young’s modulus due to stress dependency and microcrack damage. The red arrow indicates the direction of change due to increasing differential stress and the black arrow indicates the direction of change due to increasing microcrack damage (from cycle 1 to cycle 5).....85

Figure 3-10. Bulk modulus obtained from high frequency velocities inversion and low frequency oscillation tests (after Adelinet et al., 2010). Effective pressure = confining pressure – pore pressure. The pore pressure is fixed to 10 MPa.87

Figure 3-11. Strain gauge position on long sample89

Figure 3-12. Static Poisson’s ratio as a function of differential stress at different locations on the long sample.....90

Figure 3-13. Static vs dynamic Poisson’s ratio at different locations on the long sample. The dash line represents line of equality.91

Figure 4-1. Schematic diagram showing the effect of confining pressure on elastic wave velocity.94

Figure 4-2. Schematic diagram of the uniaxial (a) and hydrostatic (b) experimental setup97

Figure 4-3. Typical P and S wave arrivals (from sample WGA). Top: Pulsing with P wave piezoelectric ceramic and receiving with P piezoelectric ceramic trace. Bottom: Pulsing with S piezoelectric ceramic and receiving with S piezoelectric ceramic trace. Excitation pulse is at 0 μ s.100

Figure 4-4. P (a) and S wave (b) velocities, their ratio (c), Young’s modulus (d) and Poisson’s ratio (e) with increasing differential stress. Solid and dashed lines represent loading and unloading respectively of samples. Sample variability is seen in the loading data. Sample WGUH1, WGUH2, WGUH3, and WGUH4 was taken to 60%, 70%, 80% and 90% respectively of the UCS.102

Figure 4-5. Summary of results showing normalized parameters as a function of microcrack damage. Z is the P or S wave velocity, V_p/V_s , Young’s modulus, or Poisson’s ratio at a given damage level. Z_0 is the P or S wave velocity, V_p/V_s , Young’s modulus, Poisson’s ratio at an initial damage level. The initial damage is the microcrack present in the sample before any other microcracks were induced. These parameters were taken at 66MPa differential stress during uniaxial compression.103

Figure 4-6. P (a) and S wave (c) velocity, their ratio (g), Young’s modulus (e) and Poisson’s ratio (h) with increasing confining pressure. Errors in velocity are estimated from repetition of measurements from samples without induced microcrack damage (WGA, WGB, and WGD). The P and S wave

velocities and Young's modulus of the samples with induced microcrack damage are normalized to the P and S wave velocities and Young's modulus of the samples without microcrack damage (b, d, and f).....105

Figure 4-7. Summary of results showing normalized parameters as a function of microcrack damage for: (left) present study; and (right) data from chapter 3. Z is the P or S wave velocity, V_p/V_s , Young's modulus, or Poisson's ratio at a given damage level. Zo is the P or S wave velocity, V_p/V_s , Young's modulus, Poisson's ratio at an initial damage level. The initial damage is the microcrack present in the sample before any other microcracks were induced. These parameters were taken at 66MPa differential stress during uniaxial compression.107

Figure 4-8. P (b) and S wave (c) velocities as a function of mean stress. Solid lines represent loading of sample under uniaxial compressive conditions. Dotted lines represent unloading of samples under uniaxial compressive conditions. Dashed lines represent pressurization of sample under hydrostatic confining conditions. Also shown are the approximate positions of the stages of crack development in brittle rock under uniaxial compression. (after Bieniawski, 1967a; Bieniawski, 1967b; Bieniawski, 1967c; Brace et al., 1966). (a) the schematic illustration of crack orientation and growth are referred to a sample that has been through all the stages involved in the brittle failure of rocks (e.g. WGUH4)109

Figure 5-1. Schematic diagram of the hydrostatic (a) and uniaxial (b) experimental setup114

Figure 5-2. P and S wave arrival of sample WGA. Top: Pulsing with P wave piezoelectric ceramic and receiving with P piezoelectric ceramic trace. Bottom: Pulsing with S piezoelectric ceramic and receiving with S piezoelectric ceramic trace. Excitation pulse is at 0 μ s.116

Figure 5-3. Attenuation characteristics of the sample and reference at different hydrostatic confining pressure. Left: The magnitude of the fast Fourier transform of the first 2 periods of the P (a) and S wave (c) arrivals.

Right: The spectral amplitude ratio of the reference to the sample of the P (b) and S wave (d). The linear portion is taken between 0.8MHz to 1.7MHz where a linear least square fit line is drawn through the data points. This verifies the linearity assumption made in the calculation. 119

Figure 5-4. P (a) and S wave (c) velocities and attenuation (b and d) as a function of confining pressure. Errors are calculated from repetition of measurements from samples WGA, WGB, and WGD..... 121

Figure 5-5. P (a) and S wave (c) velocities and attenuation (b and d) of sample WG-SDD under increasing-amplitude cyclic loading . The unloading measurements are shown..... 122

Figure 5-6. Normalized parameters as a function of number of cycles. Z is the P or S wave velocity, or P or S wave Q factor at a given cycle number. Zo is the P or S wave velocity, or P or S wave Q factor at the first cycle. These parameters were taken at 58MPa differential stress. 123

Figure 8-1. Example of a batch file. A text editor (Notepad or Wordpad in Windows) can be used to create the batch file. The file extension of the file should be saved as .bat..... 151

Abstract

Fracture in rock is a major factor that affects the rock's physical properties and it also provides the route for the passage of fluids that can transport potentially hazardous substances and hydrothermal fluids. Assessment of the degree of fracture in rocks is important as they play an essential role in many geomechanical issues (stability of boreholes, stimulation of oil and geothermal reservoirs, the design of civil structures, tunnels and hazardous waste disposals), and in understanding a number of processes in the Earth's crust such as magmatic intrusions, plate tectonics, fault mechanics and sedimentary basins. The fundamental understanding of how seismic waves are altered when they pass through fractured rock are currently poorly understood, hence a comprehensive study is timely. An improved understanding of how fractures affect the physical properties (such as seismic velocity and attenuation) would significantly enhance our ability to predict the fracture state of rock at depth remotely. The main focus of this thesis is to characterize P and S wave velocity, their ratio, shear wave splitting and attenuation and their dependence on the fracture density of the rock. Laboratory experiments were carried out in uniaxial compressive condition to increase microfracture density and hydrostatic confining condition to close microfractures. Experiments were performed on a single rock type (Westerly granite) to keep the mineralogy, chemical composition, and grain size constant. The condition of the microfractures was dry to remove the complexity of saturation and fluid type. Through transmission technique was used to measure P and S wave velocities and spectral ratio technique was used to measure attenuation. P and S wave velocities were measured at 1.5MHz. Attenuation measurements were made in the frequency range of 0.8MHz to 1.7MHz.

Elastic properties can be measured statically where strain data are recorded and related to stress during slow loading of a specimen, or dynamically, where the elasticity can be calculated from the velocity of P and S waves. In order to understand the elastic properties of the crust at depth using seismology, the relationship between the static and dynamic properties must be known. Increasing-amplitude, uniaxial cyclic loading experiments were carried out to investigate and quantify the effect of microcracking on the elastic properties, and to establish a relationship between static and dynamic measurements. There is a linear relationship between static and dynamic Young's moduli, and a significant discrepancy between the static and dynamic Poisson's ratio. We attribute the differences in the static and dynamic elastic properties to the size distribution of the crack population relative to the amplitude and frequency of the applied stress, frictional sliding on closed cracks during loading/unloading, and the assumption of isotropic elasticity in the sample.

Strong stress-dependency exists in the uniaxial compressive and hydrostatic confining conditions due to closure of microcracks. This resulted in: an increase in the P and S wave velocities, their ratio, static and dynamic Young's modulus, and static and dynamic Poisson's ratio; and a decrease in the P and S wave attenuation. The increase of fracture density caused: a decrease in the P and S wave velocities and static and dynamic Young's modulus; a small increase in the dynamic Poisson's ratio and V_p/V_s ; and a large increase in the static Poisson's ratio, and P and S wave attenuation. Seismic wave attenuation is more sensitive

than seismic wave velocity to closure of microcracks and increase of microfracture density.

The effect of varying crack density on the P and S wave velocities and elastic properties under confining pressure (depth) were quantified. The elastic wave velocities and Young's modulus of samples that have a greater amount of microcrack damage required higher confining pressure to be equal to those of samples with no induced microcrack damage. We found that fractures are completely closed at ~5km (~130MPa) in crystalline rocks. At shallow depth (less than 5km), fracture density affects seismic wave velocities. We observed an overall 6% and 4% reduction in P and S wave velocities respectively due to an increase in the fracture density. The overall reduction in the P and S wave decreased to 2% and 1% at ~2km. Consequently, assessing the degree of fracture between 2km and 5km using seismic wave velocities may be difficult.

Acknowledgements

First and foremost, thanks to God for giving me strength, wisdom, knowledge and good health, and for guidance and protection, keeping me focus, determined and patient.

I would like to express my deep and sincere gratitude to my supervisors, Daniel Faulkner and Andreas Rietbrock. I am deeply grateful to Daniel Faulkner for giving me this one in a life time opportunity, being very supportive, helping me to secure funding to carry out this research, building my general and high pressure laboratory technical skills, and teaching me the fundamentals of Rock Deformation. I would like to thank Andreas Rietbrock for detailed and constructive comments, important support throughout this research, and for teaching me the necessary geophysical aspects of this research.

I would like to thank the University of Liverpool for offering me the Dorothy Hodgkin Postgraduate Award (DHPA). It would have been impossible to carry out this research without the DHPA.

During this research I was not able to physically see my Mom (Sandra), brothers (Shomari and Okeno) and sister (Sadrika) because of unforeseen circumstances. I deeply miss them. I must admit that it has been extremely difficult not being with them, but the love, togetherness, and friendship we have for each other carried me through. Thanks to them for being 100% supportive and encouraging in all possible ways, understanding, optimistic, strong and making me the person I am today. I have to give a special thanks to my Aunt Elaine for constant encouragement and support before, during, and even after this research.

The Rock Deformation Laboratory has an excellent work atmosphere. I would like to thank the following members for proving such environment and for helping me with the many technical difficulties I encountered: Pete, Tom, Sergio, Julia, Shanvas (for also being a superb flat-mate and friend), Dan T, Betty, Graham and Cristina. Thanks to the dedicated staffs in the Earth and Ocean Sciences department for always having the time to help me with administration

matters. Thanks to all the friends I made in the department that gave encouragement and support throughout this research including Dave Prior, Rich Worden, Stewart, Eddie, Ceri, Mohammed (Bukar and Shatwan), and Salah. A massive thanks to Dave Hodgson for informing and helping me to successfully apply for the EPSRC PhD Plus Scheme 2010-2011.

I am deeply grateful to my undergraduate supervisor Keith Miller for being very supportive. Thanks to Stephen Kewin from CAE engineering for advice in the design and accurate manufacturing of the apparatus used in this research. I would also like to thank Rochelle from University of Manchester for constructive discussions and collaboration.

‘All work and no play makes Jack a dull boy’. Thanks to Sadiki, Trevor, Mobrie, Alexandra, Francia, Keisha and Elvis for encouragement during the research and social life support. Thanks to all the guys I played football with, especially to the Earth Science football team.

Finally, I offer my regards and blessings to all of those who supported me (including a few people that I forgot to mention) in any and every aspect during the research.

1 Introduction

1.1 Nature of problem

Fracture in rock is a major factor that affects the rock's physical properties and it also provides the route for the passage of fluids that can transport potentially hazardous substances and hydrothermal fluids. Assessment of the degree of fracture in rocks is important as they play an essential role in many geomechanical issues (stability of boreholes, stimulation of oil and geothermal reservoirs, the design of civil structures, tunnels and hazardous waste disposals), and in understanding a number of processes in the Earth's crust such as magmatic intrusions, plate tectonics, fault mechanics and sedimentary basins. The fundamental understanding of how seismic waves are altered when they pass through fractured rock are currently poorly understood, hence a comprehensive study is timely. An improved understanding of how fractures affect the physical properties (such as seismic velocity and attenuation) would significantly enhance our ability to predict the fracture state of rock at depth remotely. The main focus of this thesis is to characterize P and S wave velocity (referred to as V_p and V_s respectively), their ratio, shear wave splitting and attenuation and their dependence on the fracture density of the rock.

1.1.1 Influence of confining pressure on seismic wave velocity

Seismic wave velocity is affected by many factors, such as fractures (or cracks), pressure, temperature, degree of saturation, fluid type, porosity, and density. These factors are often interrelated or coupled in a way that a change in one factor results in a change in many other factors. Consequently, investigation of the effect of varying a single parameter while fixing the others becomes imperative in understanding how seismic waves propagate through rocks. Laboratory studies, a few which are outlined briefly below, have shown how P and S wave velocities vary when increasing confining pressure are applied to rocks. Many researchers measured the velocities of different rock samples, that contain unknown amounts of microcracks and different microstructure, at elevated confining pressure (Benson et al., 2005; Benson et al., 2006a; Benson et al., 2006b; Birch, 1960; Birch, 1961; Christensen, 1965; Christensen, 1974;

Christensen and Wang, 1985; Kern, 1978; Kern, 1990; Kitamura et al., 2010; Nur and Simmons, 1969; Peacock et al., 1994; Schubnel et al., 2006; Simmons, 1964; Wang and Ji, 2009). However, there is not much information about the effect of confining pressure on the P and S wave velocities of rocks that contain a controlled amount of microcrack damage.

Birch (1960) measured P wave velocities for some 250 rock specimens, mainly igneous and metamorphic rocks, up to 1GPa confining pressure at room temperature (between 20° and 30°) and found that the P wave velocities increases rapidly in a nonlinear manner below a critical point, referred to as the crack-closing pressure, as the confining pressure increases. The degree of saturation within the rock samples was not specified.

Nur and Simmons (1969) measured P and S wave velocity in granitic and limestone rocks up to 400MPa confining pressure. The authors found that fluid in microcracks in rock increases the P-wave velocities, whereas S-wave velocities remain unchanged which results in a higher V_p/V_s and Poisson's ratio than in dry rocks. The strong dependence of velocity on pressure and saturation is confined to low effective pressure (below 100MPa or 200MPa and without pore pressure).

Kern (1978) measured P wave velocities in granite, amphibolites, and peridotite specimens under conditions of high temperature up to 700°C and confining pressure up to 600MPa and found that the P wave velocities increase with pressure, in a similar manner as Birch (1960), and decrease with temperature. The general decrease in P wave velocities with increasing temperature is mainly due to grain-boundary opening and cracking and expansion of the constituent minerals (David et al., 1999; Heuze, 1983; Kern, 1978; Nasser et al., 2007).

Christensen and Wang (1985) measured P and S wave velocities of water saturated Berea sandstone as a function of confining and pore pressures up to 200MPa and found that the Poisson's ratio is anomalously high (greater than 0.3) for high pore pressure. The authors demonstrated that, at a given confining

pressure, the S wave velocity is more sensitive to increased pore pressure than is the P wave velocity, thereby causing increases in V_p/V_s and Poisson's ratio.

Peacock et al. (1994) induced permanent strain in Carrara marble specimens by stressing them above their yield point under confining pressure of 65 MPa and measured P and S wave velocities at confining pressures up to 60 MPa. The authors found that the sensitivity of velocity to confining pressure is greater for higher permanent strain samples.

Benson et al. (2005) measured permeability, porosity and P and S wave velocities simultaneously at confining pressures up to 100 MPa for a tight sandstone (Crab Orchard) and a high-porosity sandstone (Bentheim), and found that for the Crab Orchard sandstone the P and S wave velocities increased, and the permeability and porosity decreased with increasing confining pressure. The authors also found that the structural anisotropy formed by the void space is well described by P and S wave velocities anisotropy. The P and S wave velocities anisotropy of the Crab Orchard sandstone decreased with increasing confining pressure. For the Bentheim sandstone, the P and S wave velocities also increased, and the porosity and P and S wave velocities anisotropy also decreased with increasing confining pressure but the relative changes are less compared to those of the Crab Orchard sandstone. There was little variation of permeability with increasing confining pressure. The measurements were related to the contrasting pore fabric between the two rock types.

Kitamura et al. (2010) reported a notable relationship between V_p/V_s and the permeability of porous fault-related rocks by simultaneous measurement of V_p , V_s and permeability under increasing effective confining pressure up to 25 MPa. The rock samples, sandstones and silty sandstones, came from between 482 and 1316 m depth near the Chelungpu fault that was responsible for the Chi-Chi earthquake in 1999. The V_p and V_s for all samples increased with effective confining pressure in the range up to 20 MPa, then were nearly constant as effective confining pressure increased to 25 MPa.

1.1.2 Mechanisms involved in attenuation

Attenuation of seismic waves is strongly affected by the presence of cracks. Consequently, measuring attenuation may give additional information the fracture state of rocks at depth. Numerous mechanisms responsible for attenuation have been proposed. These mechanisms include: Frictional dissipation due to sliding on crack surfaces and grain boundaries (Gordon and Davis, 1968; Lockner et al., 1977; Walsh, 1966); scattering, a geometrical effect, where energy is loss from the interaction of seismic wave with cracks and pores; viscosity of saturating fluids, where attenuation peaks due to viscous relaxation developing at frequencies dependent both on pore geometry and fluid viscosity (Kuster and Toksöz, 1974; Solomon, 1973; Walsh, 1968; Walsh, 1969); inertial (Biot, 1956a; Biot, 1956b) and squirting flow (Mavko and Nur, 1975; O'Connell and Budiansky, 1977a) of saturating fluids, where fluid flow between pores induced by seismic waves resulting in attenuation. The quality factor, Q , which is dimensionless, is used as a measure of attenuation. Thus, the Q factor is a sensitive parameter for understanding the ability of the rock to transport seismic waves. The higher the Q factor, the less attenuating the rock is. The range of Q factor values in crystalline rocks from laboratory and seismic experiments is inadequate because of the difficulties involve in measuring it. Moreover, a knowledge of Q factor in crystalline rocks is important because the use of high-resolution seismic methods is becoming increasingly common such rocks for engineering, environmental and mining purposes (Juhlin, 1995; Milkereit et al., 1994).

1.1.3 Static and dynamic elastic properties

Laboratory measurements from available cores and in situ loading test such as flat jack (Loureirópinto, 1986), Goodman jack (Heuze, 1984) and plate bearing (Coulson, 1979) tests are carried out to obtain the static elastic properties. The static elastic properties of rocks are generally obtained from the linear region of the stress-strain curve. Elastic properties can also be derived from the travel time of seismic or acoustic waves. This method gives the dynamic elastic properties. However, the dynamic elastic properties are different from the static elastic properties. The difference between the static and dynamic

elastic properties results from the presence of cracks (Cheng and Johnston, 1981; King, 1983; Zisman, 1933), and the difference in the frequency of the measurements and the strain amplitude used in the experiments (Batzle et al., 2006; Tutuncu et al., 1998). Many studies aimed at establishing a relationship between both properties have been reported in the literature (King, 1983; Mockovčiaková and Pandula, 2003; Vanheerden, 1987; Wang, 2000). Here, the relationships are derived from uniaxial experiments on a range of rock types with different elastic properties. The relationship between static and dynamic Young's modulus is summarized in Figure 1-1. Investigations of the dynamic Poisson's ratio are rare due to the difficulties in determining the shear wave velocity. Consequently, very limited data relating the static and dynamic Poisson's ratio have been published.

It is well established that elastic properties are influenced by crack damage and state of stress within a rock (Eberhardt et al., 1999; Faulkner et al., 2006; Lau and Chandler, 2004; Martin and Chandler, 1994; O'Connell and Budiansky, 1974; Walsh, 1965a). However, there exist very limited data on the relationship between the static and dynamic elastic properties as a function of crack density. Furthermore, the static response of rocks to large scale stresses can be quite different from that estimated by the seismic measurements and should be investigated further (Ciccotti and Mulargia, 2004).

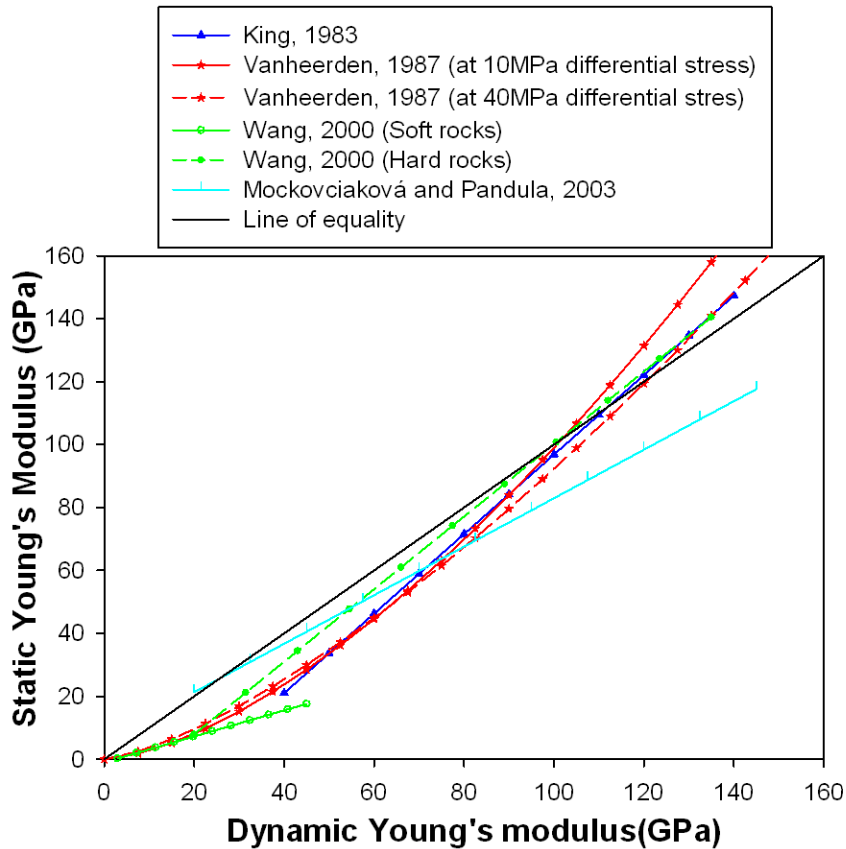


Figure 1-1. Summary of the relationship between static and dynamic Young's modulus from the literature.

1.2 Aim

In this research study, laboratory measurements of P and S wave velocity, shear wave splitting, attenuation and static elastic properties will be made as a function of microfracture density. Increasing-amplitude cyclic loading experiments will be carried out to remove the effect of stress on the parameter being measured. Consequently, the parameters will then be related to the microfracture damage. Experiments will only be performed on a single rock type (Westerly granite) to keep the mineralogy, chemical composition, and grain size constant. The condition of the microfractures will be dry to remove the complexity of saturation and fluid type. The P and S wave measurements required the development of an ultrasonic measurement system and sample assemblies that facilitates accurate and reliable measurements at low and high pressures.

The thesis will specifically address the following:

- Extend the study of Heap and Faulkner (2008) by measuring the static and dynamic elastic properties simultaneously during cyclic loading of crystalline Westerly granite. Hence the evolution of both elastic properties as the sample approaches failure can be quantified, and a relationship between both elastic properties can be established as function of microfracture density.
- Investigate the effect of confining pressure (depth) on the P and S wave velocities and dynamic elastic properties in variably controlled fractured rocks. Microfractures will be induced in a suite of samples using a standard uniaxial press, where the samples are compressed unconfined ($\sigma_2=\sigma_3=0$) between a fixed rigid plate and a manually controlled moving hydraulic piston.
- Quantify the changes in P and S wave attenuation due to frictional dissipation and scattering as: (1) fractures are induced in rock samples and (2) samples are subjected to confining pressure up to 200MPa.

1.3 Thesis structure

The core of the thesis (chapters three to five) is presented as journal papers and this necessarily involves some repetition of material as key concepts are re-introduced in places. These chapters have their own abstract, introduction, results, discussion and conclusion. For brevity, all references have been combined in a single section at the end of the thesis.

After this introductory chapter, chapter two describes the apparatus, techniques and methodology used in this thesis. The technical specifications and

design of the sample assemblies and ultrasonic measurement system are discussed. The preparation of samples that are used for testing is also outlined.

Chapter three presents the results and discussion on the evolution of static and dynamic elastic properties as crystalline rocks approaches failure. This is written in the style of a paper for submission to an international journal (Geophysical Journal International).

Chapter four presents the results and discussion on the effect of confining pressure (depth) on the P and S wave velocities and dynamic elastic properties in variably controlled fractured rocks. This is written in the style of a paper for submission to an international journal (Pure and Applied Geophysics).

Chapter five presents the results and discussion on the changes in P and S wave attenuation as: (1) fractures are induced in rock samples and (2) samples are subjected to confining pressure up to 200MPa. This is written in the style of a paper for submission to an international journal.

Chapter six presents a brief discussion and conclusion relating to all the previously discussed results, and proposes suggestion for further work.

2 Experimental Apparatus and methods

2.1 Introduction

This chapter describes the apparatus techniques and methodology used in this thesis. Two sample assemblies (uniaxial and hydrostatic) were constructed, based on designs from Dr. Daniel Faulkner, to measure P and S wave velocity and attenuation as a function of fracture density and frequency of the seismic wave. It took ~2 ½ years to design, calibrate, and commission both apparatus. The uniaxial apparatus is capable of loading a sample up to 294.3kN and measuring P and S wave velocities (from which the dynamic elastic properties can be derived), P and S wave attenuation and static elastic properties (which are obtained from stress and strain data) simultaneously. The hydrostatic apparatus is capable of measuring P and S wave velocities and attenuation up to 200MPa confining pressure. Pore fluid can also be introduced into the sample up to a pressure of 80MPa. The hydrostatic apparatus has a pore fluid system capable of measuring ultra-low permeability ($\sim 10^{-23} \text{m}^2$). Both apparatus perform experiments at room temperature. The data produced from these apparatus can be directly applied to current research in fault mechanics, volcano tectonics that features a cyclic pressurization, sedimentary basins, carbon capture and sequestration, and geomechanical issues (such as stimulation of oil and geothermal reservoirs, the design of civil structures, tunnels and hazardous waste disposals)

Firstly, this chapter discusses the technical specifications and design of the uniaxial and hydrostatic sample assemblies. Secondly, it discusses the ultrasonic system used to generate and receive P and S waves. Thirdly, the preparation of samples that are used for testing is outlined. Fourthly, it highlights the characteristics of ultrasonic P and S wave arrivals, and the effects of acoustic couplants and misorientation of the pulsing and receiving S wave polarization direction. Finally, the measurement of static and dynamic elastic properties, P and S wave velocities, shear wave splitting, attenuation, are discussed.

2.2 Uniaxial sample assembly

The sample assembly (Figure 2-1) consists of three main parts: top platen (I), top platen (II), and bottom platen. The dimensions of the parts adhered to the standard for using ultrasonic testing to determine pulse velocities (ASTM, 1997a) (see Section 3.6.1). The top platen (I) and bottom platen have a P wave piezoelectric ceramic and a S wave piezoelectric ceramic glued to them using silver-loaded epoxy adhesive (from RS Components Ltd, UK) which has a strong mechanical bonding, excellent electrical conductivity, and quick room-temperature curing. Silver-loaded epoxy was also used to fix a backing material and copper sheet to the piezoelectric ceramic (See section 3.5.1). Top platen (II) has a P wave piezoelectric ceramic and two S wave piezoelectric ceramics with backing material and copper sheet. The polarization direction of the two S wave piezoelectric ceramics (S1 and S11) is orthogonal to each other (Figure 2-1c). If the top platen (II) is at the 0° position to the bottom platen, the polarization direction of the S1 wave piezoelectric ceramic is in the same plane as the polarization direction of the S wave piezoelectric ceramic, while the polarization direction of the S11 wave piezoelectric ceramics is at 90° to the polarization direction of the S wave piezoelectric ceramic. This arrangement makes it easier to measure P and S wave velocity, and shear wave splitting simultaneously (see Section 3.8). The bottom platen is used with either of the top platens (I or II). The test sample sits between the platens.

The uniaxial sample assembly is placed in a standard uniaxial press where the sample is compressed unconfined ($\sigma_2 = \sigma_3 = 0$) between a fixed rigid plate and a manually controlled moving hydraulic piston (Figure 2-2 and Figure 2-3). The hydraulic piston is controlled by a hand operated valve pump. Axial and radial strain gauges, wired in a Wheatstone configuration which utilized a dummy sample, are used to monitor the static elastic properties of the test sample (see section 3.7). A high accuracy load cell (Tedea-Huntleigh compression load cell, model 220, grade C4) is used to measure the applied load. The maximum capacity of the load cell is 294.3kN. The strain gauge and load cell signals are fed to a RDP modular 600 multi-channel signal conditioning system that has RDP 611 strain gauge transducer amplifiers. The amplified signals are then

recorded continuously by the computer. The resolution of the strain gauge and load cell measurements is ± 0.000005 and $\pm 0.0075\text{KN}$ respectively. An ultrasonic system, discussed in section 3.5, is attached to the sample assembly.

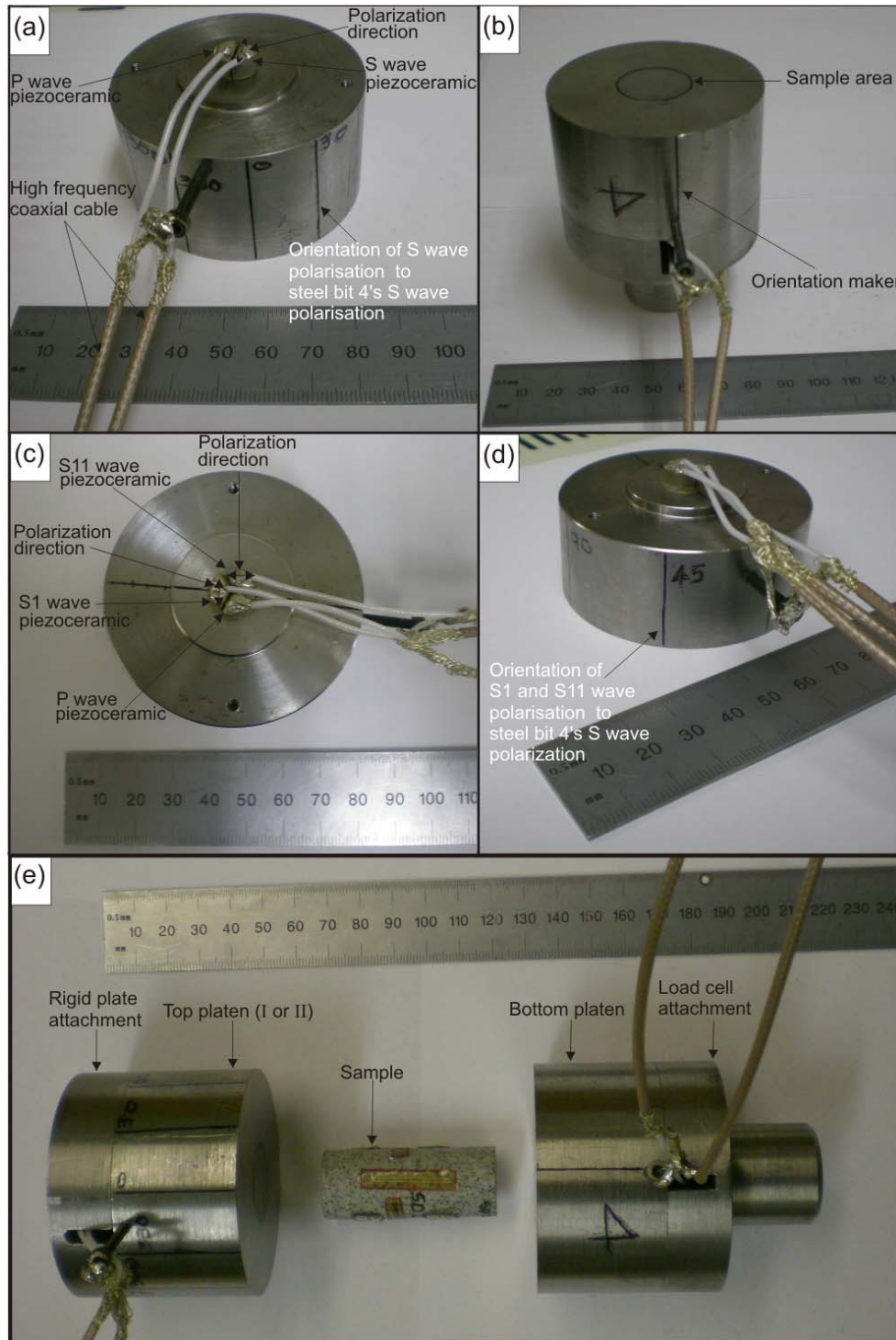


Figure 2-1. Uniaxial sample assembly. a) Top platen (I). b) Bottom platen. c and d) Top platen (II). e) Complete uniaxial sample assembly.

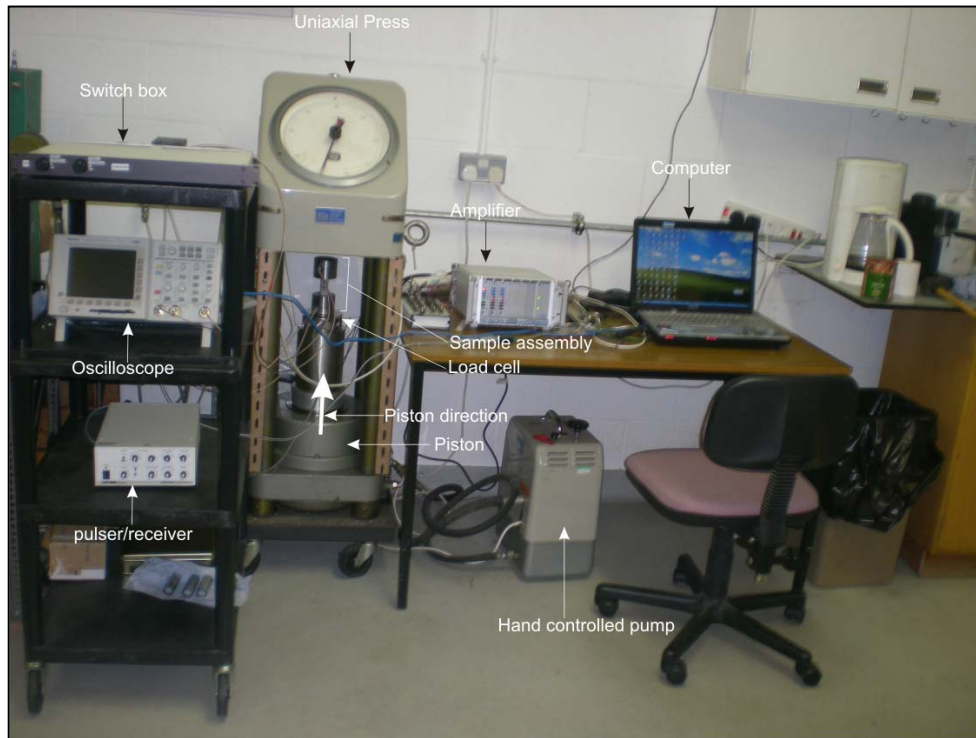


Figure 2-2. Uniaxial apparatus

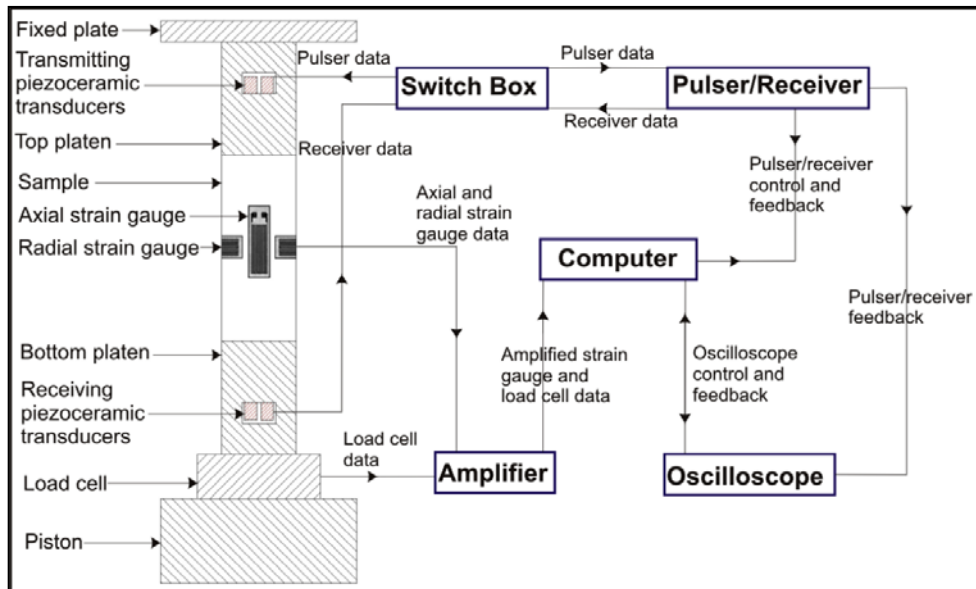


Figure 2-3. Schematic diagram of uniaxial apparatus

2.3 Hydrostatic sample assembly

The hydrostatic sample assembly (Figure 2-4 and Figure 2-5) consists of five main parts: top plug, top and bottom platen, and top and bottom platen holder. The dimensions of the top and bottom platens adhered to the standard for

using ultrasonic testing to determine pulse velocities (ASTM, 1997a) (see Section 3.6.1). The top platen holder is attached to the top plug by a central bolt and is sealed by an o-ring and a spiral backup ring. The top and bottom platens are sealed to the top platen holder and bottom platen holder respectively by an o-ring. The sample is kept separate from the confining medium by placing it in a PVC (Polyvinyl Chloride) jacket. The PVC tube seals on the o-rings of the top and bottom platens, due to confining pressure being higher than pore pressure. The upper and lower collars are attached to the top platen holder and bottom platen holder respectively. Nylon studs, fixed to the upper and lower collar, are used to prevent the bottom platen and bottom platen holder from falling due to gravity. Electrical lead-throughs are placed in the top plug and bottom platen holder to feed the high frequency coaxial cables. PEEK, a polyether ether ketone material with excellent mechanical and chemical resistance properties that are retained to temperatures up to 260°C, is used to seal and insulate the electrical lead-throughs from the body of the upper and lower bit (Figure 2-4). Two steel studs are fixed to the top plug to firmly secure the high frequency coaxial cables and for extraction of the sample assembly from the pressure vessel (Figure 2-4). Thin bore (0.5mm) high pressure pipe (Figure 2-5) is vacuum-brazed in the top and bottom platens for the introduction of pore fluid into the sample. However, pore fluid was not used in the thesis. The sample assembly is designed to accommodate 20mm diameter samples of up to 60mm in length.

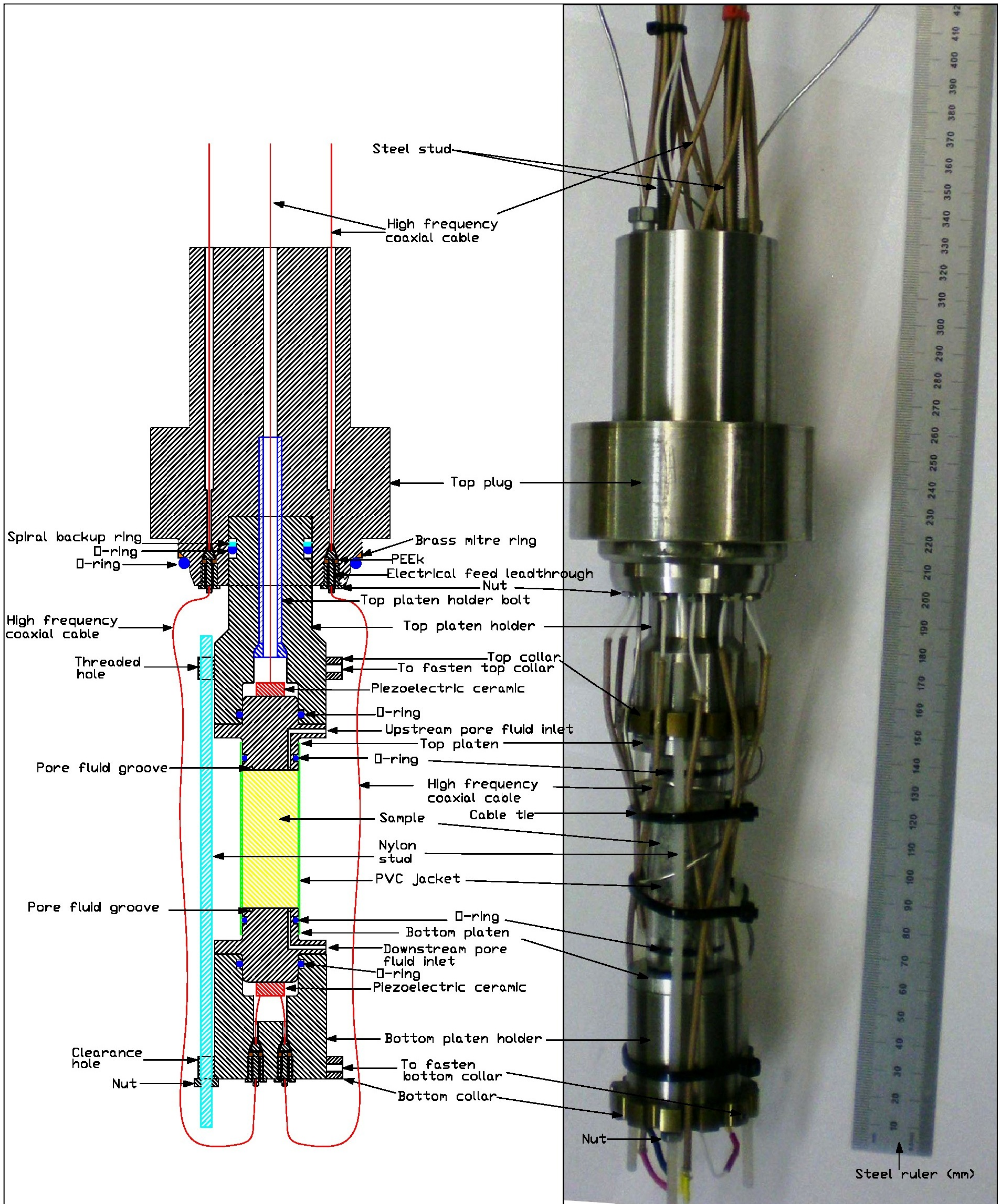


Figure 2-4. Hydrostatic sample assembly showing section through electrical feed lead-through.

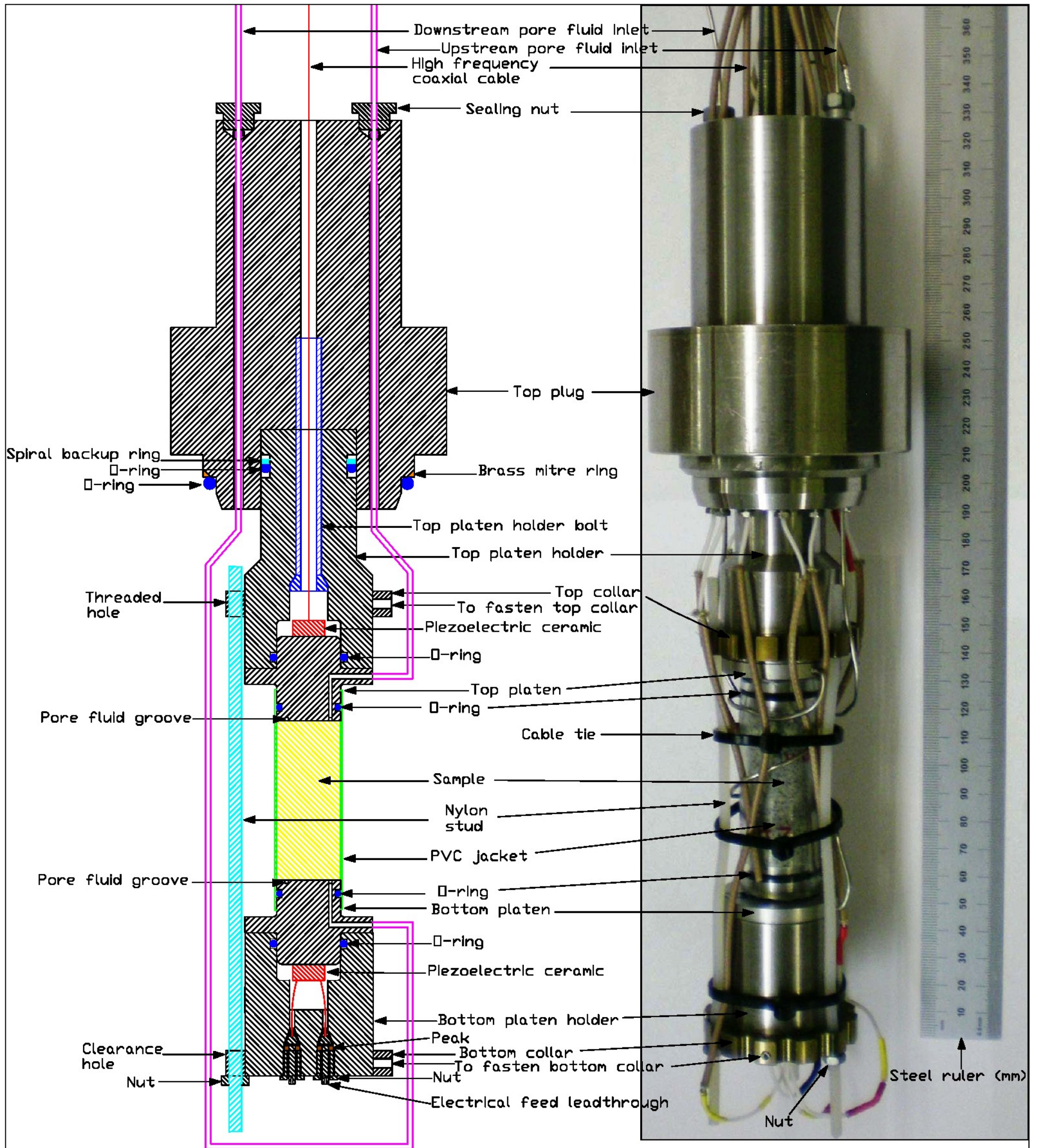








Figure 2-5. Hydrostatic sample assembly showing section through high pressure pore fluid pipe.

The top platen has a P and S wave piezoelectric ceramic with backing material and copper sheet glued to it (Figure 2-6a). The bottom platen has a P wave and two S wave piezoelectric ceramics with backing material and copper sheet glued to it (Figure 2-6c). The polarization of the two S wave piezoelectric ceramics (S1 and S11) is orthogonal to each other. This arrangement makes it easier to measure P and S wave velocity, and shear wave splitting simultaneously (see Section 3.7). The S wave piezoelectric ceramics are located away from the pore fluid pipes as they are more sensitive to the effects of the pipes than the P wave piezoelectric ceramics.

The following markings are scribed onto the outside of the bottom platen (Figure 2-6d) to show the orientation of the polarization direction of the S1 and S11 wave piezoelectric ceramics on the bottom platen to the polarization direction of the S wave piezoelectric ceramic on the top platen:

-  represents 0°. The polarization direction of the S wave piezoelectric ceramic is in the same plane as the polarization direction of the S1 wave piezoelectric ceramic.
-  represents 90°. The polarization direction of the S wave piezoelectric ceramic is in the same plane as the polarization direction of the S11 wave piezoelectric ceramic.
-  represents 45° where the amplitude and waveform of S1 and S11 waves are the same when S wave propagates through an isotropic material.
-  represents 180°. The polarization direction of the S wave piezoelectric ceramic is 180° to the polarization direction of the S1 wave piezoelectric ceramic. Here, the polarity of the S1 wave arrival reverses.
-  represents 270°. The polarization direction of the S wave piezoelectric ceramic is 180° to the polarization direction of the S11 wave piezoelectric ceramic. Here, the polarity of the S11 wave reverses.
-  represents 225° where the amplitude and waveform of S1 and S11 waves are the same when S wave propagates through an isotropic material. Here, the polarity of the S1 and S11 wave reverses.

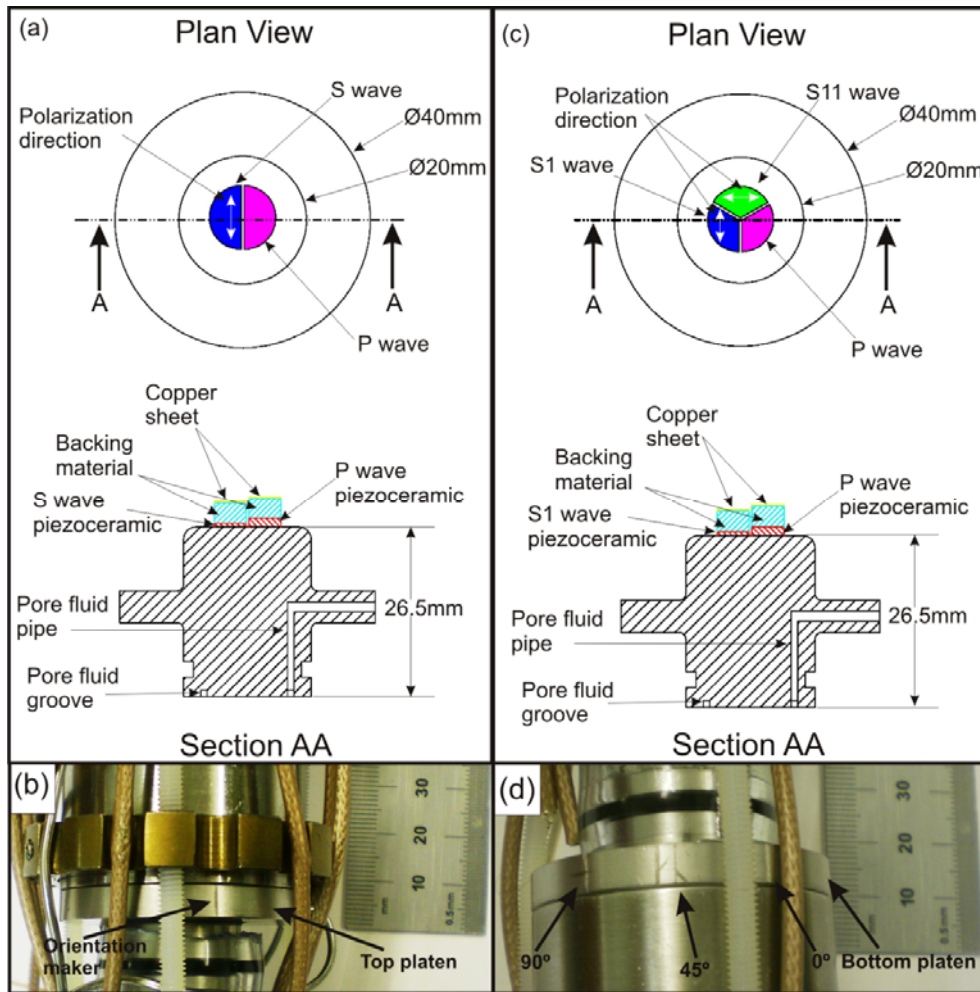


Figure 2-6. Piezoelectric ceramic arrangements on top (a) and bottom (c) platens. b) orientation marker on top platen, d) Orientation of the polarization of S1 and S11 wave piezoelectric ceramics to the polarization of S wave piezoelectric piezoelectric ceramic.

The hydrostatic sample assembly is placed within the vessel of a hydrostatic flow rig with servo-controlled pore fluid flow system (Figure 2-7, Figure 2-8, Figure 2-10) that was designed and constructed by Faulkner, D. and Armitage, P. (*Armitage, 2008*). The hydrostatic rig is capable of performing experiments at confining pressures up to 200MPa (approximately equivalent to 8km depth in the Earth's crust). The sample assembly is secured by the threaded top nut and is sealed by an o-ring and brass mitre ring configuration. Confining

pressure is generated in the pressure vessel by the use of an air-driven SC hydraulic pump (Figure 2-8c) using low viscosity 10 cs silicon oil. A combination of pumps generates and controls pore fluid pressure in the system. Pore fluid pressure in the system can be generated by the NovaSwiss hand pump (Figure 2-8a), a Haskel AGT-62/152H gas booster (Figure 2-9), or a combination of both. An ultrasonic system, discussed in section 3.5, is attached to the sample assembly.

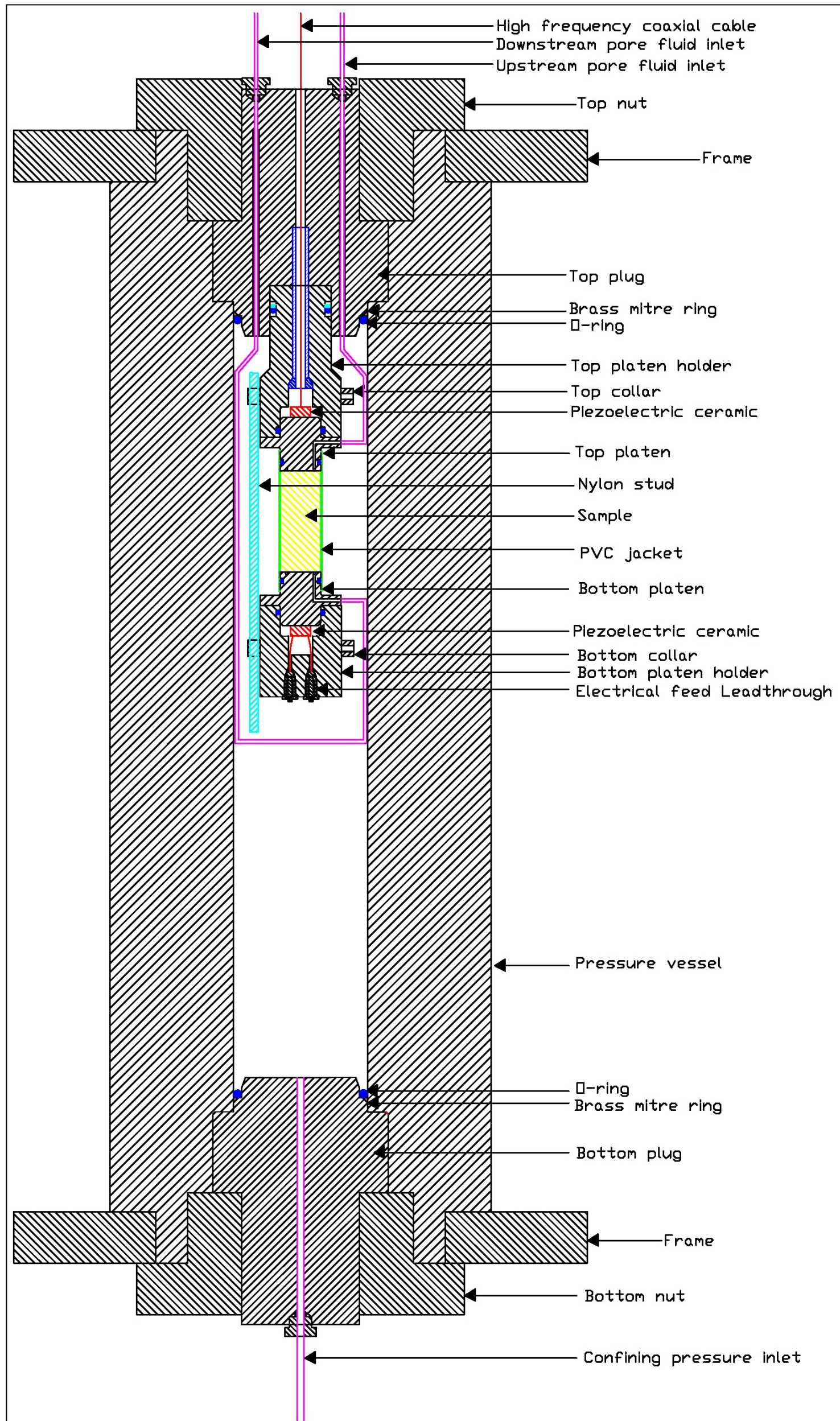


Figure 2-7. A typical section through the sample assembly inside the vessel of the hydrostatic apparatus. 1:2 scale. [after Armitage, 2008]

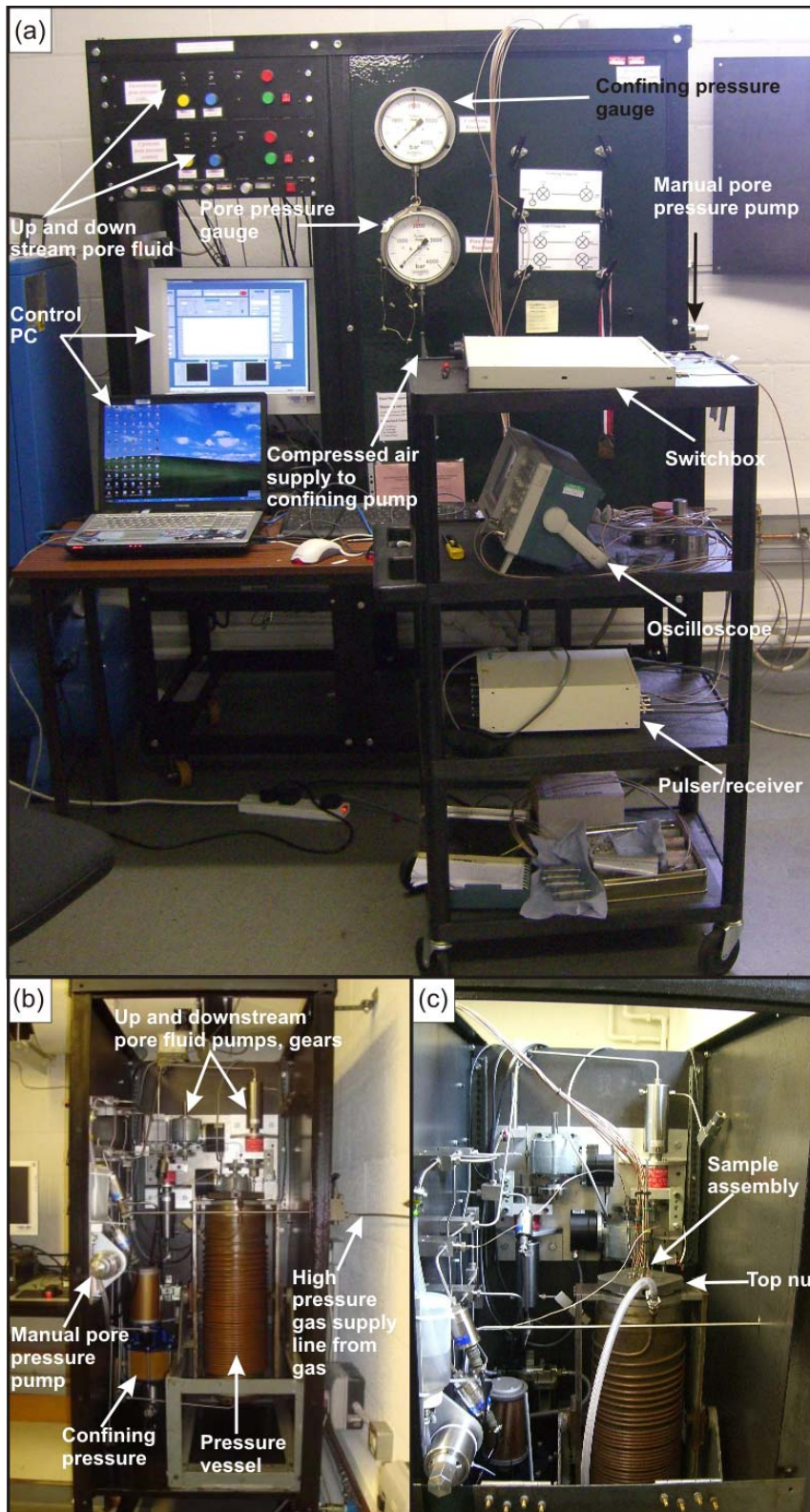


Figure 2-8. Hydrostatic apparatus. a) Ultrasonic system attached. b) Side view of hydrostatic apparatus with shielding removed. c) Sample assembly in vessel.

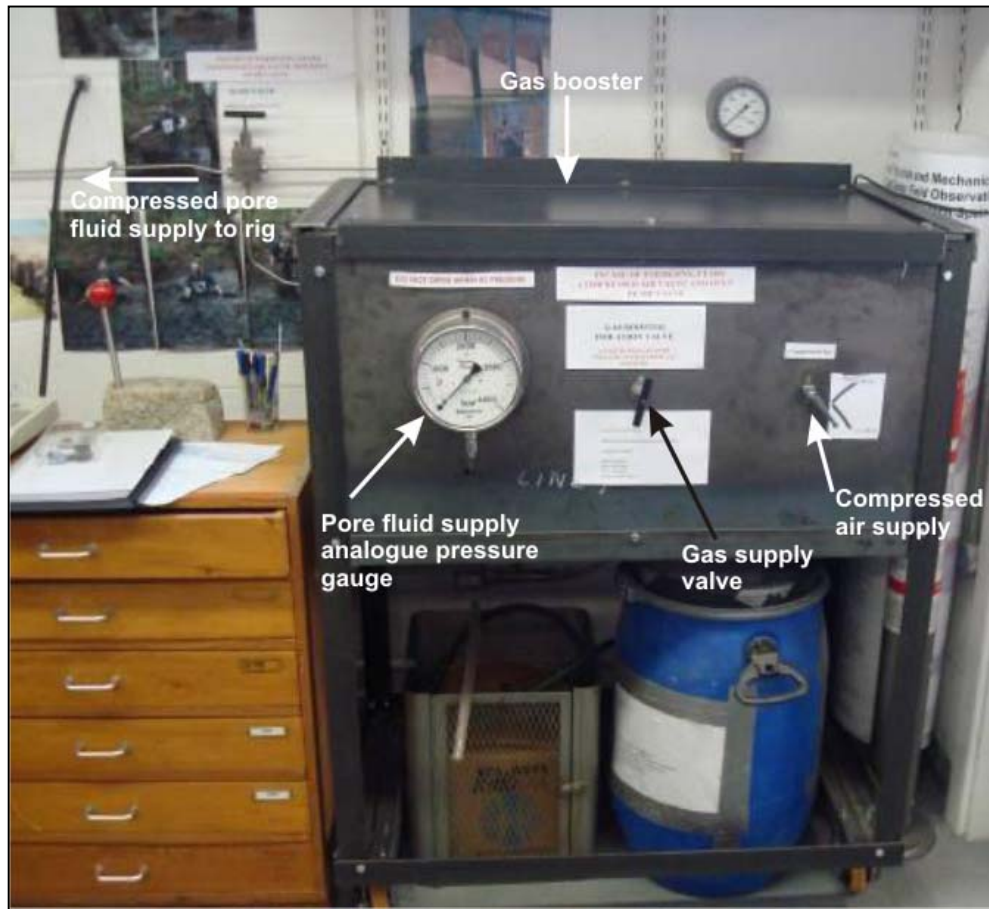


Figure 2-9. Gas booster used to supply compressed gas pore fluid to the hydrostatic flow rig

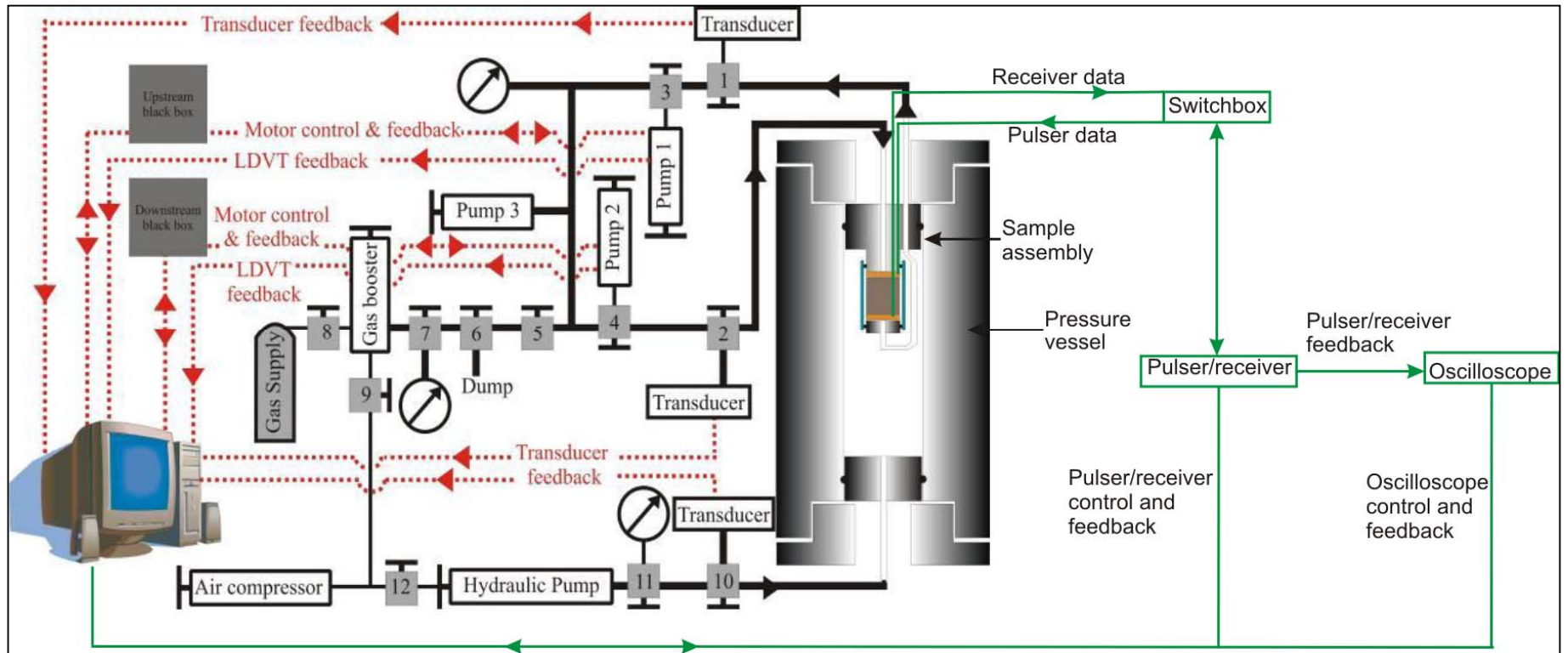


Figure 2-10. Schematic diagram of the hydrostatic apparatus. The dotted lines show electrical connections for control and feedback from motors and transducers. Thick solid lines show high pressure pipe system, thin solid lines show low pressure pipe system. Green coloured lines show the ultrasonic system (after Armitage, 2008).

2.4 Preparation of samples for testing

The samples were cored from samples of rock to a nominal diameter of ~20 mm using a diamond tipped coring drill (Figure 2-11a). The ends of the cores were cut to achieve a length-to-diameter ratio in excess of 2.5 but less than 3 (Paterson and Wong, 2005) using a diamond blade saw (Figure 2-11c). A grinding machine (Figure 2-13a) that has a 400 grit grinding wheel is used to precision-grind the cored samples to strict tolerances (± 0.02 mm) as to the squareness of their ends and to polish the ends to a surface finish of approximately 0.1Ra. Using such a high tolerance will prevent build up of undesired stress concentrations within the sample upon loading. The coring machine, diamond blade saw, and grinding machine use water as coolant. An oven is used to dry the cores (at 80°C). Axial and radial strain gauges are glued to cores for use in the uniaxial apparatus (Figure 2-12c).



Figure 2-11. Coring and cutting the ends of a rock sample. a) Coring drill. b) Cores from a Westerly granite sample. c) Diamond blade saw

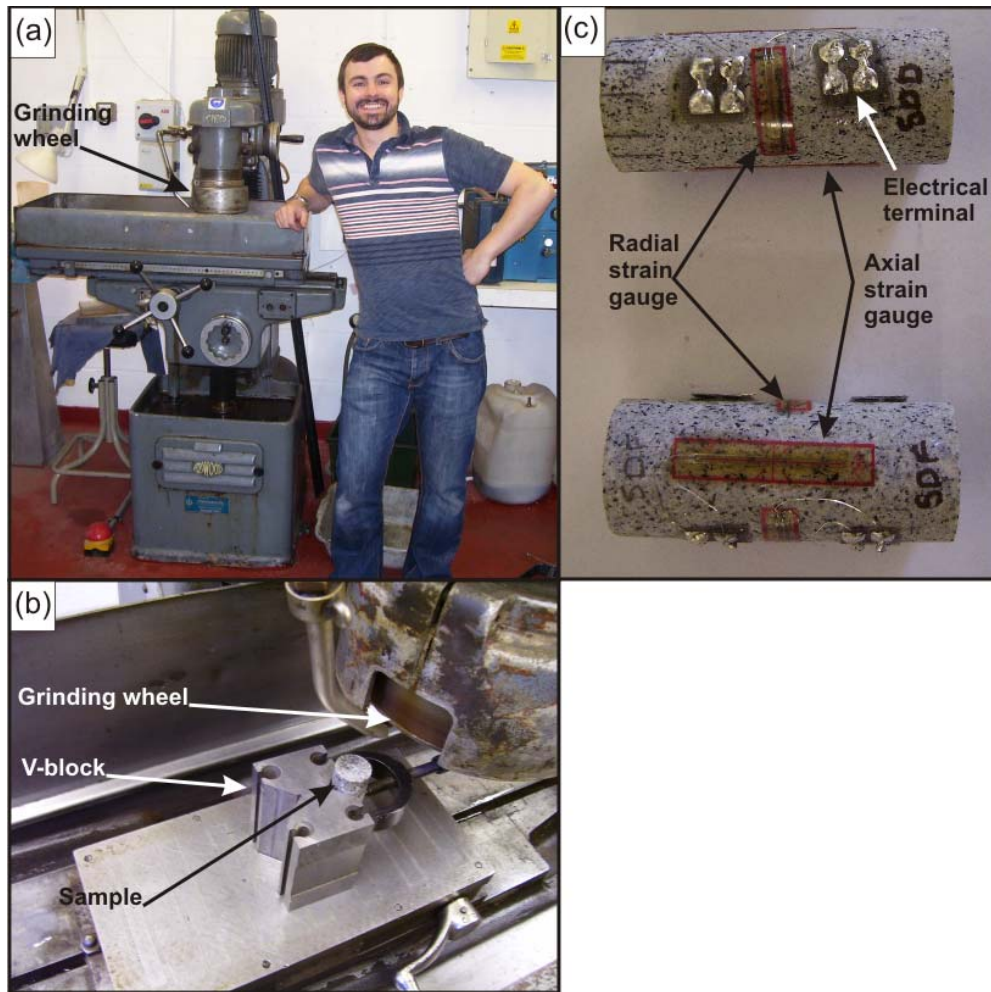


Figure 2-12. Squaring and surface finishing of cores. a) Grinding machine. b) Cored sample fixed in V-block. c) Radial and axial strain gauge glued to core.

2.5 Ultrasonic measurement System

An ultrasonic measurement system involves the generation, propagation, and reception of short transient signals. The system consists of piezoelectric ceramics, a pulser/receiver, a switchbox, high frequency coaxial cables, and an oscilloscope. The components of the ultrasonic measurements system are discussed in this section.

2.5.1 Generation and detection of P and S waves

In laboratory experiments, P and S wave are generated and received by piezoelectric ceramics. Piezoelectric ceramics convert the electrical energy to mechanical energy and vice versa, as it changes its shape when an electrical field is applied to it. The piezoelectric effect can be found in nature in quartz and tourmaline crystals. In industrial applications, it is often obtained artificially with certain ceramics such as barium titanate, (BaTiO_3) lead zirconate titanate, referred to as PZT $(\text{Pb}(\text{Zr}, \text{Ti})\text{O}_3)$, and lead meta-niobate $(\text{PbNb}_2\text{O}_6)$. The piezoelectric ceramic used in the ultrasonic measurement system is made of PZT-5H that has a fundamental frequency of 1.5MHz and is overtone polished, which facilitates measurements up to the 7th harmonic (from Boston Piezo-Optics, Inc., USA.). PZT-5H has a high electromechanical conversion efficiency, low intrinsic losses, can operate at temperatures up to 170°C, and it is stable over long periods of time (Hooker, 1998).

Based upon the polarization, piezoelectric ceramics can generate or receive P or S waves. P waves are generated when the piezoelectric ceramic is polarized in the direction of wave propagation and electrodes are applied on the two faces of the ceramic normal to the polarization direction as shown in Figure 2-13(a) and Figure 2-14. For the generation of S waves, the piezoelectric ceramics are polarized normal to the direction of wave propagation and electrodes are applied to the two faces that are parallel to the polarization direction as shown in Figure 2-13(b) and Figure 2-14.

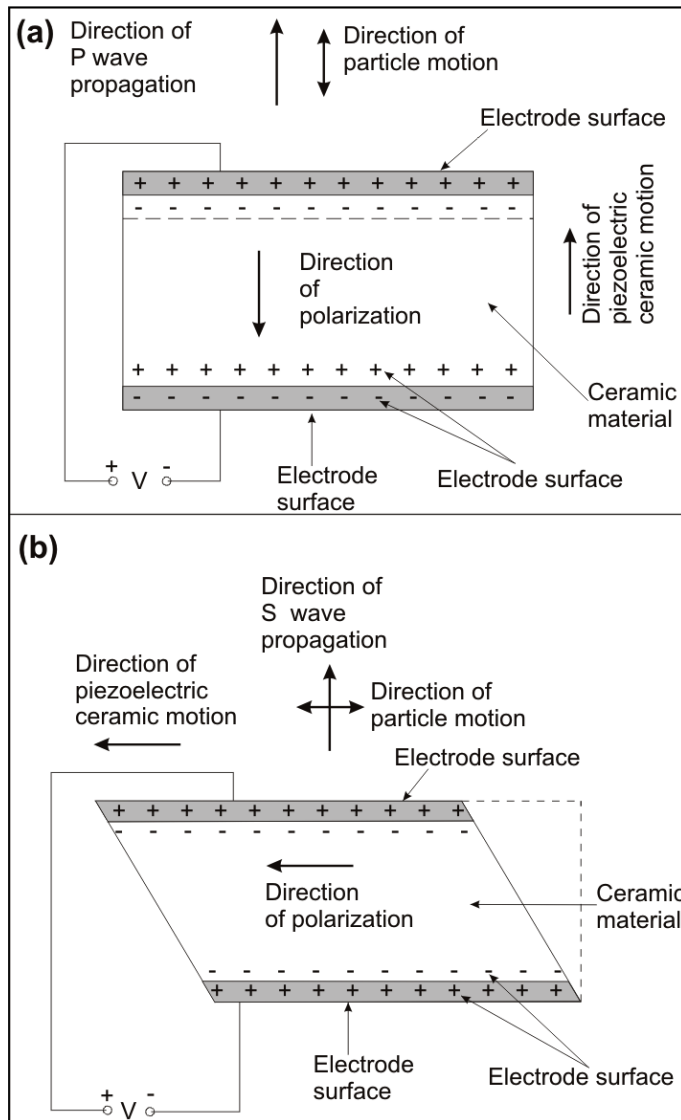


Figure 2-13 Schematic of piezoelectric ceramic for compression(a) and shear waves (b) (after Strassburger, 1982)

A backing material is fixed to the piezoelectric ceramic. The backing is usually a highly attenuative, high density material that is used to control the vibration of the piezoelectric ceramic by absorbing the energy radiating from the back face of the piezoelectric ceramic. If a coaxial cable (section 3.5.4) is directly soldered onto the face of the piezoelectric ceramic, a slight pull or push of the cable will damage the piezoelectric ceramic. Consequently, the backing

material also protects the piezoelectric ceramic from damage due to this effect. When the elastic wave impedance of the backing matches the elastic wave impedance of the piezoelectric ceramic, the result will be a heavily damped piezoelectric ceramic with wider bandwidth that displays good range resolution (an excellent characteristic for attenuation measurement), but may be lower in signal amplitude. The elastic wave impedance (Z) of a material is defined as the product of its density (ρ) and elastic wave velocity (V):

$$Z = \rho V \qquad \text{Equation 2-1}$$

As the elastic wave impedance of the piezoelectric ceramic becomes greater than the elastic wave impedance backing material, the amplitude of the signal increases but the piezoelectric ceramic resolution is reduced (Figure 2-15). In this work we used sintered stainless steel, 0.125"±0.005" thick with 0.5 micron nominal pore size (from Mott Corporation, USA), as a backing material on the piezoelectric ceramics [VanValkenburg, 1983]. The elastic wave impedance of both the backing material and PZT-5H is ~29.7 MRayls. It is difficult to soft solder a material to stainless steel because of its thin and strong oxide films. Therefore, a thin sheet of copper, ~0.25mm thick, which is much easier to soft solder onto, is glued to the stainless steel using silver-loaded epoxy adhesive (Figure 2-14).

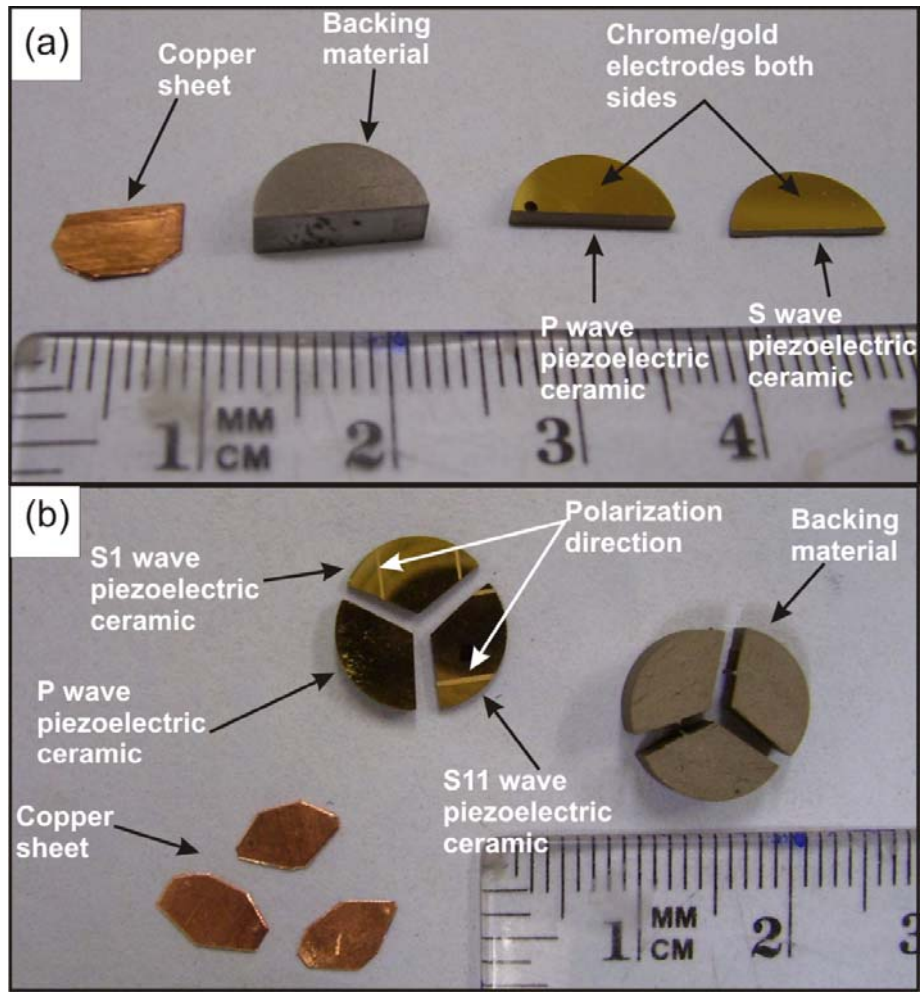
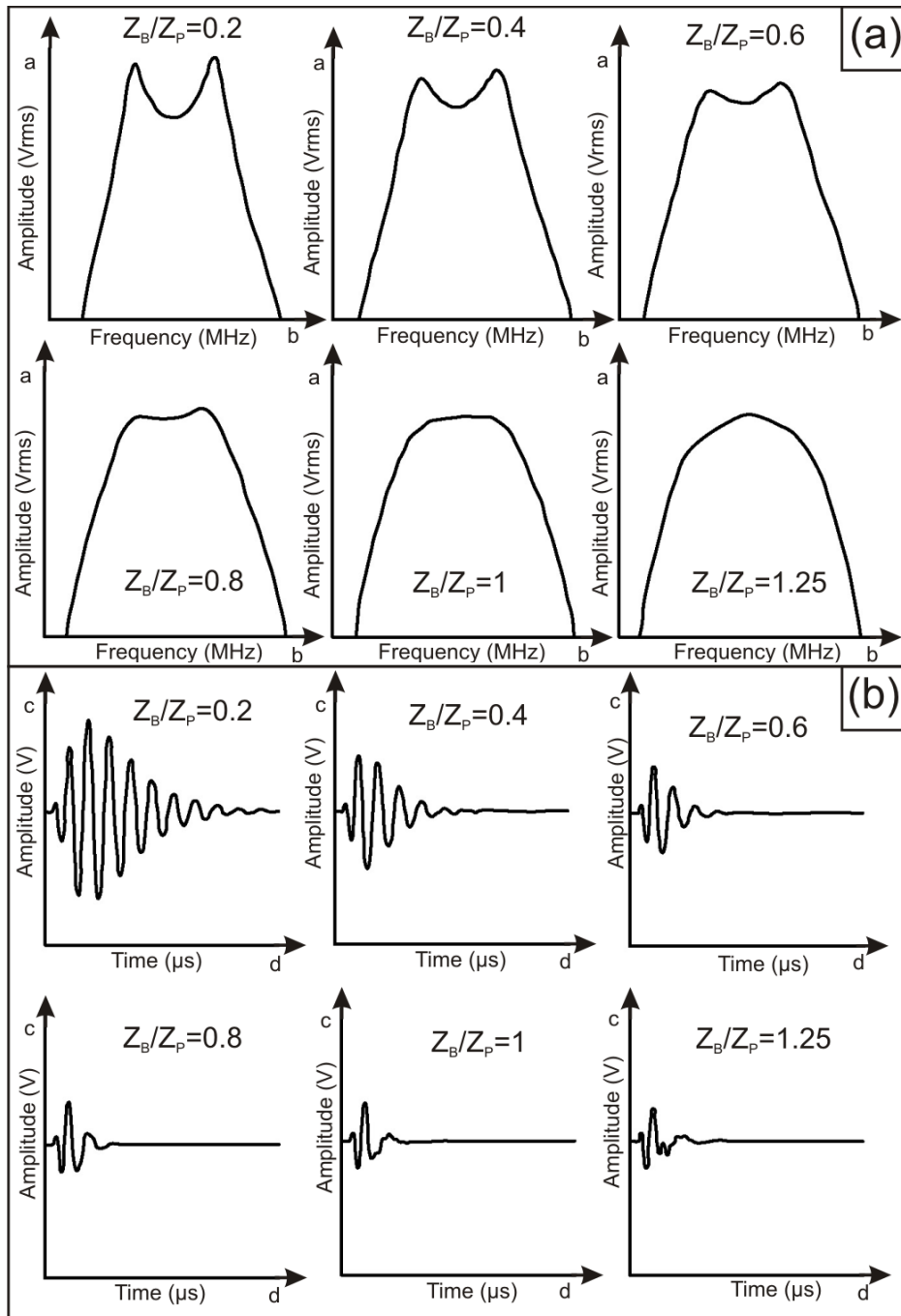


Figure 2-14. Piezoelectric ceramic, backing and copper sheet arrangement.

a) Cut into halves b) Cut into thirds



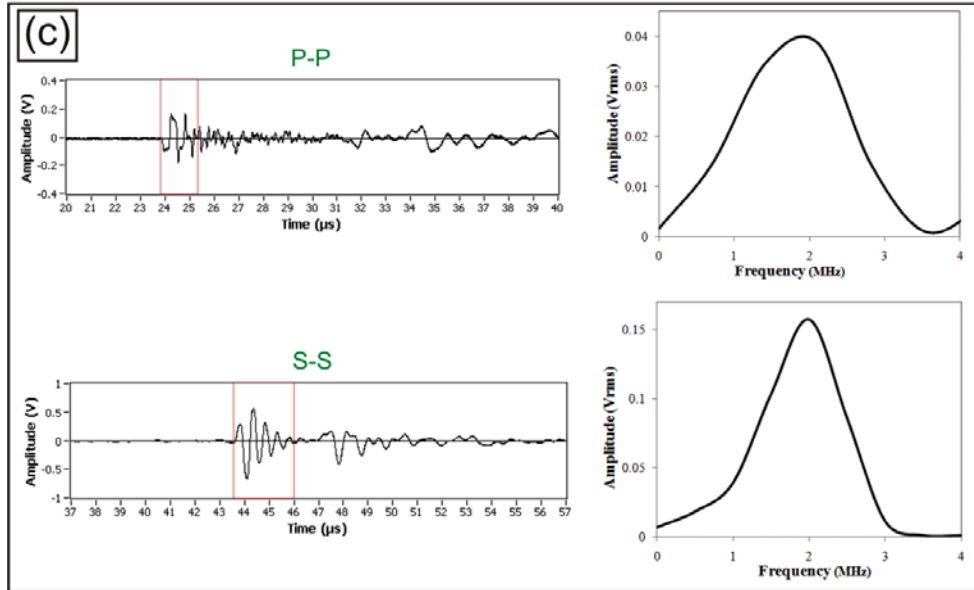


Figure 2-15. The effect of backing material on piezoelectric ceramics signals. Computer simulated piezoelectric ceramic signals with backing material of different elastic wave impedance: a) frequency response of the piezoelectric ceramic; b) transient response of the piezoelectric ceramic. $Z_P = 28 \text{ MRayl}$. Z_P is the elastic wave impedance of the piezoelectric ceramic, Z_B is the elastic wave impedance of the backing material (after Safari and Akdoğan, 2008). c) Measured signal through mild steel sample using the through-transmission method. P-P refers to pulsing with the P wave piezoelectric ceramic and receiving with another P piezoelectric ceramic and S-S refers to pulsing with S wave piezoelectric ceramic and receiving with another S wave piezoelectric ceramic. The red rectangles highlights the wave train of the P and S wave arrivals. Fast Fourier transform of the wave trains are shown to the right. The elastic wave impedance of both the backing material and piezoelectric ceramic is $\sim 29.7 \text{ MRayls}$.

2.5.2 Pulser/receiver

A pulser/receiver generates the energy that drives the transmitting piezoelectric ceramic in the ultrasonic measurement system and amplifies and/or filters the electrical response arriving from the receiving transmitting piezoelectric ceramic. A negative spike pulser / receiver (JSR DPR300 Pulser / Receiver) operated in the through-transmission mode was used (Figure 2-16). In the through-transmission mode, a piezoelectric ceramic is used to generate the elastic wave and another piezoelectric ceramic is used to receive the elastic wave that propagated through the rock sample. The pulser/receiver can also be used in pulse-echo mode. In the pulse-echo mode, a single piezoelectric ceramic is used for elastic wave generation and detection of reflected elastic waves from interfaces or cracks within the rock sample. The through-transmission mode is more suitable for measuring P and S wave velocities and attenuation of geomaterials (Krautkramer and Krautkramer, 1990). The pulser/receiver can be manually and or computer control using the JSR Instrument Control Panel program.

The pulser side of this instrument has three controls: energy, repetition rate, and damping. The energy control is composed of pulse energy, pulser impedance and pulse amplitude controls. Pulse energy and pulser impedance control set the energy of the excitation pulse generated by the pulser, and the pulser impedance respectively. The high pulser impedance range provides for better piezoelectric ceramic damping while the low pulser impedance range provides for better signal strength. The pulse amplitude control sets the amplitude of the excitation pulse and is adjustable between 100V and 900V. The energy is stored in the capacitor, C_o (Figure 2-16). This energy is periodically discharged into the sending piezoelectric ceramic by closing the repetition switch. The repetition rate controls the frequency at which this switch is closed, which varies between 100 Hz to 5 kHz. Generally, this rate is set to ensure that the waves travelling in a test sample have had time to decay in amplitude to very small values before the next discharge occurs. Stacking the repetition of the elastic wave improves the signal-to-noise ratio (Figure 2-17). The damping control adjusts the damping, R_d , applied to the piezoelectric ceramic.

The receiver side of the pulser/receiver has a low-noise amplifier which amplifies the received electrical signal between -13 dB and 66 dB. The signals then pass through adjustable high pass (from 0 to 12.5MHz) and low pass (from 3MHz to 35MHz) filters.

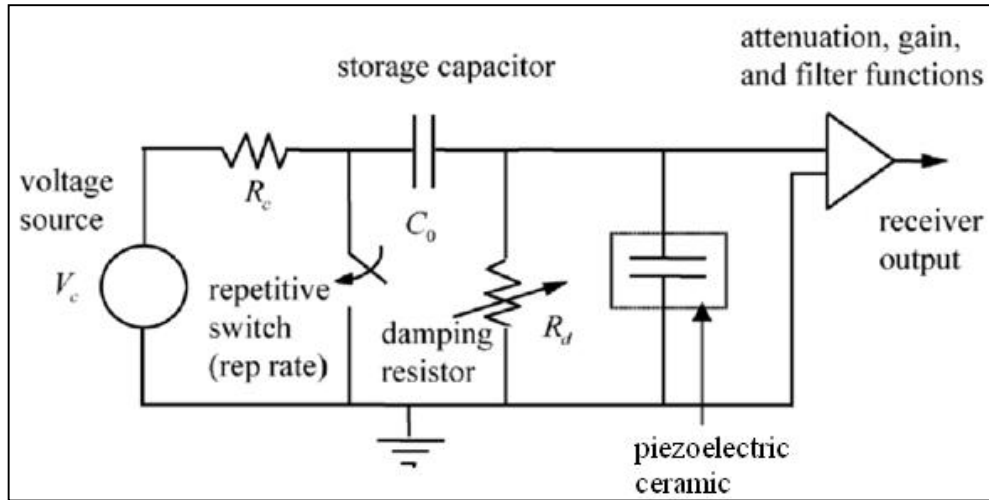


Figure 2-16. A highly simplified circuit representation of a “spike” pulser/receiver (after Schmerr Jr and Song, 2007).

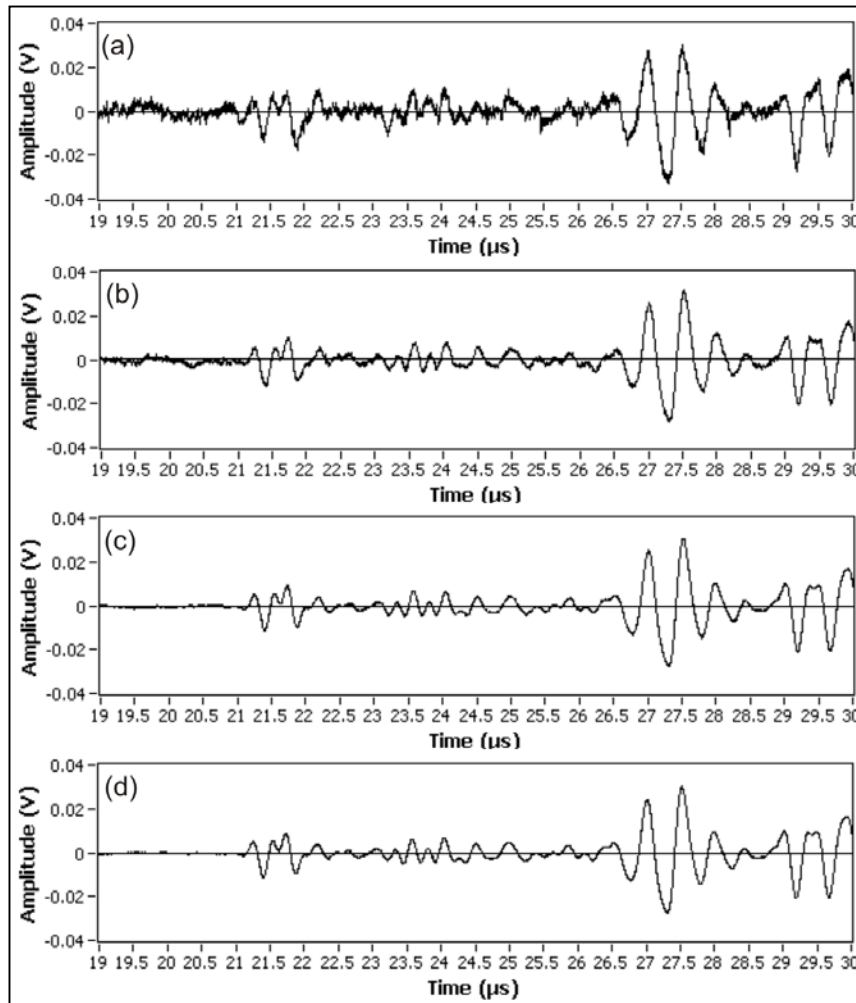


Figure 2-17. Signal-to-noise ratio improvement by summing or ‘stacking’ ultrasonic waves using a Tektronix TDS 3032B oscilloscope. a) A single signal. b) Stacking 4 signals. c) Stacking 32 signals. d) Stacking 512 signals. The P wave arrival is clearly seen in (d) after 21 μ s.

2.5.3 Switchbox

The switchbox composes of two rotary multi-way switches and provides the option of choosing which piezoelectric ceramic to excite or receive signal from. One switch controls the pulsing data and the other controls the receiving data. Each switch has four positions:

- Off.
- A – for P wave piezoelectric ceramics.
- B – for S or S1 wave piezoelectric ceramic.
- C – not used or for S11 wave piezoelectric ceramic.

2.5.4 Cabling

At the MHz frequencies involved in ultrasonic measurements, the electrical cables that transfer the electrical pulses from the pulser to the sending piezoelectric ceramic and from the receiving piezoelectric ceramic to the receiver do not just pass those signals unchanged. Thus, significant cabling effects may be present in the ultrasonic measurement setup. To minimize this effect, a high frequency coaxial cable (Attenuation @ 100MHz: 3.61dB, Capacitance per meter: 105pF) is used. The resistance of the high frequency coaxial cable is 50 Ohm because the resistance of the coaxial cable should be the same as the output of the pulser/receiver to reduce internal reflections at connections between components.

2.5.5 Data presentation

The ultrasonic data is collected and displayed in the A-scan format. The A-scan format displays the amount of received ultrasonic energy, measured as a voltage, as a function of time. The relative amount of received energy is plotted along the vertical axis and the elapsed time is displayed along the horizontal axis. A 300MHz bandwidth digital oscilloscope with 20ppm time based accuracy (Tektronix TDS 3032B) is employed for recording and display of the received pulse which is synchronized with the pulser/receiver. The oscilloscope can also sum or 'stack' up to 512 signals to improve the signal-to-noise ratio. The recorded signal is downloaded from the oscilloscope in a '.isf' format and then converted to '.csv' format using a 'isf to csv' conversion script (see appendix 8.2). A program written in labview (version 8.5) is used to display and analyze the recorded signal (see appendix 8.1). The oscilloscope can be manually or computer controlled using the Tektronix Escope web-based remote control program.

2.6 Understanding ultrasonic P and S wave signals

The arrival time of the P wave is easily identified since it is the fastest propagating wave and therefore the first wave to reach the receiver. In contrast to P wave, S wave measurements require more care in signal analysis because the waveform at the receiver is not composed of only S wave arrival; it is composed of P wave, S to P and P to S conversions waves, as well as the S wave. Many authors have commented on the difficulties in identifying the exact time of arrival of the S wave (Brignoli et al., 1996; Dyvik and Madshus, 1985; Nakagawa et al., 1996; Viggiani and Atkinson, 1995a; Viggiani and Atkinson, 1995b). It is commonly taken that the first deflection of the received signal indicates the arrival of the wave. However, *Dyvik and Madshus* (1985) and *Brignoli et al.* (1996) suggested that the arrival of the S wave is represented by the first maximum of the received signal (Figure 2-18) and that the potential error between these two interpretations is an overestimation of shear modulus of up to 14%.

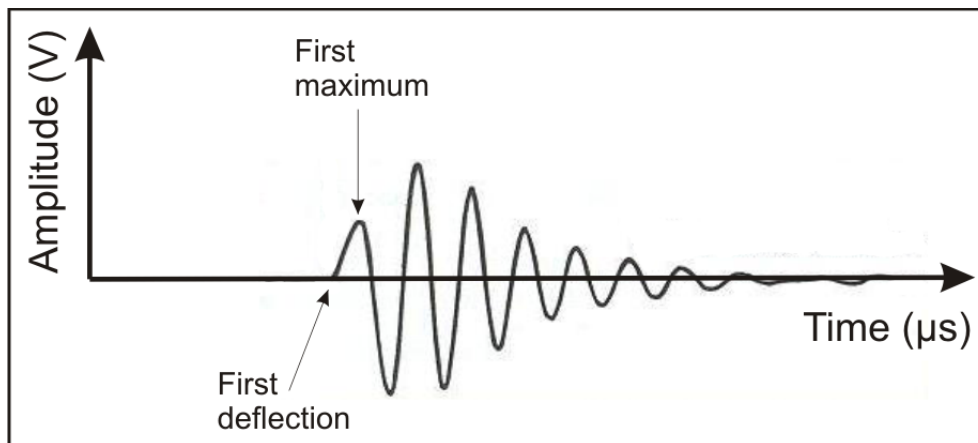


Figure 2-18. P or S wave arrival. The polarity of the first maximum is dependent on the pulser wave input. The polarity of the first maximum of S wave arrival is also dependent on the angle between the polarization direction of the pulsing S wave piezoelectric ceramic and the polarization direction of the receiving S wave piezoelectric ceramic.

2.6.1 P and S wave signals

For reliable and accurate measurement of P and S wave velocity, the standard for using ultrasonic testing to determine pulse velocities (ASTM, 1997a), recommends the following limitations on dimensions:

- The ratio of the pulse-travel distance to the minimum lateral dimension should not exceed 5.
- The travel distance of the pulse through the rock sample should be at least 10 times greater than the average grain size so that an accurate average propagation velocity may be determined.
- The minimum lateral dimension should be at least five times greater than the wavelength. The restriction on the minimum lateral dimension as a function of wavelength is due to the dispersion phenomenon. Dispersion occurs due to interaction of the wave with the boundary of the system, resulting in wave mode conversion. Dispersion will not occur if the minimum lateral dimension is at least five times the wavelength (Wasley, 1973)
- The wavelength should be at least 3 times greater than the average grain size.

The above criteria can be combined to give the relationship:

$$D \geq 5(V/f) \geq 15d \quad \text{Equation 2-2}$$

where D is the minimum lateral dimension of the rock sample (m), d is the average grain size (m), V is the velocity of the rock sample (m/s) and f is the frequency (Hz) of the piezoelectric ceramic.

Since V and d are inherent properties of the rock sample, f and D should be selected to satisfy equation 2-2. For example, using a piezoelectric ceramic of frequency 1.5MHz will satisfy equation 2-2 when Westerly granite from south-east Rhode Island, USA, that has small grain size (average 0.75mm), cored to 20mm diameter with length-to-diameter ratios in excess of 2.5 but less than 3, and has average P and S wave velocity of ~6000 m/s and 3000 m/s respectively, is used as the rock sample.

To understand the characteristics of ultrasonic P and S wave arrivals, a sample with known properties should be placed in the ultrasonic measurement system. P and S wave piezoelectric ceramics were glued to the ends of a mild steel sample (Figure 2-19) using silver-loaded epoxy adhesive. Silver-loaded epoxy was also used to fix the backing material and copper sheet to the piezoelectric ceramic. The steel sample has an effective dimension of 30mm diameter and 140.69mm length (Figure 2-20). The 140.69mm length provides a large separation time between the P and S wave arrival. Proper care was taken to ensure that the pulsing P and S wave piezoelectric ceramic were aligned accurately with the receiving P and S wave piezoelectric ceramic respectively, and the polarization direction of the pulsing S wave piezoelectric ceramic is in the same plane as the polarization direction of the receiving S wave piezoelectric ceramic. Four different waveforms were recorded (Figure 2-21): Pulsing with the P wave piezoelectric ceramic and receiving with P piezoelectric ceramic (P-P), pulsing with P piezoelectric ceramic and receiving with S wave piezoelectric ceramic (P-S), pulsing with S wave piezoelectric ceramic and receiving with P wave piezoelectric ceramic (S-P), and pulsing with S wave piezoelectric ceramic and receiving with S wave piezoelectric ceramic (S-S). The pulser/receiver settings that gave an excellent excitation and reception of the piezoelectric ceramics are shown in Figure 2-22. The P wave arrival, at the first deflection, can be seen clearly at 23.852 μ s in all traces but the amplitude is significantly reduced in the P-S, S-P, and S-S traces. The arrival of the S wave can also be seen in all the traces but the first deflection can only be picked reliably and accurately in the S-S trace at 43.560 μ s. The P wave and P to S and S to P conversion wave arrivals are within the noise level in the S-S trace. P to S and S to P conversion waves occurs when an incoming P or S wave strikes an interface at an angle other than 90 degrees. In contrast, the P and S wave arrivals (Figure 2-24), from another setup (Figure 2-23) that did not adhere to the standard for using ultrasonic testing to determine pulse velocities (ASTM, 1997a) showed different characteristics. The ratio of the pulse travel distance to the minimum lateral dimension of the setup is 9.2, which exceeded the recommended ratio of 5. The minimum lateral dimension is 1.5 times greater than the P wave wavelength and 3 times greater than the S wave wavelength, which is less than the recommended

lateral dimension. The setup also did not use any backing material fixed to the piezoelectric ceramic and used 75 ohm high frequency cable, which is different to the resistance of the pulser/receiver (50 ohm). The P wave arrival, at the first deflection, is also easily identified but the S wave arrival cannot be reliably and accurately located. There is undesired effect within the system because of the impedance mismatch between high frequency cabling and the pulser/receiver which is seen at the excitation pulse of the P-P and S-S traces. A ringing effect is also visible in the P wave (long pulse duration, from first deflection arrival to approximately 19 μ s) and S wave (long pulse duration, from uncertain arrival region to approximately 31 μ s) arrivals.

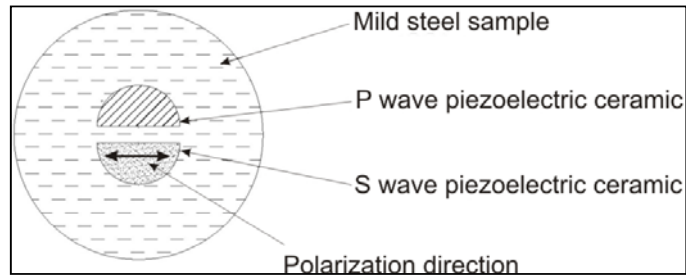


Figure 2-19. P and S wave arrangement on both ends of the mild steel sample.

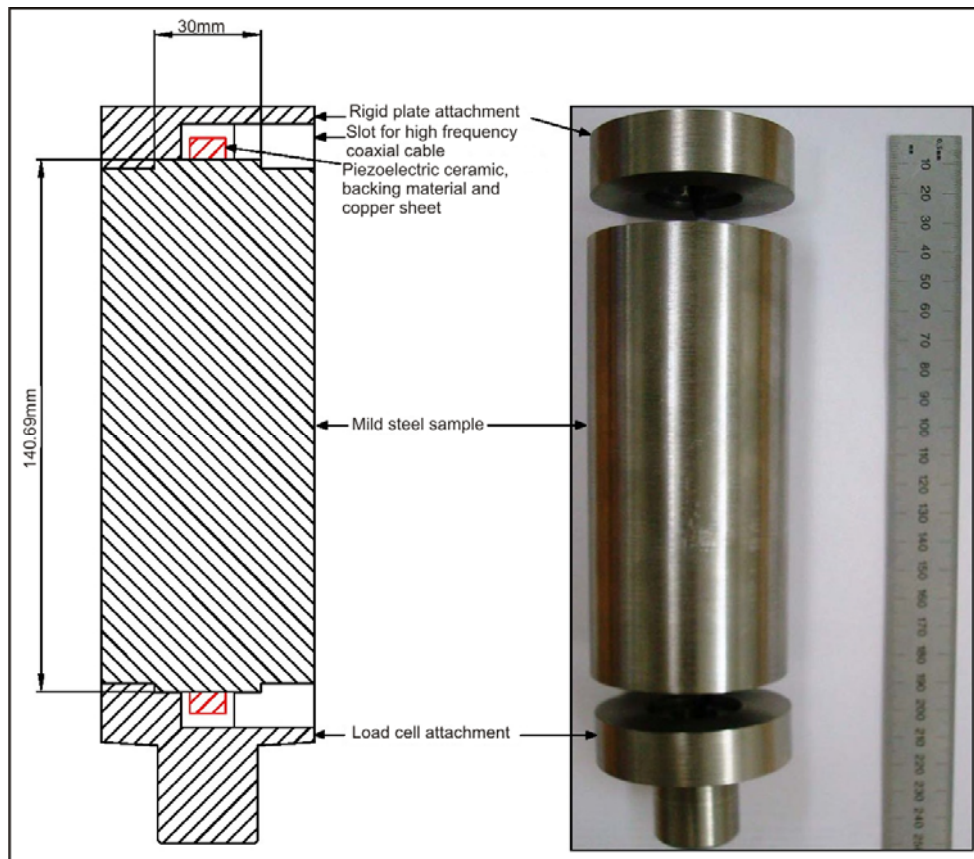


Figure 2-20. Mild steel sample placed in the ultrasonic measurement system. The dimensions of the sample adhered to the standard for using ultrasonic testing to determine pulse velocities (ASTM, 1997a). The sample was designed to fit in a standard uniaxial compressional apparatus.

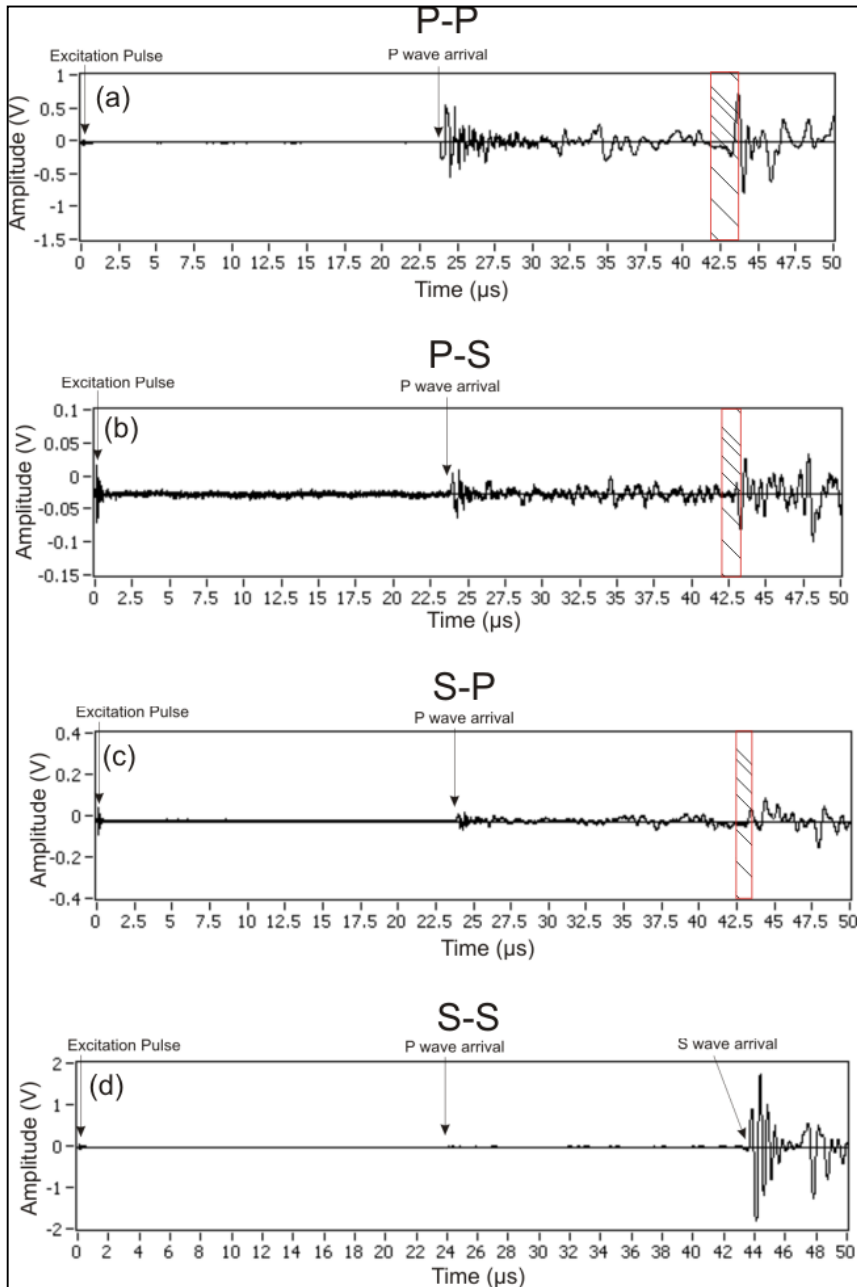


Figure 2-21. Recorded waveforms from measurements made on a mild steel sample that adhered to the ASTM standards (ASTM, 1997a). The arrows indicate the first deflection of the P or S wave arrival. The hatched area represents the region of uncertainty in picking the S wave arrival. a) P-P trace. b) P-S trace. c) S-P trace. d) S-S trace

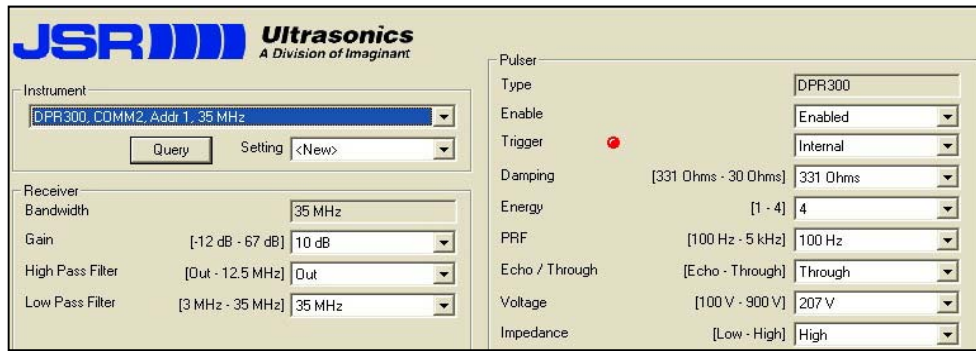


Figure 2-22. Typical pulser/receiver settings that give an excellent excitation and reception of the piezoelectric ceramics.

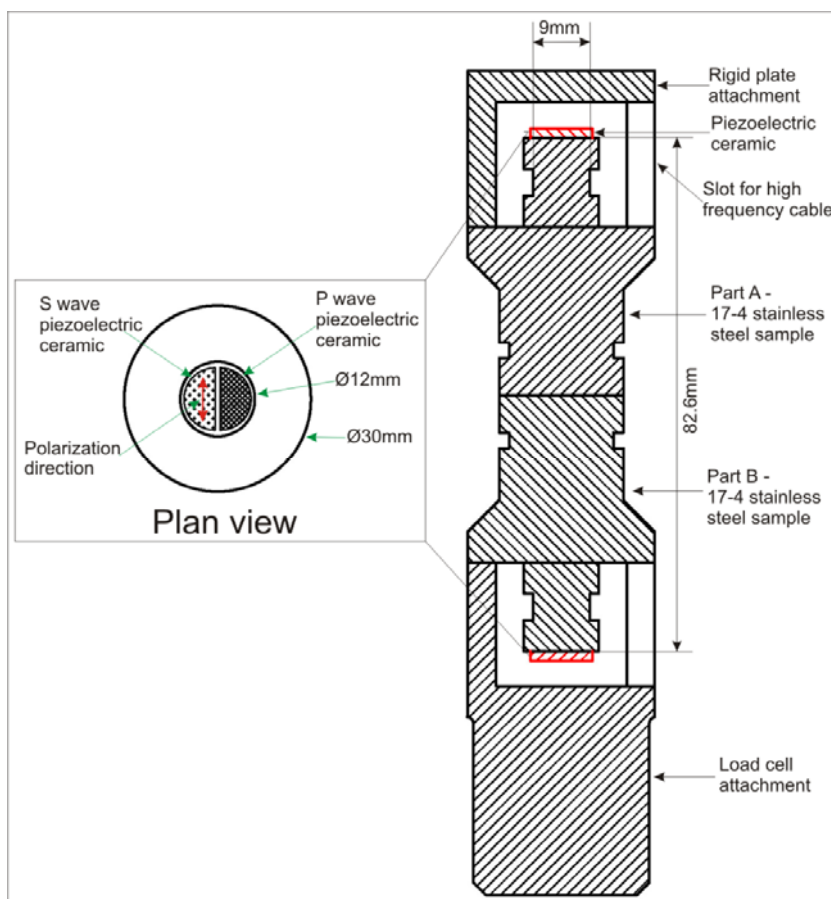


Figure 2-23. 17-4 PH (chromium-copper precipitation hardening) stainless steel sample (part A and part B) placed in the ultrasonic measurement system. The dimensions of the sample do not adhere to the standard for using ultrasonic testing to determine pulse velocities (ASTM, 1997a). The sample was designed to fit in a standard uniaxial compressional apparatus. The fundamental frequency of the piezoelectric ceramics are 1MHz.

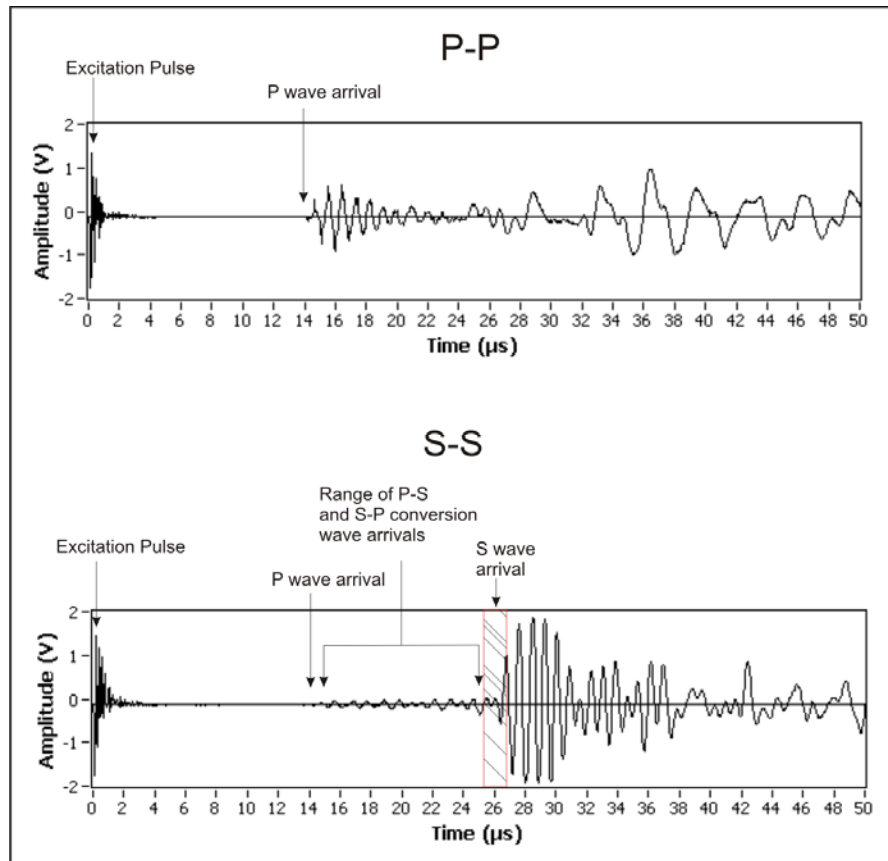


Figure 2-24. Recorded waveforms from measurements made on a 17-4 PH stainless steel sample that falls outside of the ASTM standards (ASTM, 1997a) and without backing material on the piezoelectric ceramic. Impedance mismatch between the 75 ohm high frequency cable and the pulser/receiver (50 ohm) was present in the ultrasonic measurement system. The arrows indicate the first deflection of the P or S wave arrival. The hatched area represents the region of uncertainty in picking the S wave arrival.

There are several interfaces, perpendicular to the propagating wave, present in the uniaxial and hydrostatic sample assembly. It is important to understand how these interfaces contribute to the P and S wave measurements. To understand the effects of reflections from interfaces perpendicular to the propagating direction, the mild steel sample was cut into two parts and then into four parts (Figure 2-25) to produce one and three additional interfaces in the sample. The cut interfaces were squared and ground until a surface finish of approximately 0.1Ra was achieved. In the case of the uncut mild steel sample, the S wave seen after the first arrival is the S wave that is reflected from the receiving end and then reflected again from the pulsing end (Figure 2-26). As more interfaces are created, the number of reflected S waves increased as seen in the S-S trace. The reflected P waves are much more difficult to see because the P to S and S to P wave conversions are greater in the P-P traces.

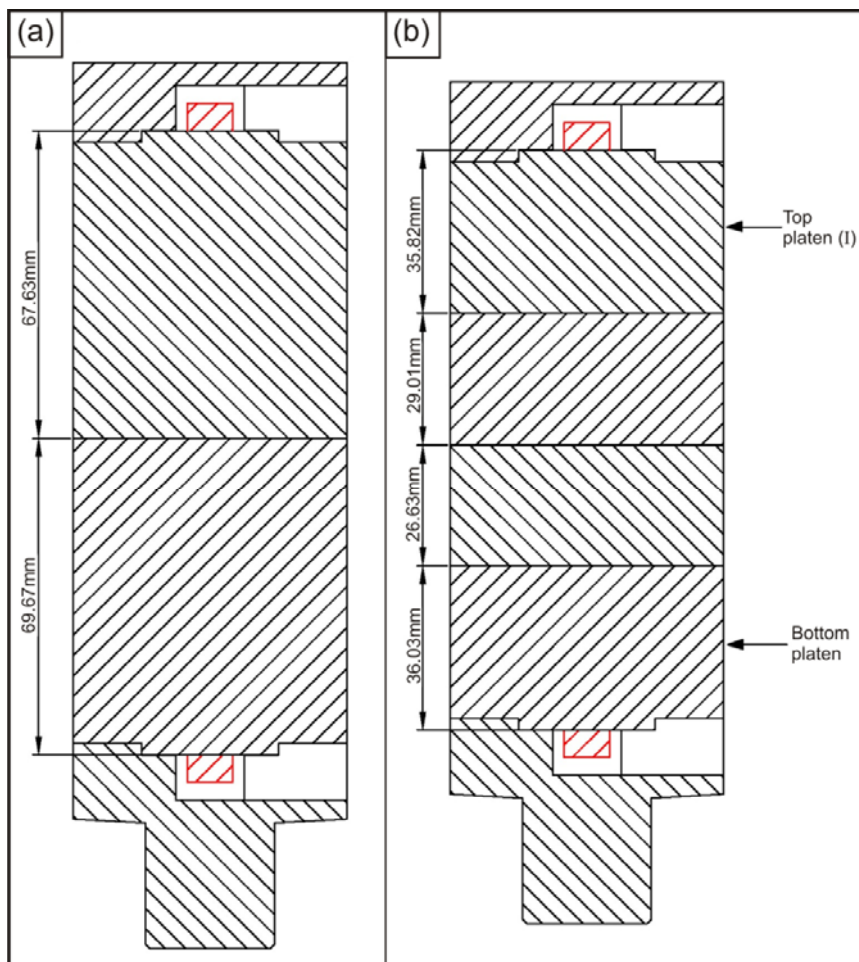


Figure 2-25. Mild steel sample cut into two (a) and 4 (b). Top platen (I) and top platen (II) are components of the uniaxial apparatus.

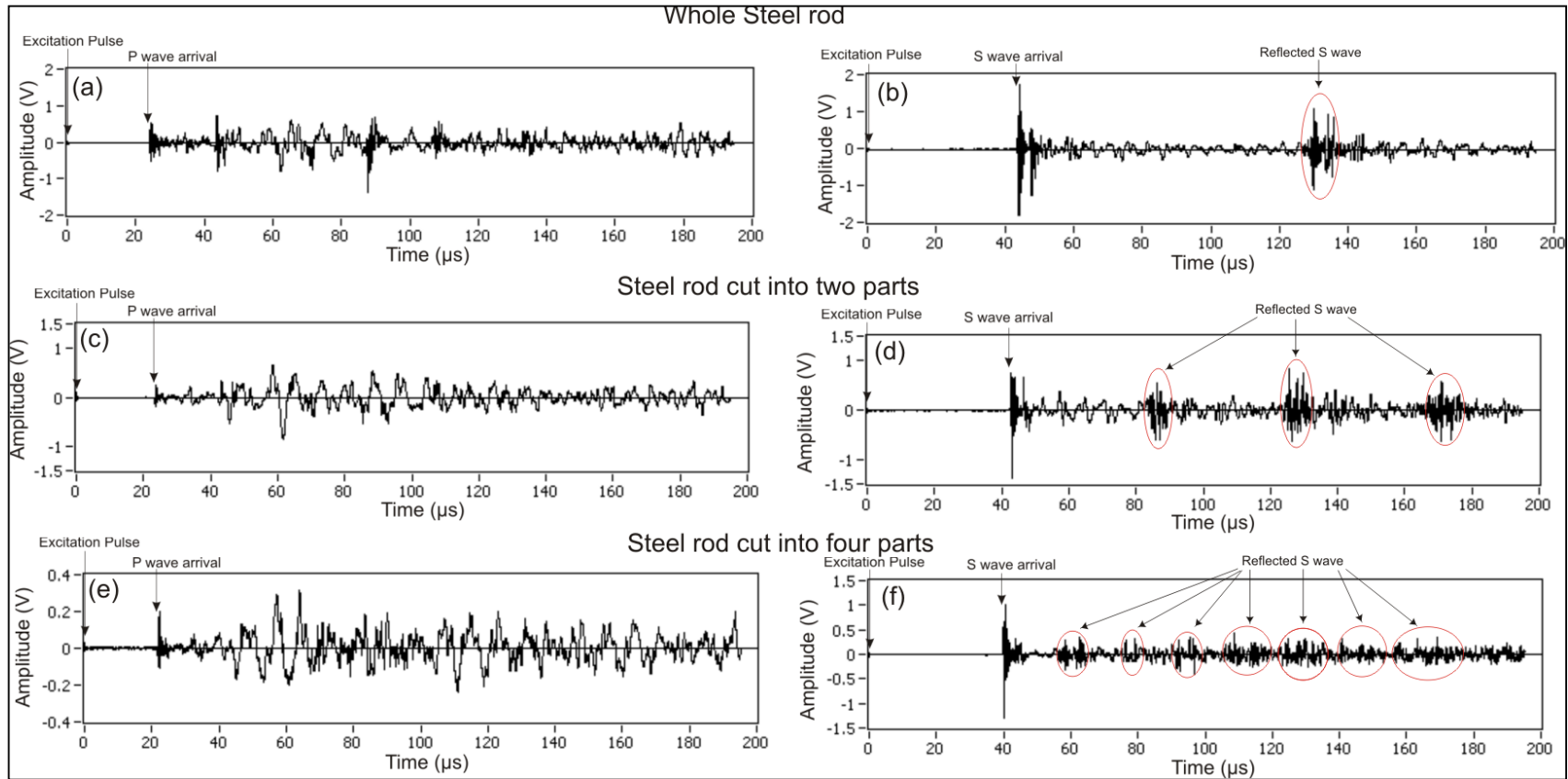


Figure 2-26. P-P traces (left) and S-S traces (right) of the mild steel uncut, cut into two parts, and cut in four parts.

2.6.2 S wave misorientation

The S wave arrival amplitude is affected when the polarization direction of the pulsing and receiving S wave are not in the same plane. The term misorientation in this context refers to the angle between the polarization direction of the pulsing S wave piezoelectric ceramic and the polarization direction of the receiving S wave piezoelectric ceramic. Misorientation occurs when the top platen is rotated and the bottom platen is fixed or vice versa. During rotation, the pulsing P and S wave piezoelectric ceramic are no longer aligned to the receiving P and S wave piezoelectric ceramic respectively. However, this misalignment does not affect the P and S wave arrival time. Misorientation affects the amplitude of the S wave arrival severely (Figure 2-27).

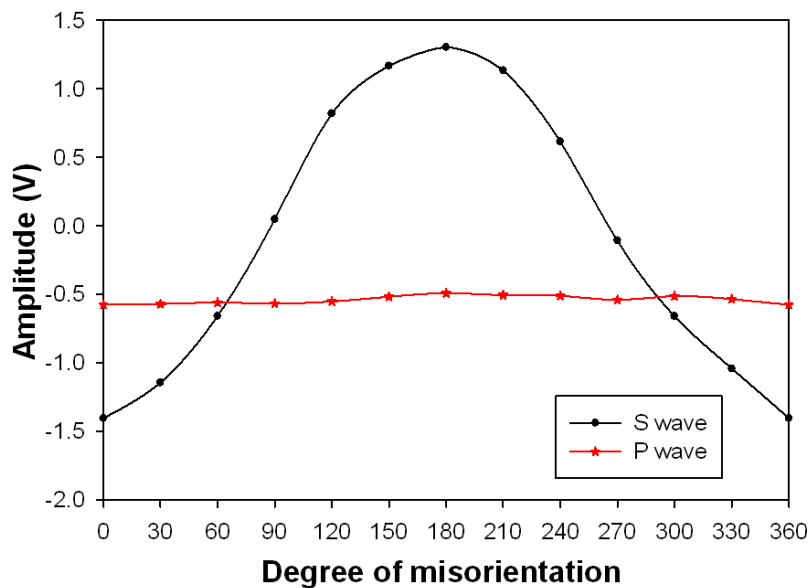


Figure 2-27. Amplitude of the first maximum of P and S wave arrival during rotation of the top platen (I) and keeping the bottom platen fixed. Misorientation is the angle between the polarization direction of the pulsing S wave and the polarization direction of the receiving S wave.

2.6.3 Elastic wave Coupling

Contact or coupling between the specimen and the top and bottom platens is important for reliable ultrasonic measurement (Krautkramer and Krautkramer, 1990; Szilard, 1982). For the platens and the test specimen to be in good contact, it is important that the test specimen and platens be ground at both ends to achieve a surface finish of approximately 0.1Ra or better, and the entire setup should be squared. A non-uniform air gap between the platens and the test specimen will alter the transmission characteristics of the ultrasonic waves. To reduce the effect of a non-uniform air gap, an elastic wave couplant such as water, glycerin, grease, petroleum jelly, or oil can be used (Krautkramer and Krautkramer, 1990). The elastic wave couplant should be kept as thin as possible, as increasing the thickness will degrade the transmitted signal. The differences in the P and S wave arrivals can be easily observed from testing the signal from the top and bottom platens with and without elastic wave couplant as shown in Figure 2-28. The elastic wave couplant used in this case was multi-purpose grease. The P wave arrival was dramatically improved with the elastic wave couplant. The elastic wave couplant did not change the S wave arrival. In fact, it made it more difficult to pick the S wave arrival as the elastic wave couplant increased the amplitude of the P to S and S to P conversion waves. Consequently, couplant was not used in our experiments.

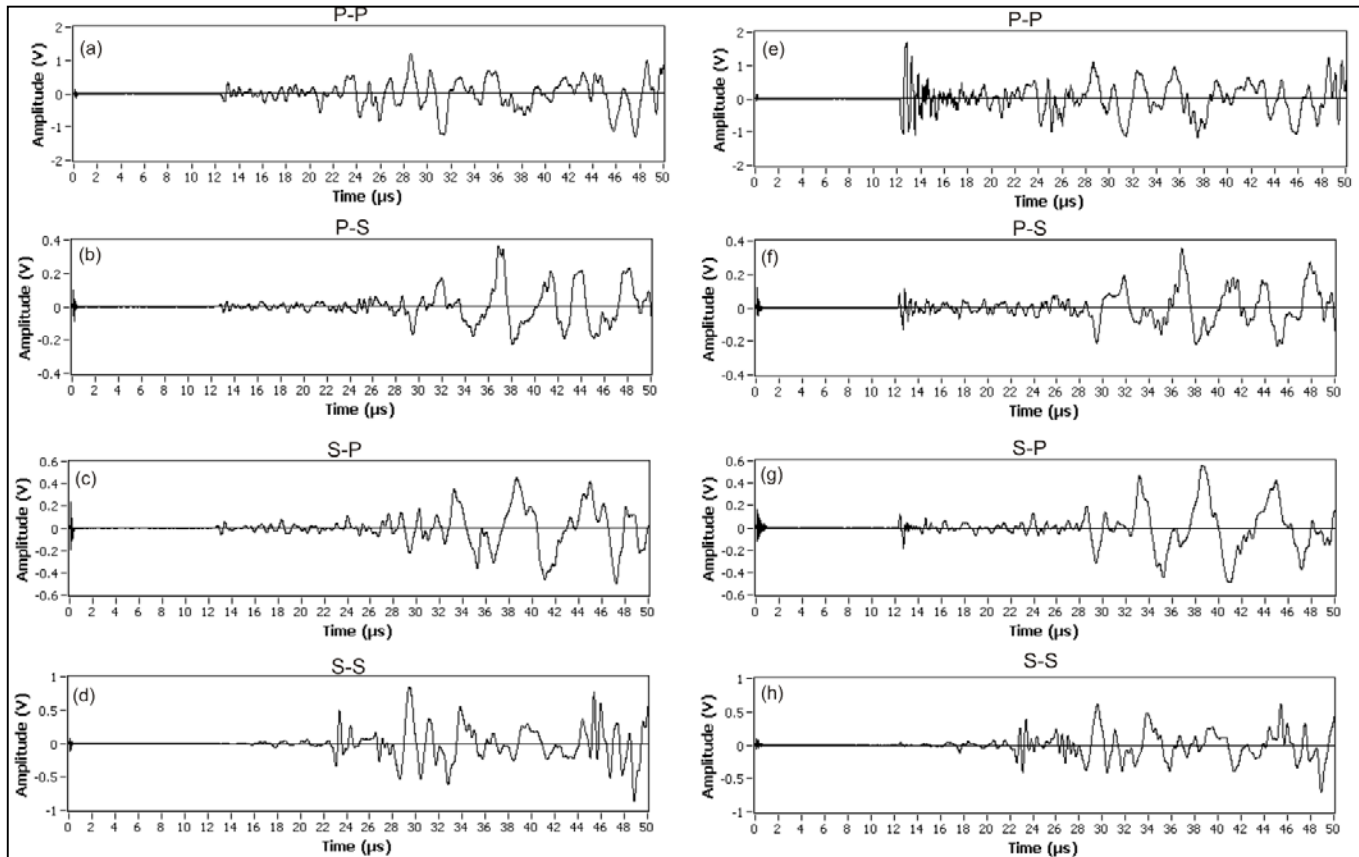


Figure 2-28. Couplant (right) vs no couplant (left) of signals from the top platen (I) and bottom platen. The couplant used is multi-purpose grease. An axial load of 70KN was applied to the top platen (I) and bottom platen.

2.7 Static and dynamic elastic property measurements

Elastic properties are essential parameters whenever stresses are measured in the crust. Static elastic properties of materials are generally obtained from the linear elastic region of the stress-strain curve. The Young's modulus, E_s , is defined as the ratio of the stress to strain in the direction of the applied stress:

$$E_s = \sigma/\varepsilon \quad \text{Equation 2-3}$$

where σ denotes applied stress and ε denotes strain. If the stress-strain curve is non-linear but exhibit perfect elasticity then the Young's modulus is defined as secant (E_{sec}) or tangential modulus (E_{tan}). Perfect elasticity implies that, during loading and unloading, the same path is followed. Hence the energy stored in the specimen during loading will be released during unloading. The secant modulus is defined as the ratio of the total stress to the total strain,

$$E_{\text{sec}} = \sigma/\varepsilon . \quad \text{Equation 2-4}$$

The tangent modulus is defined as the local slope of the strain-strain curve

$$E_{\text{tan}} = d\sigma/d\varepsilon . \quad \text{Equation 2-5}$$

The Poisson's ratio is defined as the ratio of radial strain to axial strain,

$$\nu_s = - \varepsilon_{\text{radial}} / \varepsilon_{\text{axial}} . \quad \text{Equation 2-6}$$

Equations 2-3 to Equation 2-6 assume homogeneous strain.

Strain gauges (from Tokyo Sokki Kenkyujo Co., Ltd; gauge type PFL-10-11 and PFL-20-11 for radial and axial measurements respectively) were used to measure axial and radial strains. The axial strain is measured in the direction parallel to the uniaxial loading direction, while the radial strain is measured in the direction perpendicular to the uniaxial loading direction (Figure 12c). The strain gauges are glued to the sample using a P-2 adhesive (from Tokyo Sokki Kenkyujo Co., Ltd). The axial and radial strain gauges are wired in a Full Wheatstone Bridge configuration (Figure 2-29). The Wheatstone Bridge is excited with a stabilized DC supply. As stress is applied to the sample, a resistive change takes place in the strain gauges and unbalances the Wheatstone Bridge which results in a signal output. The resistance of the strain gauge also changes with temperature which results in an unwanted voltage change across the Wheatstone Bridge. This temperature effect is eliminated by using dummy strain

gauges alongside the active strain gauges. The dummy strain gauges are glued to a test sample which has no stress applied to it; while the active strain gauges are glued to a test sample on which the experiment is conducted.

Dynamic elastic properties are derived from the travel time of seismic or ultrasonic wave. The Young's modulus, E_D , and Poisson's ratio, ν_D , can be estimated from the well-known relationships of isotropic materials as follows (Kuttruff, 1991):

$$E_D = \frac{\rho V_s^2 (3V_p^2 - 4V_s^2)}{V_p^2 - V_s^2} \quad \text{Equation 2-7}$$

$$\nu_D = \frac{V_p^2 - 2V_s^2}{2(V_p^2 - V_s^2)} \quad \text{Equation 2-8}$$

where V_p is the P wave velocity, V_s is the S wave velocity and ρ is the density of the rock. In most cases, there is a difference between the static and dynamic elastic properties (see chapter 3).

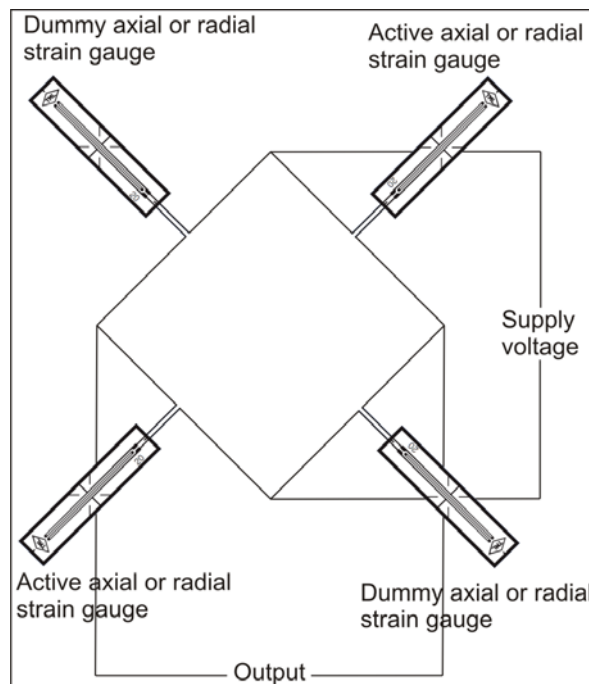


Figure 2-29. Full Wheatstone Bridge configuration for axial and radial strain measurement.

2.8 P and S wave, and shear wave splitting velocity measurement

The P and S wave travel times through the platens need to be accounted for when determining the travel time through the test sample. In the case of the uniaxial sample assembly setup, the P and S travel times through the platens are measured by placing the bottom platen against the top platen (I or II). Due to the fact that the diameter of platens are larger than the test sample, a sample made of the same material as the platen (mild steel), that has the same dimensions as the test sample is placed between the platens to create the same stress conditions taking into account the length changes of the platens as a function of differential stress. (Figure 2-30). The change in the P and S wave travel times are very minimal as shown in Figure 2-31 and Figure 2-32. In the case of the hydrostatic sample assembly setup, the P and S travel times through the platens are measured by placing the top platen against the bottom platen. The change in the P and S wave travel times are also very minimal as a function of confining pressure as shown in Figure 2-33. The P and S wave velocities of the test sample are calculated by dividing the length of the rock sample (L) by the travel time through the rock sample (t), corrected for travel time through the platens (t_p):

$$V_p \text{ or } V_s = L / (t_{pr} - t_p) \quad \text{Equation 2-9}$$

where V_p is the P wave velocity, V_s is the S wave velocity and t_{pr} is arrival time through the platens and rock sample.

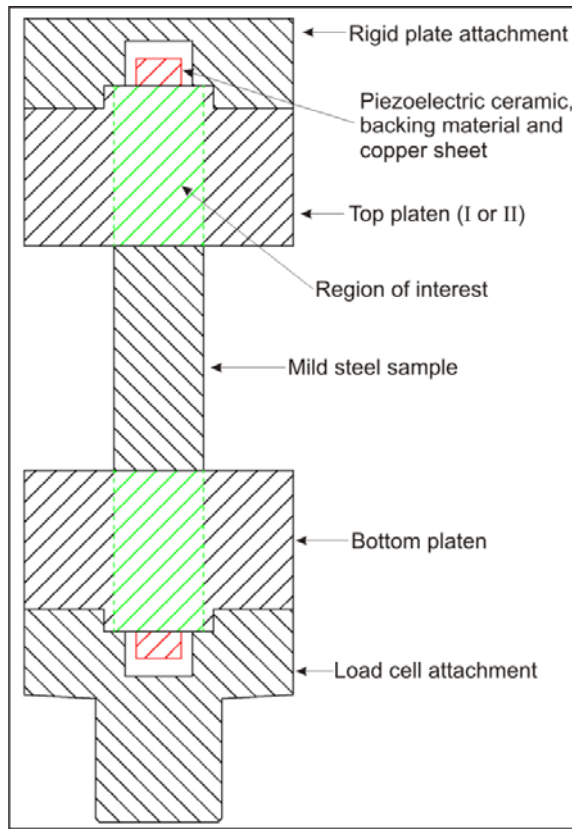


Figure 2-30. Platen region of interest of the uniaxial sample assembly. Mild steel sample of the same deminsion as the test samples is placed between the top (I or II) and bottom to account for changes in the length of the region of interest as a function of differential stress.

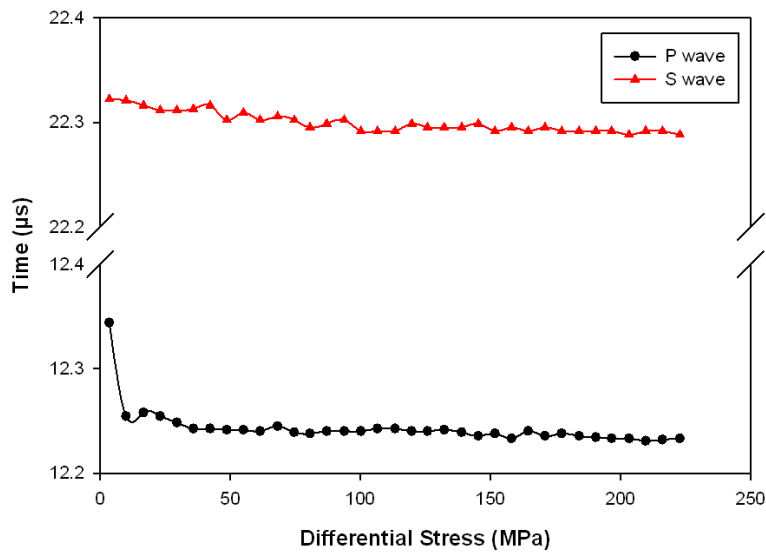


Figure 2-31. P and S wave travel times through the top platen (I) and bottom platen as a function of differential stress.

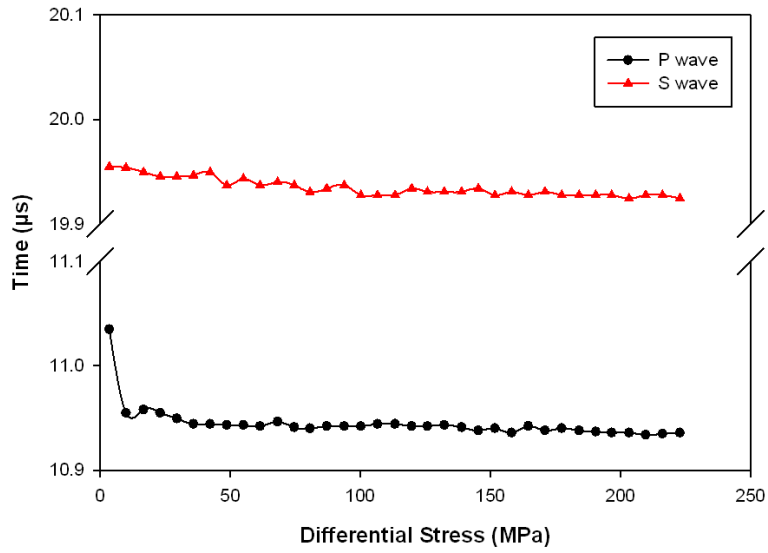


Figure 2-32. P and S wave travel times through the top platen (II) and bottom platen as a function of differential stress.

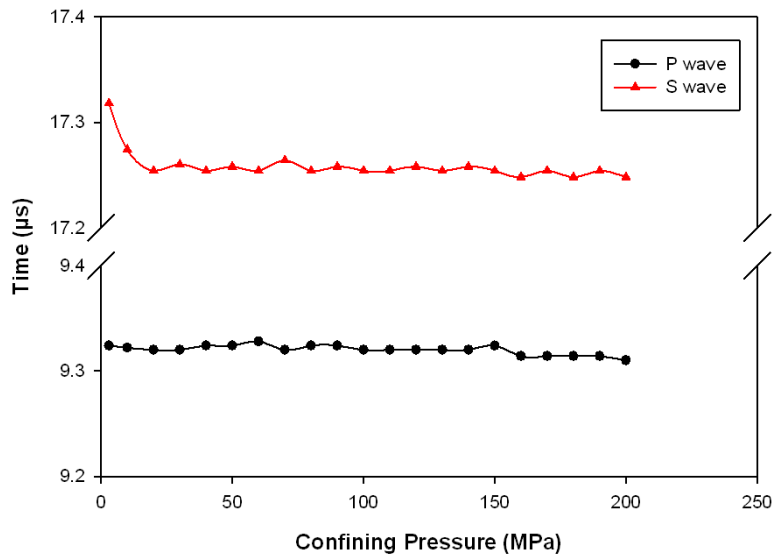


Figure 2-33. P and S Travel time through the top and bottom platens as a function of confining pressure.

Shear wave splitting is the phenomenon that occurs when a S wave enters an anisotropic rock. The incident shear wave splits into orthogonally polarized fast and slow shear waves (Figure 2-34). The faster S wave is oriented parallel to the cracks or crystals' alignment if the crystals are elastically anisotropic. The measurements of shear wave splitting reflect the degree of anisotropy and leads to a better understanding of the rock's crack density and orientation or crystal lattice alignment (Aki and Richards, 2002).

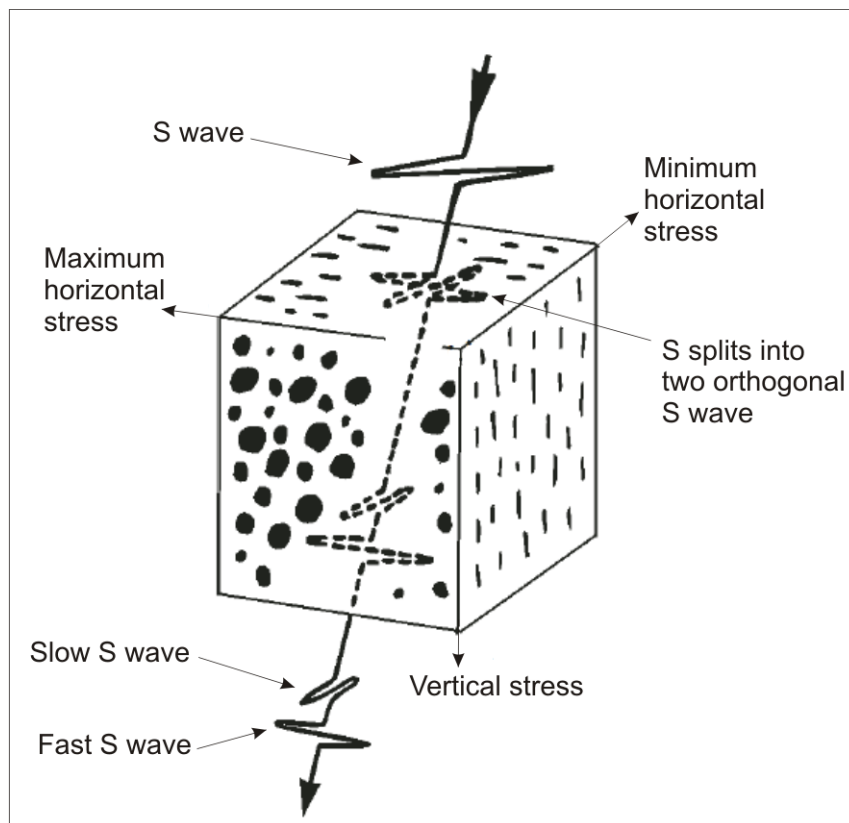


Figure 2-34. Schematic illustration of shear-wave splitting in stress-aligned cracks. (after Crampin et al., 2008)

The uniaxial and hydrostatic sample assembly can be used to measure shear wave splitting. Shear wave splitting can be measured by pulsing with a S wave piezoelectric ceramic that is polarized and aligned in the same plane as the receiving S wave piezoelectric ceramic, and then rotating the test sample to identify the fast and slow S waves. This setup records both the fast and slow waves but the arrival of the slow wave is difficult to locate. Figure 2-36 to 3-38, show examples of shear wave splitting in a mylonitic gneiss sample from

Chimparra Formation, north Spain. The mylonitic gneiss sample is composed of biotite, garnet, opaques, plagioclase, and quartz. Three orthogonal cores (1B, 2B, and 3B) were taken from the mylonitic gneiss sample. The mylonitic gneiss 3b core is perpendicular to the foliation within the sample. Shear wave splitting can also be measured by pulsing with a S wave piezoelectric ceramic that is polarized 45° to the polarization direction of the receiving S1 and S11 wave piezoelectric ceramic (Figure 2-35). One of the receiving piezoelectric ceramic will receive the fast S wave while the other will receive the slow S wave. Figure 2-39 shows an example of shear wave splitting in a Westerly granite sample that has induced microcrack damage parallel to the axial loading direction.

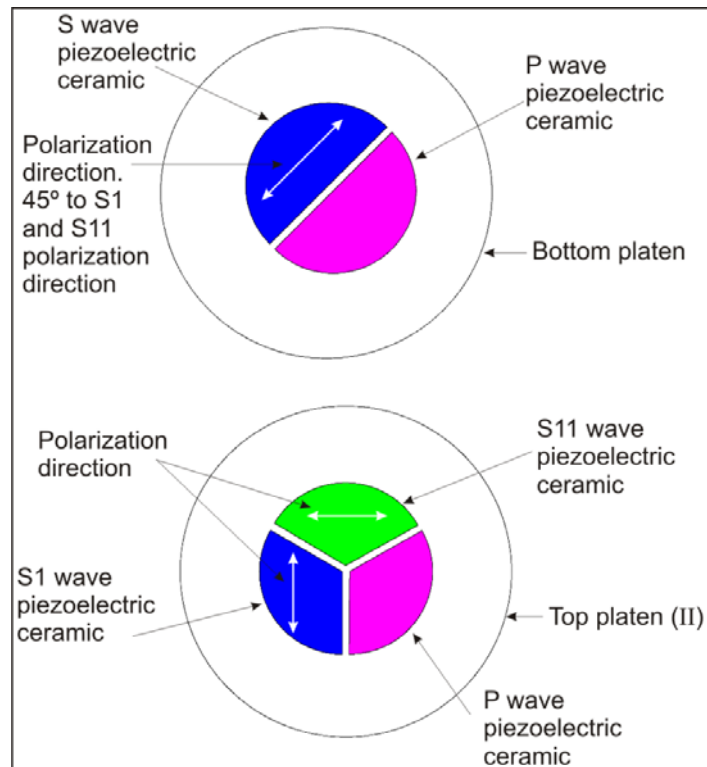


Figure 2-35. S wave piezoelectric ceramics arrangement for shear wave splitting measurement. Pulse with S wave piezoelectric ceramic on bottom platen. Receive with S1 and S11 piezoelectric ceramics on top platen (II).

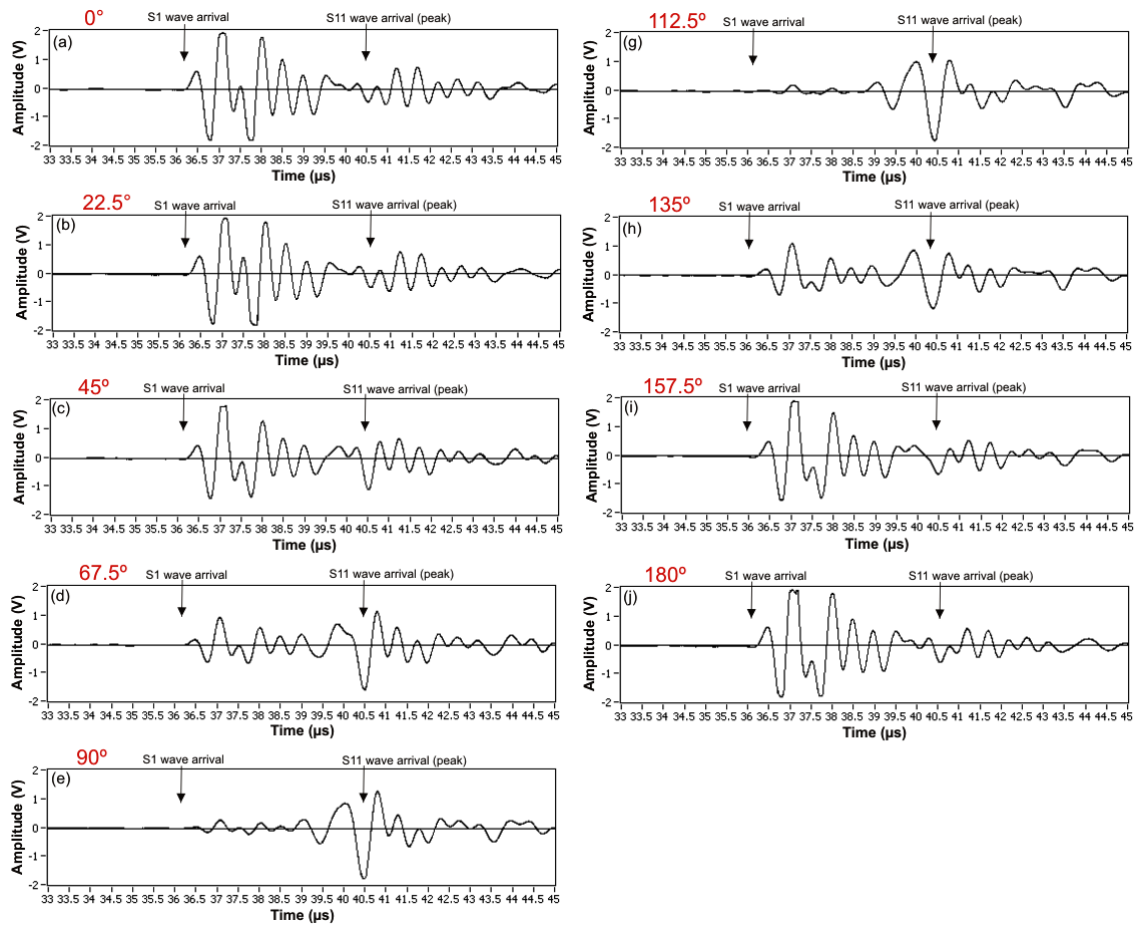


Figure 2-36. S-S traces of shear wave splitting of mylonitic gneiss 1B. The waveform changes as the sample is rotated between 0° and 180° . The fast S wave (S1) can be accurately picked at the first deflection. The slow S wave (S2) can be picked at the first maximum. In some traces the fast or slow wave is within the noise level and cannot be seen.

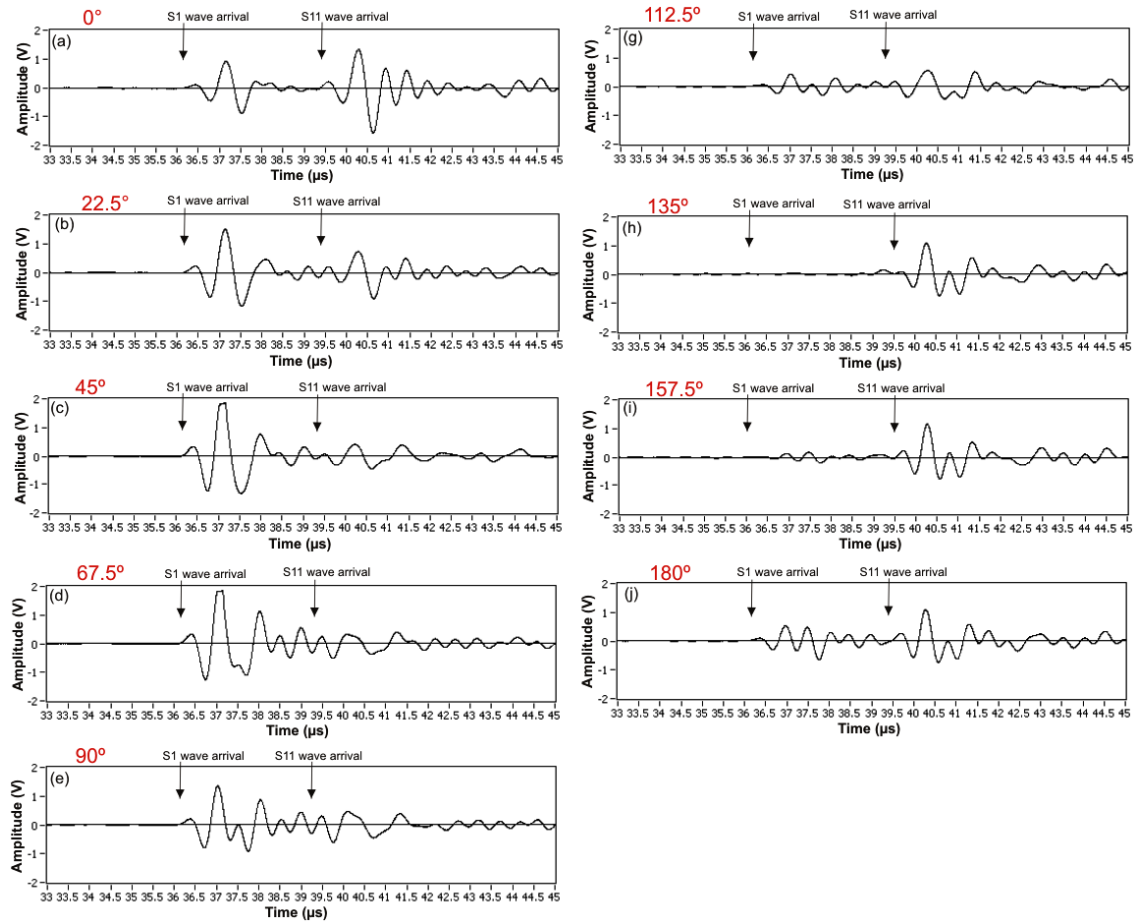


Figure 2-37. S-S traces of shear wave splitting of mylonitic gneiss 2B. The waveform changes as the sample is rotated between 0° and 180°. The fast S wave (S1) and slow S wave (S2) can be accurately picked at the first deflection. In some traces the fast or slow wave is within the noise level and cannot be seen.

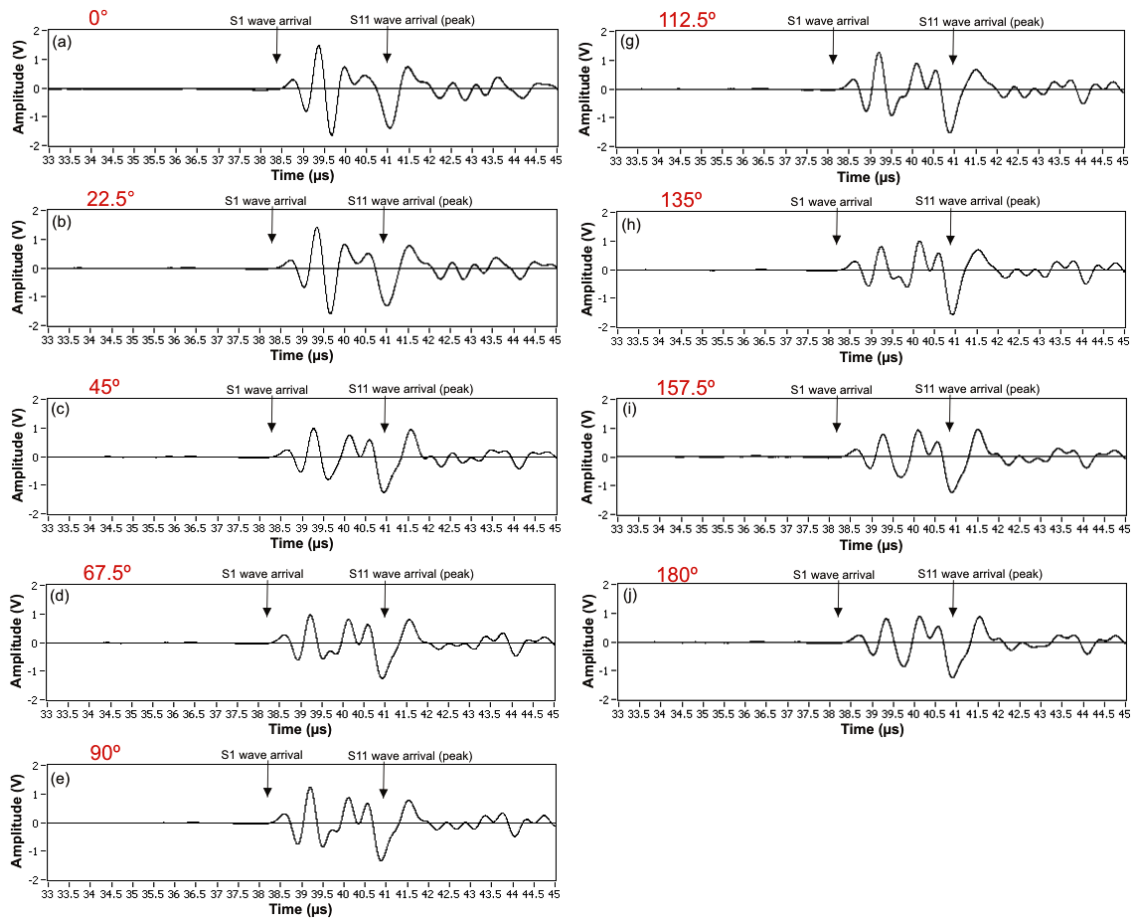


Figure 2-38. S-S traces of shear wave splitting of mylonitic gneiss 3B. The waveform changes as the sample is rotated between 0° and 180° . The fast S wave (S1) can be accurately picked at the first deflection. The slow S wave (S2) can be picked at the first maximum.

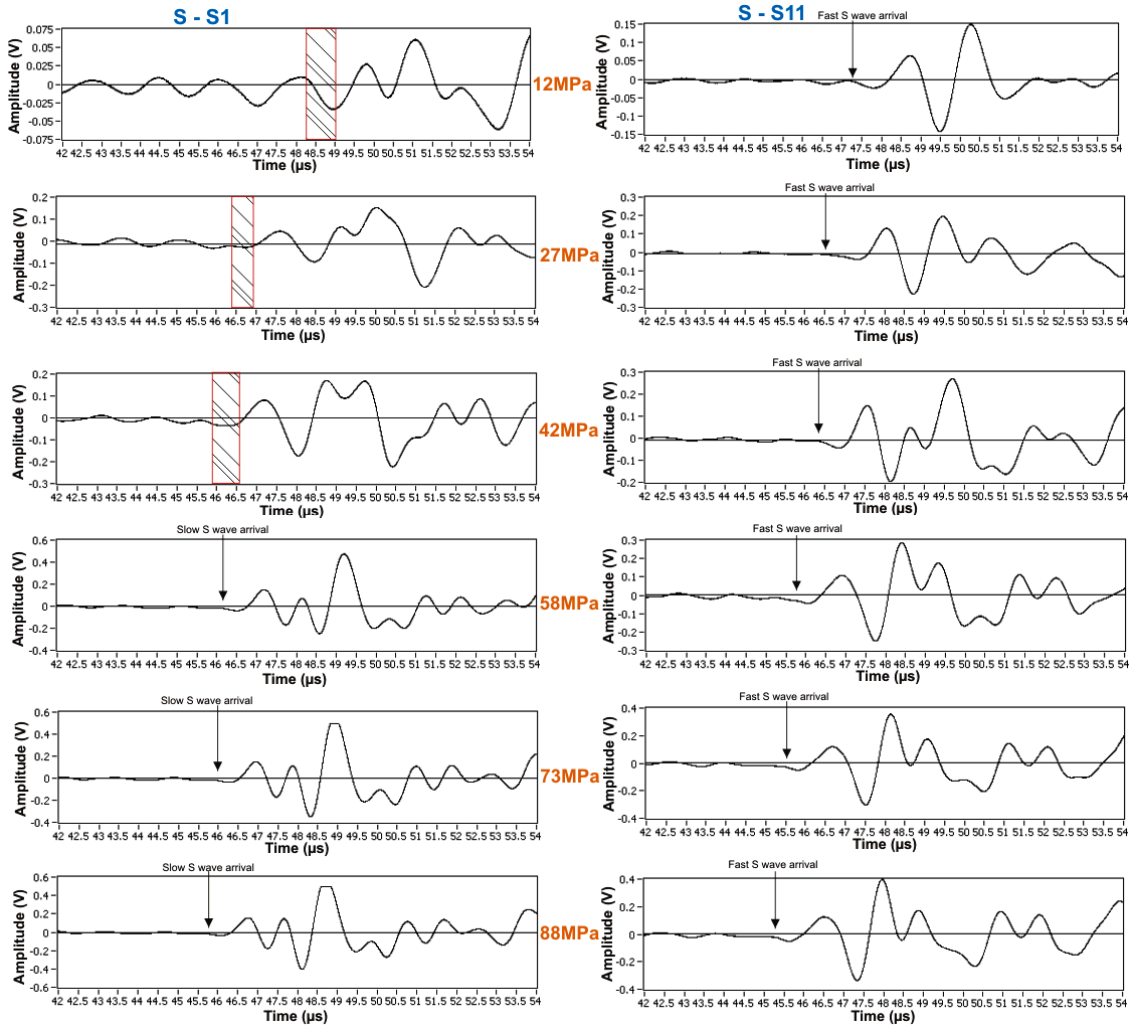


Figure 2-39. Shear wave splitting of Westerly granite with microcracks oriented parallel to the axial loading direction. S-S1 traces are on the left. S-S11 traces are on the right. The Westerly granite sample with induced microcrack damage was taken up to 88MPa differential stress. The hatched area represents the region of uncertainty in picking the slow S wave arrival. The difference between the fast and slow wave arrival times increases as the differential stress increases.

2.9 Attenuation measurement

Attenuation is the decrease of amplitude of a signal as a function of time and distance. Absolute measurement of attenuation is a formidable task as seismic wave attenuation in rocks consist of intrinsic attenuation (absorption of energy through conversion into heat due to interaction between the propagating wave and the rock) and extrinsic attenuation (the lost of energy due to beam spreading, transmission loss and scattering). Intrinsic attenuation is of great importance because it can give additional information on the physical properties of rocks (permeability, crack damage, degree of saturation, type of saturant, etc). The range of Q factor values in crystalline rocks from laboratory and seismic experiments is scarce. Moreover, a knowledge of Q factor in crystalline rocks is important because the use of high-resolution seismic methods is becoming increasingly common in such rocks for engineering, environmental and mining purposes (Juhlin, 1995; Milkereit et al., 1994). The two main techniques used to measure seismic attenuation in the laboratory are the spectral ratio and the rise time techniques. The spectral ratio technique relies on the fact that signal amplitude decreases with increasing frequency more rapidly for a lossy medium than for an ‘elastic’ reference. The rise time technique compares the pulse rise time of a signal before it enters a lossy medium to the pulse rise time of a signal passing through the lossy medium. The quality factor, Q (Equation 2-13), which is dimensionless, is used as a measure of attenuation. The higher the Q factor, the less attenuating the rock.

2.9.1 The spectral ratio technique

In the procedure outlined by Toksoz et al. (1979), the amplitudes of plane seismic waves for the reference and the sample are expressed as:

$$A_1(f) = G_1(x)e^{-\alpha_1(f)x}e^{i(2\pi ft - K_1x)} \quad \text{Equation 2-10}$$

and

$$A_2(f) = G_2(x)e^{-\alpha_2(f)x}e^{i(2\pi ft - K_2x)} \quad \text{Equation 2-11}$$

where A is the amplitude, f is the frequency, x is the distance, $K = 2\pi f/v$ is the wave number, v is velocity and $G(x)$ is a geometrical factor which includes beam spreading, reflections etc., and $\alpha(f)$ is the frequency dependent attenuation

coefficient. The subscripts 1 and 2 refer to the reference and the sample respectively. It is assumed that α is a linear function of frequency, although the method itself tests this assumption (Jackson and Anderson, 1970; Knopoff, 1964; McDonal et al., 1958).

According to *Toksöz et al. (1979)*, the following relationship can be established:

$$\alpha(f) = \gamma f \quad \text{Equation 2-12}$$

where γ is a constant and is related to the quality factor, Q, by

$$Q = \pi/\gamma\nu \quad \text{Equation 2-13}$$

When the same geometry is used for both the sample and reference (i.e. same sample dimensions, piezoelectric ceramic holders, and arrangements), then G_1 and G_2 are frequency-independent scale factors. The ratio of the Fourier amplitudes is

$$\frac{A_1}{A_2} = \frac{G_1}{G_2} e^{-(\gamma_1 - \gamma_2)fx} \quad \text{Equation 2-14}$$

or

$$\ln\left(\frac{A_1}{A_2}\right) = (\gamma_1 - \gamma_2)xf + \ln\left(\frac{G_1}{G_2}\right) \quad \text{Equation 2-15}$$

When G_1/G_2 is independent of frequency, $(\gamma_2 - \gamma_1)$ can be found from the slope of the line fitted to $\ln(A_1/A_2)$ versus frequency (Figure 2-40b and d). If the Q of the standard reference is known, γ_2 of the sample can be determined. When the Q of the standard is high (i.e. $Q \approx \infty$), then $\gamma_1 = 0$, and γ_2 of the rock sample can be determined directly from the slope. In fact, a reference material with a Q factor value greater than 1000 introduces an into error γ_2 of less than 1%. A more serious concern is the validity of the assumption that the geometric factors G_1 and G_2 have the same frequency dependence, and G_1/G_2 is independent of frequency. With polished rock surfaces and good coupling between the piezoelectric ceramic holder and sample, one would not expect frequency-dependent reflection coefficients at the interface.

In our calculation of the Q factor, the linear region is taken in the 0.8MHz – 1.7MHz frequency range. A Hanning window was applied to the averaged signals to minimize Gibbs’ phenomenon (a distortion or leakage due to discontinuities in the frequency domain) (Hamming 1977). Fast Fourier transform is then performed on the first 2 periods of the P and S wave arrivals, of the reference and sample (Figure 2-40a and c).

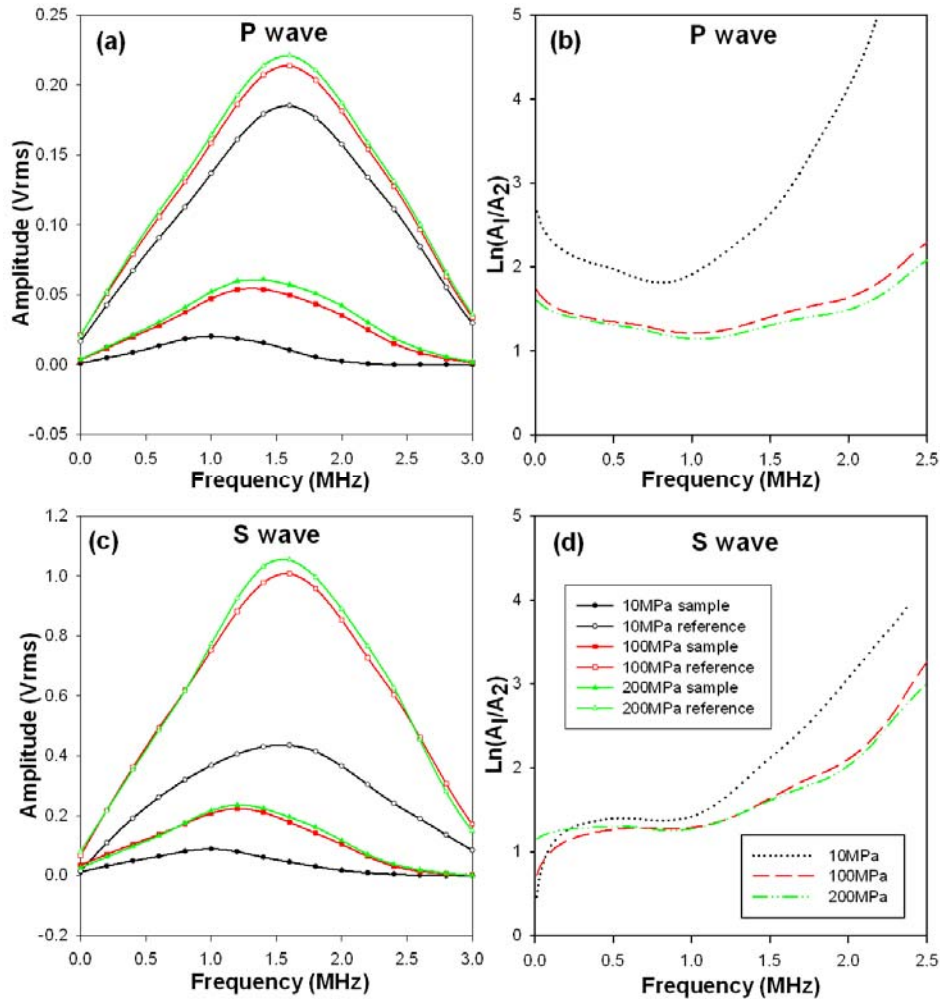


Figure 2-40. Attenuation characteristics of the sample and reference at different hydrostatic confining pressure. Left: The magnitude of the fast Fourier transform of the first 2 periods of the P (a) and S wave (c) arrivals. Right: The spectral amplitude ratio of the reference to the sample of the P (b) and S wave (d). The linear portion is taken between 0.8MHz to 1.7MHz where a linear least square fit line is drawn through the data points. This verifies the linearity assumption made in the calculation.

2.9.2 The Rise Time Technique

The pulse rise time, τ , is defined as the interval between the intersections of the tangent of the point of the maximum slope, extrapolated to zero and to peak pulse amplitude (Figure 2-41) (Gladwin and Stacey, 1974). This accounts for the broadening of the signal as it propagates through a rock sample.

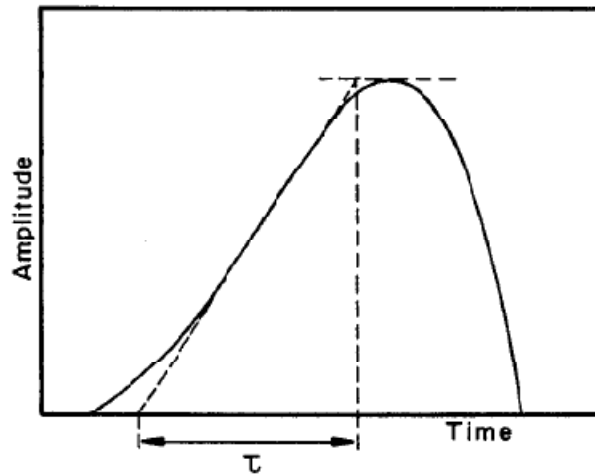


Figure 2-41. The rise time, τ , of a typical wave. (after Gladwin and Stacey, 1974)

Gladwin and Stacey (1974) related the rise time, τ , of the received signal and the quality factor, Q :

$$\tau = \tau_0 + CT/Q \quad \text{Equation 2-16}$$

where τ_0 is the initial rise time (for $T = 0$), T is the travel time of wave propagating through the sample, and C is a constant equal to 0.53 ± 0.04 if T is in microseconds. By making Q the subject of Equation 2-16, we get:

$$Q = (\tau - \tau_0)/CT \quad \text{Equation 2-17}$$

Equation 2-16 has been discussed widely. Kjartansson (1979) showed theoretically that for a constant- Q model and for an impulse displacement source, the constant C is independent of Q for large values of Q and is equal to 0.485. If a velocity source is considered instead of a displacement source, the C -value is 0.298. Blair and Spathis (1982), have shown experimentally that: (i) τ_0 depends upon the source pulse but is not simply the source pulse risetime; (ii) C depends upon the source pulse and is also a weak function of Q , for $Q > 20$. Stewart

(1984), calculated the relations between the rise time τ of the displacement signal and the ratio T/Q for several source signals and found that $\tau = 2T/Q$ for a Heaviside source, $\tau = 0.5T/Q$ for an impulse source, and an intermediate value of C for all single polarity sources. Tarif and Bourbie (1987) found that the constants τ_0 and C depend on the absolute value of T/Q and on the initial source signal. They estimated the relative accuracies of the spectral ratio and rise time techniques and found that the spectral ratio technique is reliable and easy to implement for Q values between 5 and 50, the rise time technique enables high attenuations ($Q < 5$) to be measured, and both techniques lack precision for low attenuation ($Q > 100$). For high Q samples, the slope of the spectral ratio is low and therefore difficult to estimate accurately, whilst the rise time of the pulse is rapid and therefore also difficult to measure.

3 Quantifying and comparing the evolution of dynamic and static elastic properties as crystalline rock approaches failure during multi-cycle uniaxial loading

3.1 Abstract

Elastic properties can be measured statically where strain data are recorded and related to stress during slow unloading of a specimen, or dynamically, where the elasticity can be calculated from the velocity of P and S waves. In order to understand the elastic properties of the crust at depth using seismology, the relationship between the static and dynamic properties must be known. In this study, the dynamic and static elastic properties were measured for crystalline rock as it approaches failure. Increasing-amplitude, uniaxial cyclic loading experiments were carried out to investigate and quantify the effect of microcracking on the elastic properties, and to establish a relationship between static and dynamic measurements. Increasing-amplitude stress cycling causes an increase in the density of microcrack damage which results in a decrease in static and dynamic Young's modulus and an increase in static and dynamic Poisson's ratios as the number of cycles, and hence microfracture damage, increases. Here we compare the static and dynamic measurements during the unloading part of the stress cycling as the microfracture damage should be constant during this portion of the stress history. Stress-dependency due to opening of cracks was seen for both static and dynamic elastic properties as the sample was unloaded. The static Young's moduli are more sensitive to stress than the dynamic moduli. There is a linear relationship between static and dynamic Young's moduli, although this is not a one-to-one relationship. There is a significant discrepancy between the static and dynamic Poisson's ratios. Bulging of the sample during the experiment is affecting the static Poisson's ratio but cannot completely describe the difference seen between static and dynamic properties. The gradient and intercept of the linear relationship change as the amount of microfractures in the sample increases. We attribute the differences in the static and dynamic elastic properties to the size distribution of the crack population relative to the

amplitude and frequency of the applied stress, frictional sliding on closed cracks during loading/unloading, and the assumption of isotropic elasticity in the sample.

3.2 Introduction

Knowledge of the elastic properties is important in the characterization of rock masses in reservoir, engineering applications, and fault zone studies (e.g. Bieniawski, 1974; Bruhn et al., 1994; Caine et al., 1996; Hajnal et al., 1983; Hamiel and Fialko, 2007; Healy, 2008; Karakus et al., 2005; Saleh et al., 1996; Sukmono et al., 2006). Laboratory measurements from available cores and in situ loading test such as flat jack (Loureirpinto, 1986), Goodman jack (Heuze, 1984) and plate bearing (Coulson, 1979) tests are carried out to obtain the static elastic properties which is very time consuming, expensive and impossible for studies at crustal depths greater than ~2-3km (the typical depth limit for mines and boreholes). Elastic properties can also be derived from the travel time of seismic or ultrasonic waves. This method gives the dynamic elastic properties. The determination of dynamic elastic properties of rocks is relatively inexpensive and quick where equipment such as piezoelectric transducers, geophones and seismographs are used to measure seismic waves. However, the static response of rocks to large scale stresses can be quite different from that estimated by the seismic measurements and should be investigated further (Ciccotti and Mulargia, 2004).

Many studies aimed at establishing a relationship between both properties have been reported on in the literature. Many of the results, summarized by Lama and Vutukuri (1978), show that dynamic Young's (E_D) modulus is greater than the static Young's modulus (E_S) by amounts varying between 0 and 300% and that dynamic Poisson's ratio is also greater than the static Poisson's ratio. King (1983) reported static Young's modulus and dynamic Young's modulus at an applied uniaxial stress of 7MPa, measured on 174 igneous and metamorphic rocks samples from the Canadian Shield and found a linear relationship

$$E_S = 1.263E_D - 29.50(\text{GPa}). \quad \text{Equation 3-1}$$

The static Young's modulus was calculated from the linear elastic region of the stress-strain curve and, where a linear region could not be established, the secant values were used (see Jaeger et al., 2007, pg. 81 to 83 for details on how the static moduli may be determined).

Vanheerden (1987) found that the dynamic Poisson's ratio is smaller than the static Poisson's ratio, and the dynamic Young's modulus is greater than the tangent static Young's modulus for 10 different rock types at uniaxial stress levels up to 40MPa. They also showed that the static and dynamic Young's moduli of rocks are related by

$$E_S = aE_D^b \quad \text{Equation 3-2}$$

where a and b are stress-dependent parameters. Investigations of the dynamic Poisson's ratio are rare due to the complexity of the experimental configuration and also difficulties in determining the shear wave velocity.

Elastic properties are influenced by crack damage and state of stress within a rock (Eberhardt et al., 1999; Faulkner et al., 2006; Lau and Chandler, 2004; Martin and Chandler, 1994; O'Connell and Budiansky, 1974; Walsh, 1965a; Zimmerman, 1985). In a recent paper, Heap and Faulkner (2008) carried out stress-cycling uniaxial experiments on Westerly granite and measured elastic properties outside the linear-elastic region, quantifying the elastic property development at stresses closer to rock failure. Two effects were noted. First, it was found that increasing-amplitude stress cycling, designed to impart an ever-increasing density of microfractures to the samples, causes a gradual reduction in sample stiffness, equating to a decrease in Young's modulus (~11%) and an increase in Poisson's ratio (~43%) when compared at a constant stress level. Second, elastic properties are also seen to have a strong stress-dependency during loading (~46% increase in Young's modulus from 20 to 100 MPa).

The main objectives of the present study are to extend the study of Heap and Faulkner (2008) by measuring the static and dynamic elastic properties simultaneously during cyclic loading of crystalline Westerly granite. Hence the evolution of both elastic properties as the sample approaches failure can be quantified, and a relationship between both elastic properties can be established. The methods used during the experiments are first presented, then the results

obtained are shown. Possible explanations for the trends observed in the data are discussed, including the reasons for the differences between the static and dynamic elastic properties.

3.3 Methodology

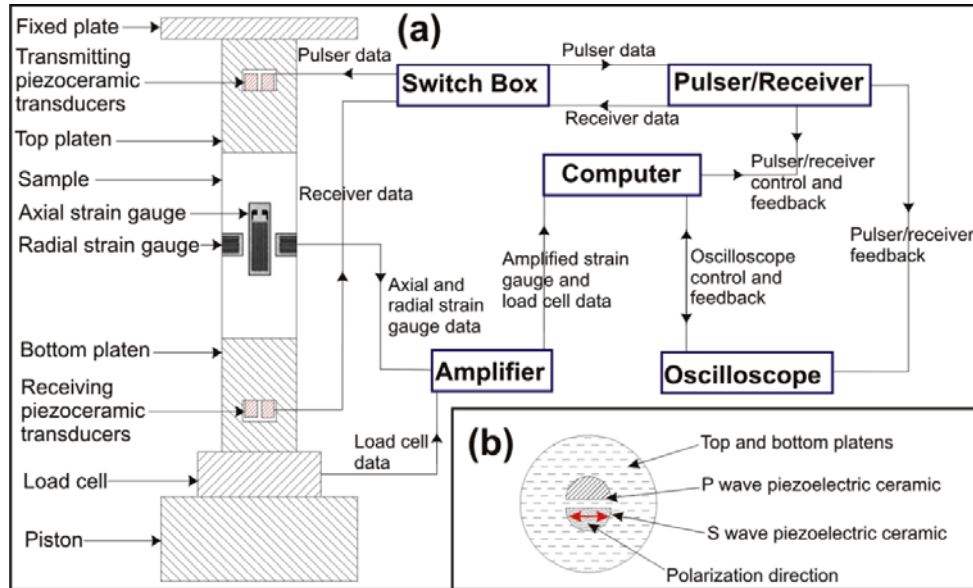


Figure 3-1. Schematic diagram of experimental arrangement (a), and arrangement of P and S wave piezoelectric ceramic within the loading top and bottom platens (b).

A standard uniaxial press was used where the sample is compressed unconfined ($\sigma_2=\sigma_3=0$) between a fixed rigid plate and a manually controlled moving hydraulic piston (see figure 3-1). Axial and radial strain gauges, wired in a Wheatstone configuration that utilized a dummy sample, were attached in the middle of the sample and used to monitor the axial and radial strain, from which the static elastic properties were calculated. Two different types of piezoelectric ceramics, one P wave and one S wave with fundamental frequency of 1.5MHz, are housed in each steel spacer. The schematic arrangement is shown in figure 3-1(b). Through transmission method was employed to measure simultaneously the P and S wave velocity of the sample in an axial direction. The pulsing P and S wave piezoelectric ceramic is aligned with receiving P and S wave piezoelectric ceramic respectively, and both S wave crystals were polarized in the same direction. Sintered stainless steel, 0.125"±0.005" thick with 0.5 micron nominal

pore size, was used as a backing material on the piezoelectric ceramic (VanValkenburg, 1983). The backing is used to control the vibration of the piezoelectric ceramic by absorbing the energy radiating from its back face. The elastic wave impedance of the backing matched the elastic wave impedance of the piezoelectric ceramic resulting in heavily damped piezoelectric ceramic that displays good range resolution with slightly lower signal amplitude. A negative spike pulser / receiver (JSR DPR300 Pulser / Receiver) was used for excitation of the piezoelectric ceramics and detection of the pulse. The choice of piezoelectric ceramics to excite or receive is manually controlled by a switch box. A 300MHz bandwidth digital oscilloscope with 20ppm time based accuracy (Tektronix TDS 3032B) is employed for recording and display of the received pulse which is synchronized with the pulser/receiver. The oscilloscope can also average up to 512 signals to reduce noise. The pulser/receiver and oscilloscope are coupled to a computer for storage of data, and processing of the recorded waveforms for analysis. The standard methodology for using ultrasonic testing to determine pulse velocities (ASTM, 1997a) was adhered to for accurate and reliable measurements of P and S wave velocities. This experimental configuration and methodology resulted in very clean elastic wave measurements from which the P and S wave arrivals could both easily be identified. (see figure 3-2 for a representative example of P and S wave arrival collected on sample WG-SDD for this study).

Increasing-amplitude cyclic loading experiments were performed on oven dry (stored at 80°C), intact Westerly granite samples under ambient laboratory conditions. Westerly granite from south-east Rhode Island, USA has low initial crack density, small grain size (average 1mm), an extensive history of laboratory testing, is generally considered to be isotropic, and can provide a high level of repeatability under carefully controlled test conditions [Lockner, 1998; Haimson and Chang, 2000]. The 20mm diameter samples were cored in a common orientation from the same block to allow results to be comparable. They were cut so their length-to-diameter ratios were in excess of 2.5 but less than 3 and precision-ground to strict tolerances (± 0.02 mm) as to the squareness of their ends (Paterson and Wong, 2005). An average of 221MPa differential stress was

taken as the unconfined compression strength (UCS) of the cored Westerly granite samples from a series of uniaxial compression tests performed on samples from the same block in the laboratory in Liverpool (see Table 1). In the first cycle, the sample was taken to $50\% \pm 4\%$ of its UCS and the stress was then reduced to zero. For the second cycle the sample was taken to $60\% \pm 4.5\%$ of its UCS and then reduced to zero. This pattern was continued until a maximum of $90\% \pm 7\%$ of its UCS was reached. Cycle number is a non-linear proxy for the amount of microfracture damage as, with each increasing stress cycle, more damage is imparted to the sample. At every $\sim 6\text{MPa}$ increment, the load was held constant for a period of ~ 10 seconds to record the P and S wave data, while the static data was recorded continuously. The loading and unloading rate was kept at $\sim 1\text{MPa}/\text{min}$. Time-dependent effects are almost negligible to the evolution of static elastic properties of dry Westerly granite for hold time up to 6 hours (Heap and Faulkner, 2008).

The elastic properties of materials are generally obtained from the ‘linear’ region of the stress-strain curve. However, the relationship need not necessarily be linear as long as there is a reproducible relationship between stress and strain, such as for a perfectly elastic material. Perfect elasticity implies that, during loading and unloading, the same path is followed. Hence the energy stored in the specimen during loading will be released during unloading. In this case there are no unique values for the elastic moduli; instead there will be a range of values corresponding to the level of stress on the specimen. Perfectly elastic behavior does not occur in rock as hysteresis is always observed, implying that some of the energy stored during loading has been dissipated into the specimen (see figure 3-3a). There is no apparent linear elastic region; the stress-strain curve changes from being concave upwards to concave downwards, hence a third-order polynomial relationship was fitted in order to capture the true form of the stress–strain loading and unloading curve with two inflexion points. The fitted curve is differentiated so that the tangent Young’s modulus can be calculated for any given stress. As there is no clear linear elastic part of the stress strain curve, we assume elasticity where the gradient of the unloading part of the stress-strain curve at any given stress is $\pm 5\text{GPa}$ to that of the next loading curve. Although there is hysteresis between the two curves, perfect elasticity is assumed (Heap

and Faulkner, 2008). The rationale is that during unloading no additional crack damage should accumulate in the sample, and this should also be true for the following loading curve, up to the point where the previous highest stress applied to the sample is reached. This assertion is supported by the Kaiser effect (Kaiser, 1950). The Kaiser effect is a well known phenomena in metallurgy and laboratory acoustic emissions (AE) studies (Holcomb, 1993; Holcomb and Costin, 1986; Kurita and Fujii, 1979; Michihiro et al., 1985; Sondergeld and Estey, 1981; Zhang et al., 1998). It refers to the observation that acoustic emissions will not occur during the reloading of a material until the stress exceeds its previous high value. The Poisson's ratio is calculated from the axial and radial strain gauge data from the same region identified above using,

$$\nu = - \epsilon_{\text{radial}} / \epsilon_{\text{axial}} \quad \text{Equation 3-3}$$

Compression and shear wave velocities are determined as the length of the sample (L) divided by the arrival time of the waves (t), corrected for travel time in the steel spacers:

$$V_p \text{ or } V_s = L/t \quad \text{Equation 3-4}$$

where V_p is the P wave velocity and V_s is the S wave velocity. From the P and S wave velocities, elastic constants such as Young's modulus, E , and Poisson's ratio can be estimated from the well-known relationships of isotropic materials as follows (e.g. Kuttruff, 1991):

$$E = \frac{\rho V_s^2 (3V_p^2 - 4V_s^2)}{V_p^2 - V_s^2} \quad \text{Equation 3-5}$$

$$\nu = \frac{V_p^2 - 2V_s^2}{2(V_p^2 - V_s^2)} \quad \text{Equation 3-6}$$

where ρ is the density. The change in the sample's density, calculated from the change in volumetric change which occurs during uniaxial compression was accounted for in the calculations.

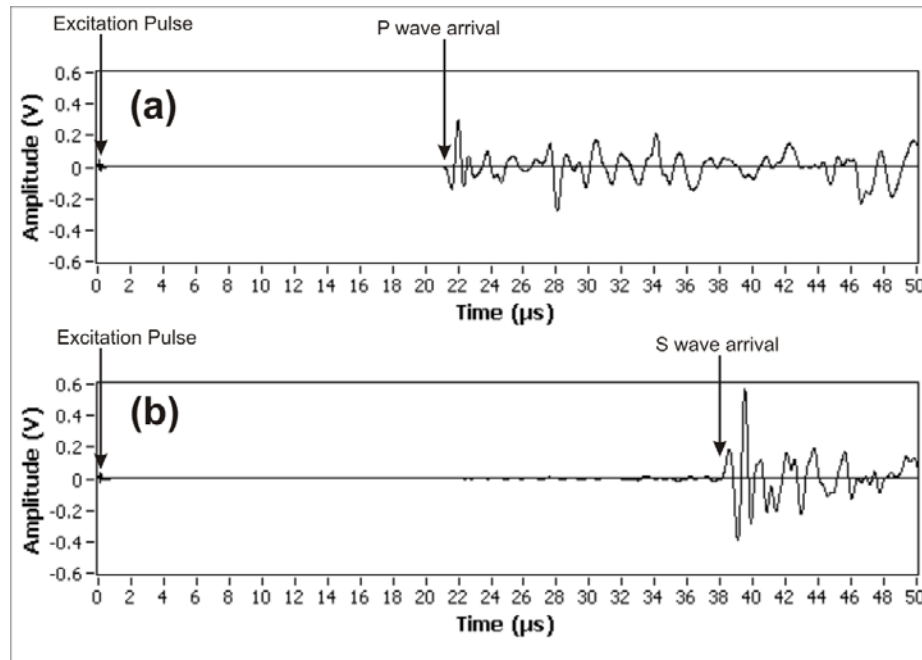


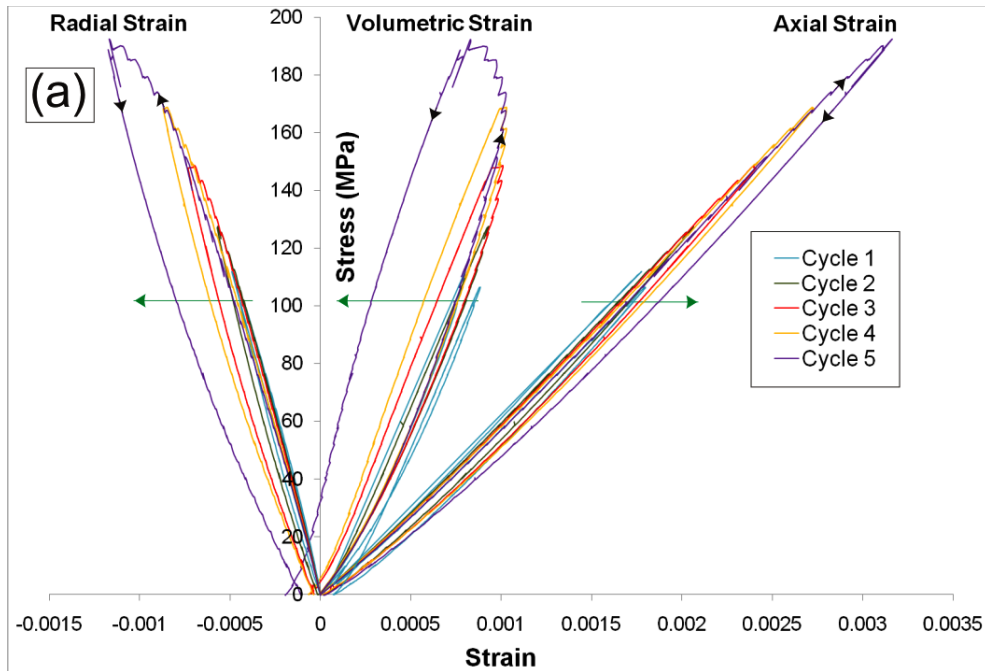
Figure 3-2. P and S wave arrival of sample WG-SDD. a) recorded trace when pulsing with P wave piezoelectric crystal and receiving with an identical P wave transducer located on the other side of the sample. b) trace obtained pulsing with S wave piezoelectric crystal and receiving with S wave transducer.

Sample	Experiment type	Failure Stress (MPa)	No. Of cycles	Note
WG-SDC	UCS	205.86	NA	To determine UCS
WG-SDB	UCS	217.88	NA	To determine UCS
WG-SDG	UCS	223.81	NA	To determine UCS
WG-SDE	UCS	239.34	NA	To determine UCS
WG-SDD	Increasing Amplitude	NA	5	For repeatability
WG-SDI	Increasing Amplitude	NA	5	For repeatability
WG-SDH	Increasing Amplitude	NA	5	For repeatability

Table 3-1. Summary of experiments.

3.4 Results

Irreversible changes occurred in the sample, as successive loading and unloading traced out different paths (see stress-strain curve in Figure 3-3a). The unloading of the sample leads to a permanent strain when the zero stress is reached. The irreversible changes in the rock sample are mainly due to the formation and growth of microcracks. The P and S wave velocities also showed the irreversible changes (Figure 3-3b). During unloading of the sample, the velocities are less than those during loading. The evolution of P and S wave velocity during loading followed the same path as the prior unloading cycle. The area bounded by the loading and unloading velocities, from 3MPa to 107MPa differential stress, shows that cycle number is a non-linear proxy for the amount of microfracture damage (as shown in figure 3-4).



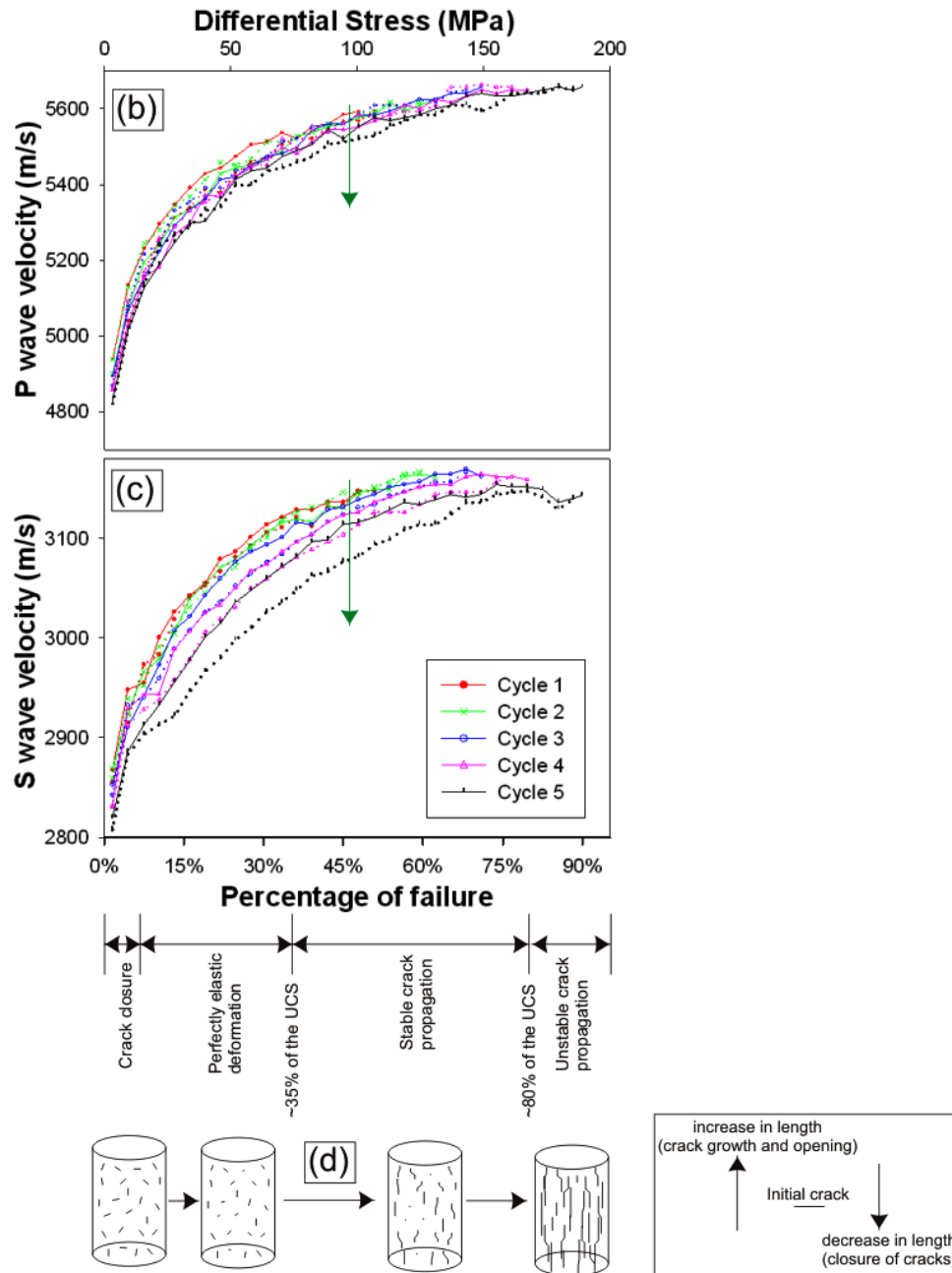


Figure 3-3. Stress-strain curve (a) and P (b) and S wave velocity (c) of sample WG-SDD under increasing-amplitude cyclic loading experiments. Green arrows indicate the change in radial, volumetric and axial strains and P and S wave velocity as the cycle number increases. Volumetric strain = axial strain + (2*radial strain). Solid and dotted lines represent loading and unloading respectively. The P and S wave velocity measurement error is less than 0.3%. The approximate positions of the stages of crack development in

brittle rock under uniaxial compression (Bieniawski, 1967a; Bieniawski, 1967b; Bieniawski, 1967c; Brace et al., 1966) are shown in (d) along with schematic illustration of crack orientation and growth.

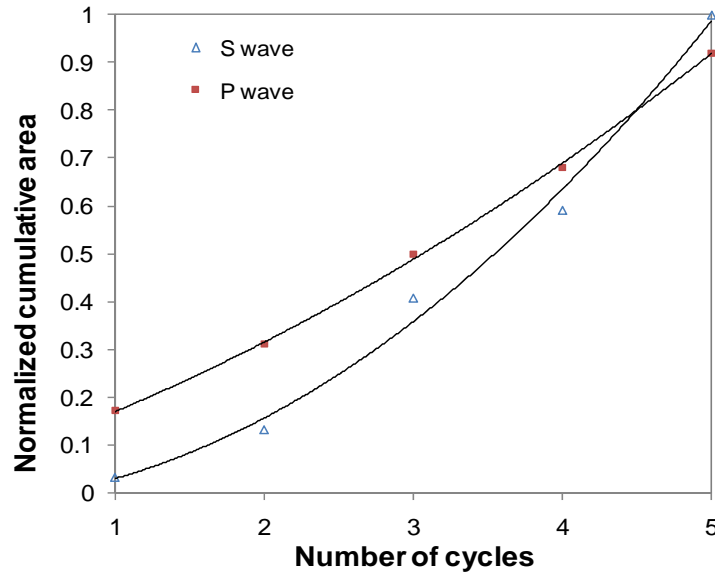


Figure 3-4. Area bounded by the loading and unloading velocity, from 3MPa to 107MPa differential stress, as a function of number of cycles. The area depicts microfracture damage.

3.4.1 Young's modulus

The typical evolution of static and dynamic Young's modulus as a function of differential stress and number of cycles is shown in figure 3-5. The static and dynamic Young's modulus shows a strong stress-dependency. If a single stress cycle is considered (e.g. cycle 3), the static and dynamic Young's moduli decreased from 71GPa to 51GPa and 66GPa to 53GPa respectively. The sample accumulated microcrack damage as the number of cycles increased which caused the Young's modulus to decrease. If the elastic properties at one stress value are compared between the first and last stress cycle (70MPa in this example), there is an overall 11% decrease in static and a 5% decrease in dynamic Young's modulus.

The comparison between the static and dynamic Young's modulus is shown in figure 3-5e and 3-5f. The static Young's modulus is greater than the dynamic Young's modulus at high differential stress. At 40MPa differential stress, during the first cycle, both Young's moduli are equal. Below 40MPa differential stress, the dynamic Young's modulus is greater than the static Young's modulus. This pattern is consistent throughout the cycles with the point of equality shifting by ~12MPa differential stress as the number of cycles increase. The most appropriate function relating the static and dynamic Young's modulus of each cycle with very high correlation (R^2 value of 0.99) is the linear function:

$$E_{(\text{static Young's modulus})} = 2.243E_{(\text{dynamic Young's modulus})} - 75.091 \text{ (GPa)} \quad \text{Equation 3-7}$$

The gradient and intercept of the linear relationship between static and dynamic Young's modulus change as the number of cycle increases (as shown in Figure 3-6).

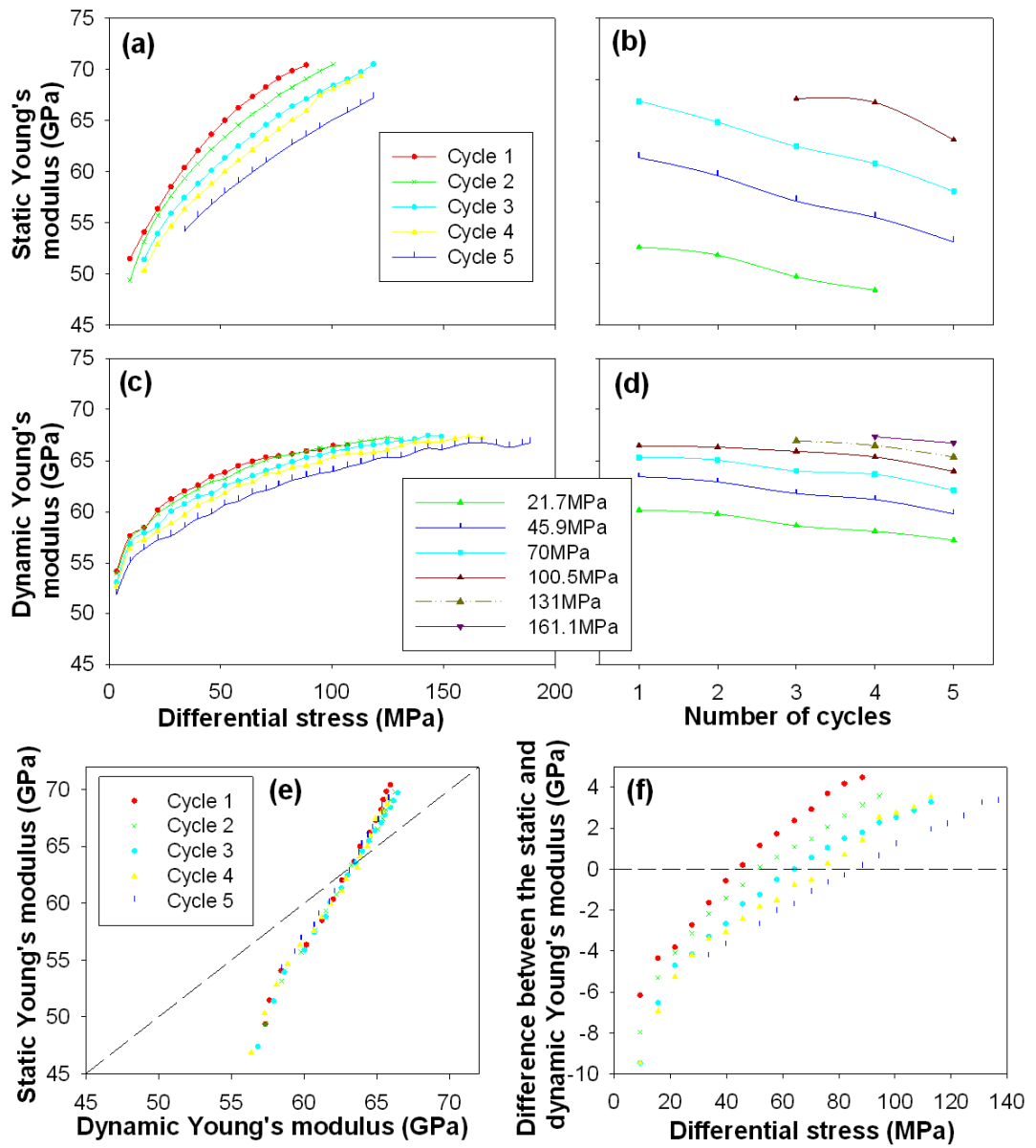


Figure 3-5. Static and dynamic Young's modulus evolution with increasing differential stress (a, c) and number of cycles (b, d) of sample WG-SDD. The static Young modulus is compared to the dynamic Young's modulus (e, f). The dash line represents line of equality.

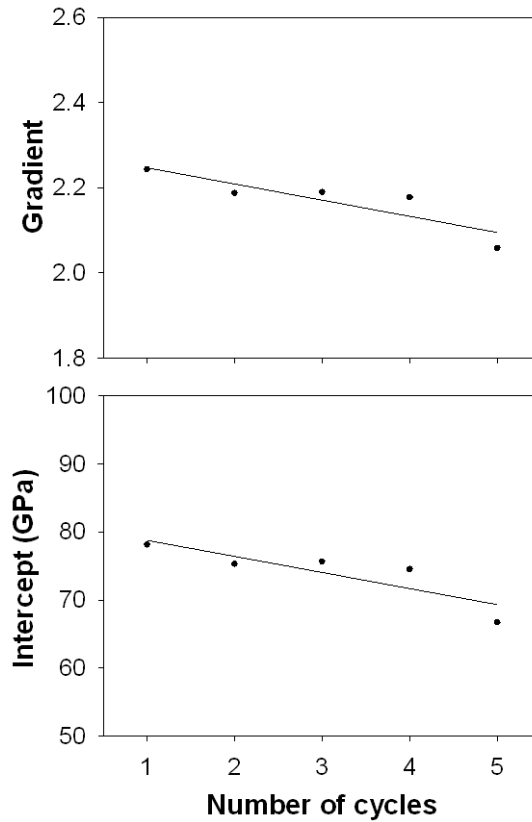


Figure 3-6. Variation of the linear relationship parameters as a function of cycles.

3.4.2 Poisson's ratio

The evolution of static and dynamic Poisson's ratio is plotted as a function of differential stress and number of cycles in figure 3-7. The static and dynamic Poisson's ratios also showed strong stress-dependency. In the first cycle, the static Poisson's ratio decreased slightly from 0.25 as the differential stress decreased to 60MPa. As the differential stress decreased below 60MPa, the static Poisson's ratio decreased rapidly to 0.18. However, the behaviour of the static Poisson's ratio is different for the other cycles. In the other cycles, the static Poisson's ratio showed an overall increase as the differential stress decreased. The dynamic Poisson's ratio decreased slightly from ~ 0.27 as the differential stress decreased to 20MPa and then decreased rapidly to 0.24 (e.g. cycle 3). The accumulation of microcrack damage within the sample caused an increase in the Poisson's ratio. If the elastic properties at one stress value are compared between

the first and last stress cycle (70MPa in this example), there is an overall 77% and 3% increase in static and dynamic Poisson's ratio respectively.

The comparison between the static and dynamic Poisson's ratio during loading of the sample is shown in figure 3-7e and 3-7f. The static Poisson's ratio is much greater than the dynamic Poisson's ratio with exception to the first cycle.

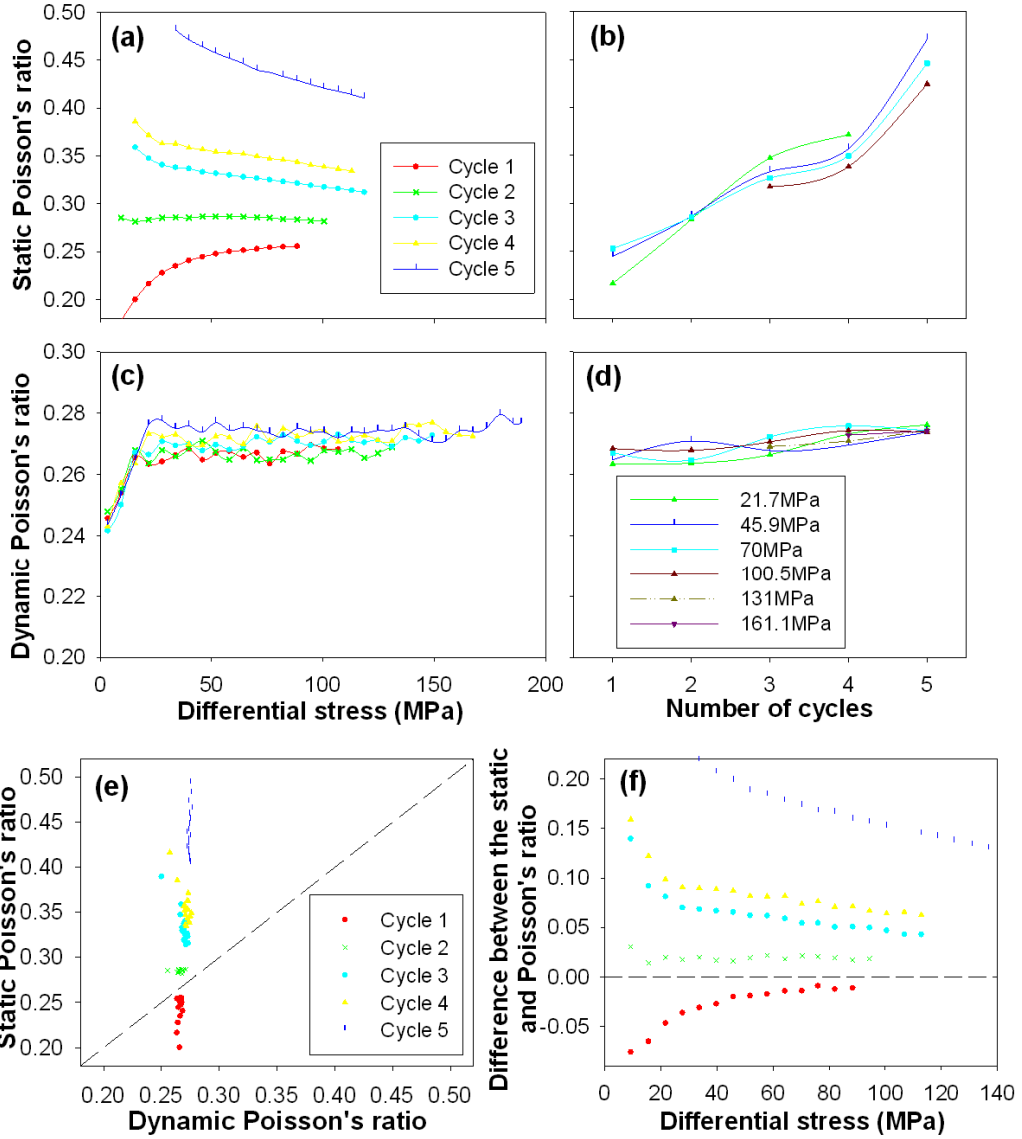


Figure 3-7. Static and dynamic Poisson's ratio evolution with increasing differential stress (a, c) and number of cycles (b, d) of sample WG-SDD. The static Poisson's ratio is compared to the dynamic Poisson's ratio (e, f). The dash line represents line of equality.

3.5 Discussion

During unloading of the sample, no additional microcrack damage was imparted, which is evident in the next loading cycle, where the P and S wave velocity generally follows the previous unloading P and S wave velocity path. This result supports our methodology of using the unloading stress-strain curve to calculate the static elastic properties. Triaxial experiment carried out by Schubnel et al. (2003) and Thompson et al. (2006) on granite samples, showed that cumulative AE increased exponentially towards failure, which strongly supports the non-linear microcrack damage accumulated in our experiment as the number of cycles increased.

The stress-dependency of the elastic properties can be explained by cracks that are oriented transversely and obliquely to the axial loading direction that are closed during loading of the sample. However, Westerly granite has a low initial crack density and has a small amount of microcracks that are obliquely and transversely orientated to the axial load direction (Heap and Faulkner, 2008).

During each cycle of the experiment, the elastic limit of the rock sample was exceeded which results in permanent deformation. The permanent deformation was mainly due to the formation and growth of microcracks. The majority of the newly initiated microcracks and crack growth are oriented in the same direction as the applied stress, which is evident in a ~1.5% decrease in S wave velocity compared to ~0.5% decrease in P wave velocity; as the S wave is polarized normal to the loading direction. This is also corroborated by thin section analysis done by Heap and Faulkner (2008) (see Figure 3-8).

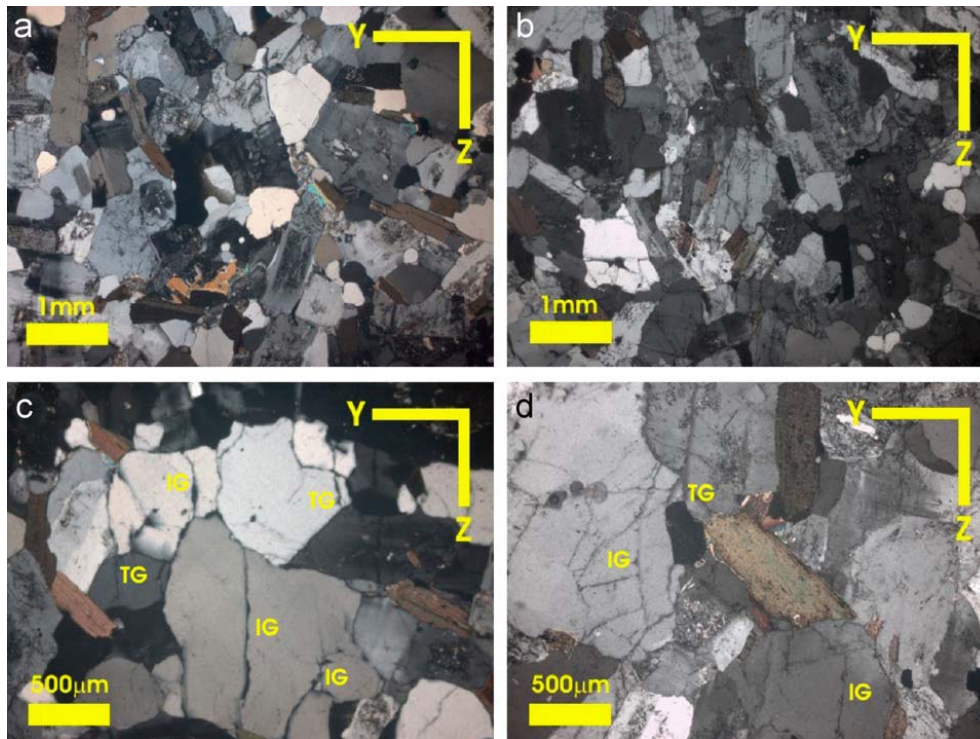


Figure 3-8. Photomicrographs of Westerly granite under cross-polarized light. (a) undeformed sample. (b) deformed sample. (c) and (d) magnified photomicrographs of deformed sample showing large intragranular and transgranular microcracks in grains of quartz. Thin sections were taken along the YZ plane (parallel to loading direction). IG—intragranular microcrack; TG—transgranular microcrack (after Heap and Faulkner, 2008).

Microphysical modeling of cracked rocks under stress can provide key insights into the development of their elastic properties. Walsh (1965c; 1965b) modeled the changes in static elastic properties as a function of crack density during uniaxial compression of rocks. The model assumes an isotropic material that contains randomly oriented cracks and predicts that the Young's modulus and Poisson's ratio decrease with the opening of cracks (equivalent to the 'crack closure' stage in Figure 3-3d). When cracks are closed under compressive stress, the sample will reach 'intrinsic' values of the elastic properties. At higher compressive stresses, frictional sliding on opposing crack faces is predicted to increase Young's modulus and Poisson's ratio above the intrinsic value. Qualitatively, this agrees with our results (Figures 3-5 and 3-7), apart from the

changes observed in the static Poisson's ratio with increasing stress (Figure 3-7a). However, we are considering the *unloading* part of the loading cycle, and in the sliding crack model, the change in radial strain with decreasing stress will be low compared to the change in axial strain with stress, due to previous sliding on cracks. This will result in a low static Poisson's ratio at high stress until stress levels drop below that at which elastic unloading can occur by sliding on cracks, whereupon the static Poisson's ratio should increase, as is seen in our data. Although sliding of cracks could equally contribute to an increase in both the axial and radial strain, the opening of the newly initiated cracks and 'crack growth' will produce more radial strain.

Walsh's models (1965c and a) and subsequent models that extend Walsh's results (e.g. Budiansky and O'Connell, 1976; Hudson, 1981; Hudson, 1990; Kachanov, 1994; O'Connell and Budiansky, 1974) predict that as crack density increases, the Young's modulus will decrease and Poisson's ratio will increase. Equation 3-8 (from Walsh 1965c) shows how the Poisson's ratio and Young's modulus would change (keeping one of the elastic properties constant at an instant) if the crack density increases (either by increasing N or c , or both).

$$\frac{\nu_f}{E_f} = \frac{\nu}{E} + \frac{2\pi N c^3}{15VE} \left[\frac{2+3\mu^2+2\mu^4}{(1+\mu^2)^{3/2}} - 2\mu \right] \quad \text{Equation 3-8}$$

where ν and ν_f are the intrinsic and effective Poisson's ratio respectively, E and E_f is the intrinsic and effective Young's modulus respectively, N is the number of cracks, c is half the crack length, V is the volume, and μ is coefficient of friction between the crack faces. If all else is kept constant, then an increase in crack density will result in higher ν_f and lower E_f . Consideration of Walsh's models can also help to interpret the difference between the static and dynamic elastic properties which are discussed in the next section.

3.5.1 Differences between static and dynamic elastic properties

The relationships between static and dynamic elastic properties have been studied by, amongst other researchers (King, 1983; Mockovčiaková and Pandula, 2003; Vanheerden, 1987; Wang, 2000), where the relationships are derived from uniaxial experiments on a range of rock types with different elastic properties. The relationships between static and dynamic Young's moduli are summarized in figure 3-9 which shows large discrepancies between the relationships. Investigations of the dynamic Poisson's ratio are rare due to the difficulties in determining the shear wave velocity (related to the picking of the S wave arrival). Consequently, very limited data relating the static and dynamic Poisson's ratios have been published. The relationship presented in this paper is derived from only one rock type and takes into account the effects of stress and microcrack damage. The differences between static and dynamic elastic properties are likely caused by factors such as microcracks, rate of loading (frequency) and strain amplitude. These factors are now discussed.

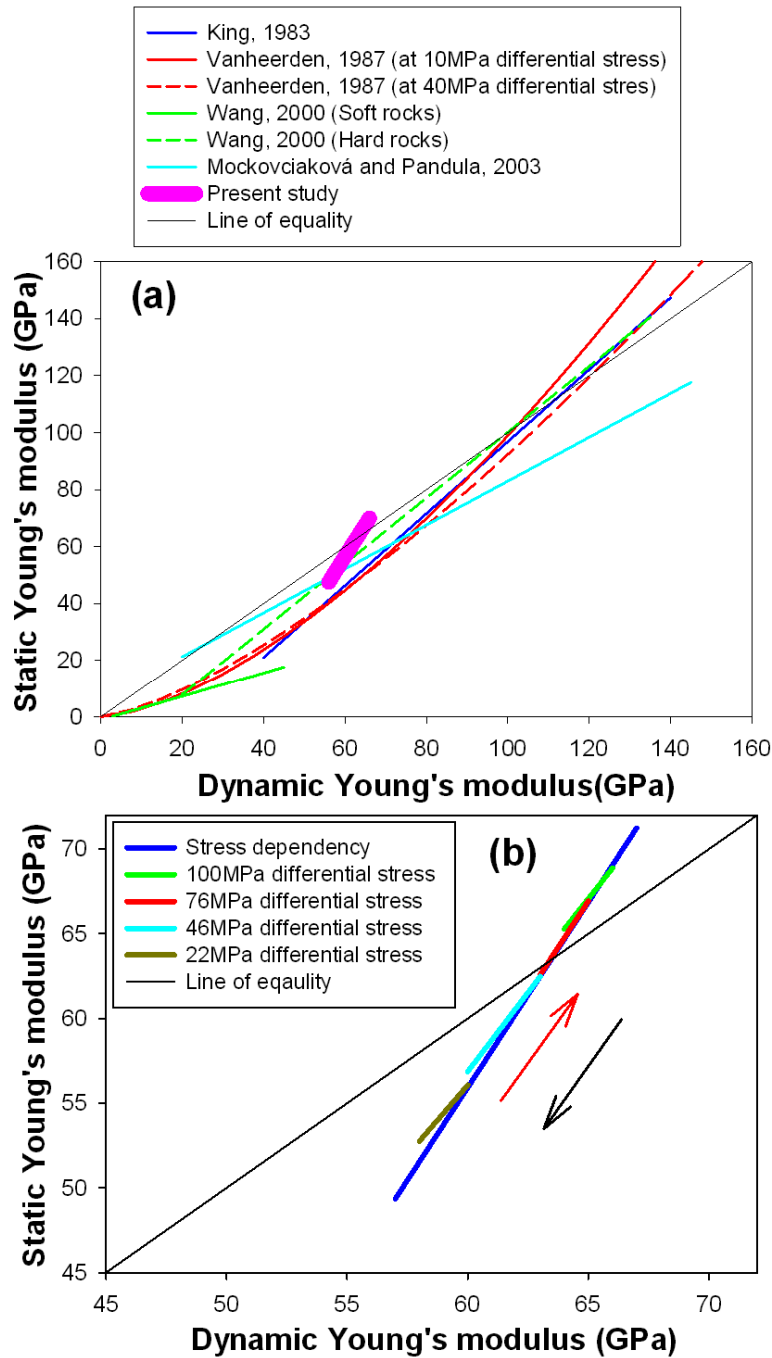


Figure 3-9. (a) Summary of the relationship between static and dynamic Young's modulus from the literature and present study. (b) Change in the present study's static vs. dynamic Young's modulus due to stress dependency and microcrack damage. The red arrow indicates the direction of change due to increasing differential stress and the black arrow indicates the direction of change due to increasing microcrack damage (from cycle 1 to cycle 5).

3.5.1.1 Microcracks

The dynamic elastic properties are calculated from wave propagation that interacts with microcracks only within the propagating path, while the static elastic properties are influenced by all of the microcracks within the sample. At low differential stress, the microcracks have a greater effect on the static Young's modulus than the dynamic Young's modulus causing the static Young's modulus to be less than the dynamic Young's modulus. However, the static Young's modulus is greater than the dynamic Young's modulus at high differential stress. A possible explanation for this scenario is that microcracks that are not orientated perpendicular and oblique to the unloading direction remain opened and the effect of these microcracks significantly affects the dynamic Young's modulus as the propagation of the S wave interacts with these cracks.

In the case of the Poisson's ratio, the opening and sliding (such as that occurring in Walsh's sliding crack model (1965c)) of the microcracks affect the static Poisson's ratio whereas only the opening of cracks affects the dynamic Poisson's ratio. When the crack density is low and the sample stiffness is high (cycle 1), the change in axial strain is larger than the change in radial strain during unloading of sample as the sliding of microcracks slightly contribute to the change in radial strain. As the sample gets weaker and the crack density increases, the sliding of microcracks affects the radial strain dominantly relative to the axial strain which cause the static Poisson's ratio to be low at high differential stress and then increase as unloading occurs.

3.5.1.2 Frequency, strain amplitude and strain rate

The static elastic properties can be considered to be measured quasi-statically; whereas the dynamic measurements were acquired at a much higher frequency, 1.5MHz. Adelinet et al. (2010) measured bulk modulus at high frequency (10^6 Hz) and low frequency (10^{-2} Hz) as a function of effective pressure, up to 200MPa; and found that with increasing effective pressure, high frequency and low frequency bulk moduli increased respectively by approximately 55% and

60% and the high frequency bulk moduli are greater than the low frequency bulk moduli (as shown in Figure 3-10). In general, elastic properties measured at high frequency are always greater than elastic properties measure at low frequency (Adam and Batzle, 2008; Batzle et al., 2006; Batzle et al., 2001).

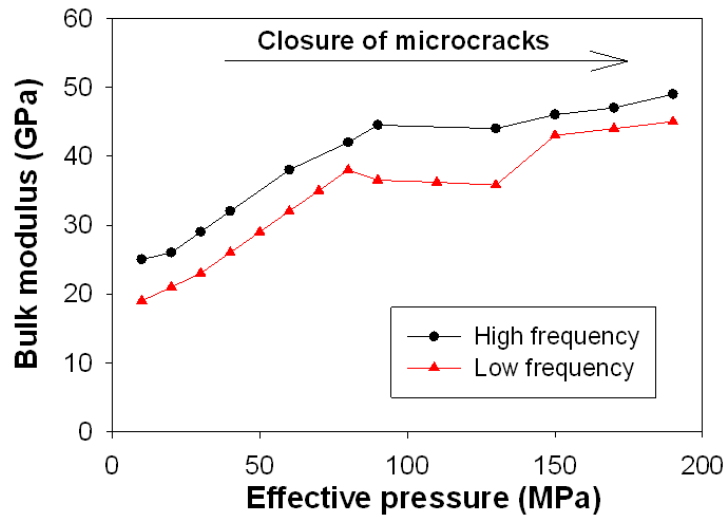


Figure 3-10. Bulk modulus obtained from high frequency velocities inversion and low frequency oscillation tests (after Adelinet et al., 2010). Effective pressure = confining pressure – pore pressure. The pore pressure is fixed to 10 MPa.

Static elastic properties are determined by increasing stress in steps which is accompanied by large strain amplitudes, generally of the order $>10^{-2}$; whereas dynamic elastic properties are determined by wave propagation with extremely small strain amplitude, generally of the order $<10^{-6}$. The high strain rate imparted by the dynamic elastic properties method is likely to result in the apparently higher stiffness as compared to the static elastic properties method as rock parameters are strain rate dependent (a higher strain rate yields a higher rock's strength). This effect is likely to reduce with higher confinement due to closure of microcracks. The strain amplitude is of key importance, as large strain amplitudes will promote sliding along cracks, whereas cracks will be unaffected by small strain amplitudes.

3.5.1.3 Bulging of the sample

A further experiment was carried out to investigate the poor correlation between the static and dynamic Poisson's ratio. As the static measurement depends heavily on the radial strain measurement, we wanted to test the hypothesis that the radial strain measurement might be affected by the friction at the loading platen/sample interface, leading to an excess radial strain measurement, resulting in large changes in the measured static Poisson's ratio. The excess radial strain is very high for short samples (that has length to diameter ratio of 1). With a longer specimen, length to diameter ratio of 2.5, the profile of lateral deformation is likely to show approximately uniform deformation along the centre of the specimen (Hawkes and Mellor, 1970). If a very long sample was used, then end effects should become even less significant in the centre of the sample. Hence, an increasing stress cycle experiment was carried out on a Westerly granite sample of 20mm diameter and 105mm length, using the methodology outlined earlier. Three sets of radial strain gauges and a set of axial strain gauges, wired in a Wheatstone configuration, were attached onto the sample (see Figure 3-11). The results of this experiment, shown in figure 3-12, showed that the radial strain increased toward the centre of the specimen. The bulging of the sample is mainly due to the friction at the sample/loading platen interface due to the mismatch of Young's moduli between the sample and platens. The Poisson's ratio is highest at the middle position and lowest at 13mm position. The dynamic Poisson's ratio is not affected by the sample's length and bulging. A comparison of the static and dynamic Poisson's ratio at each position is shown in figure 3-13. As the static Poisson's ratio is lowest at the 13mm position, the dynamic Poisson's ratio is higher than the static Poisson's ratio, with the exception of the 5th cycle. At the 26mm and middle position, the difference between the static and dynamic Poisson's ratio are similar to those outlined earlier confirming that sample bulging cannot be responsible for the observed differences in the static and dynamic Poisson's ratios. This corroborates the generally held view that samples with a length greater than twice the diameter develop representative stress and strain in the central region of the sample, away from the loading platens (Hawkes and Mellor, 1970; Paterson and Wong, 2005).

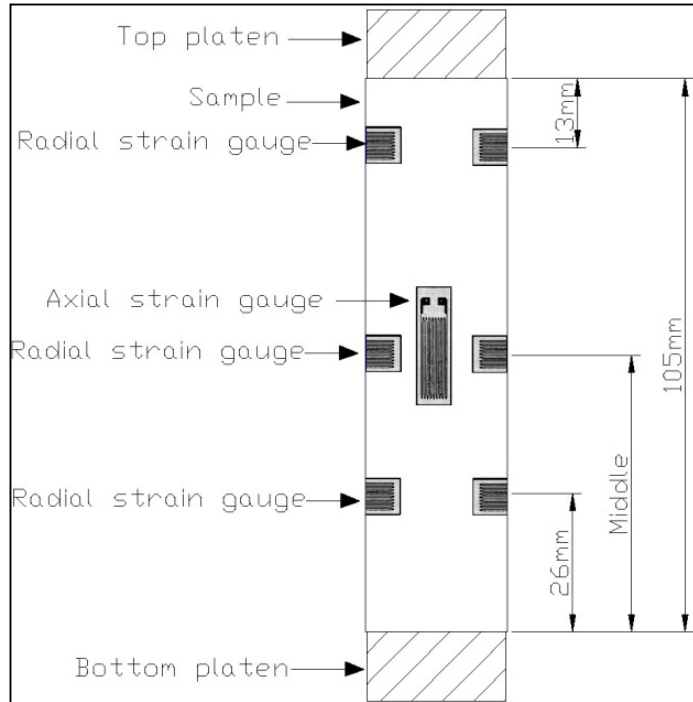


Figure 3-11. Strain gauge position on long sample

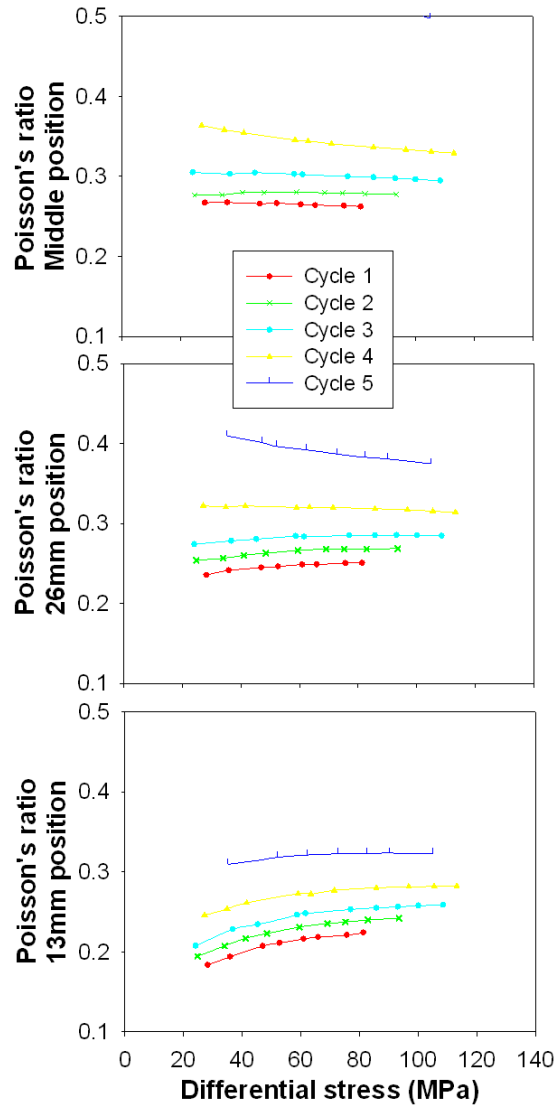


Figure 3-12. Static Poisson's ratio as a function of differential stress at different locations on the long sample.

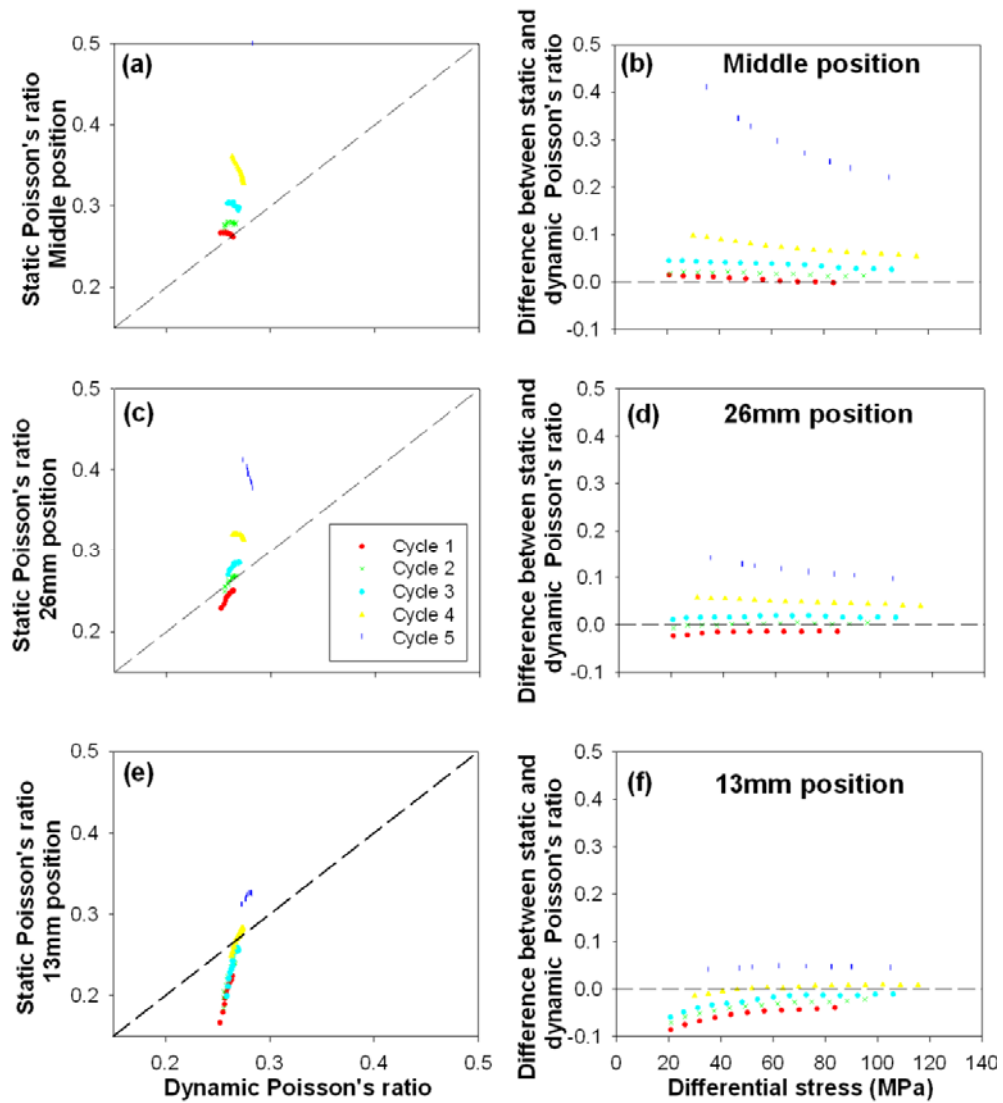


Figure 3-13. Static vs dynamic Poisson's ratio at different locations on the long sample. The dash line represents line of equality.

3.6 Conclusion

Stress-dependency due to opening of cracks oriented transverse and oblique to the axial loading direction was seen for both dynamic and static elastic properties as the crystalline rock approached failure. This resulted in: (1) a decrease in static and dynamic Young's moduli, and dynamic Poisson's ratio; and (2) an increase in the static Poisson's ratio.

Our data show that changes in the dynamic and static elastic properties occur as the rock sample accumulates microcrack damage. If the elastic properties for different stress cycles (and hence varying amounts of crack damage) at a common stress level are compared, there is a decrease in static and dynamic Young's moduli, and an increase in static and dynamic Poisson's ratios. The increase in the static Poisson's ratio is very large compared to the increase in the dynamic Poisson's ratio.

The differences between static and dynamic elastic properties are likely caused by factors such as microcracks, rate of loading (frequency) and strain amplitude. The opening and sliding of the microcracks affects the static Poisson's ratio whereas only the opening of cracks affects the dynamic Poisson's ratio as large strain amplitudes will promote sliding along cracks, whereas cracks will be unaffected by small strain amplitudes. The effects of stress and crack damage are likely the cause of the large discrepancies between the relationships between the static and dynamic Young's moduli reported in the literature.

4 Quantifying the effect of varying damage history in crystalline rocks on the P and S wave velocities and elastic properties under hydrostatic confining pressure.

4.1 Abstract

Cracks play a very important role in many geotechnical issues and in a number of processes in the earth's crust. Seismic waves can be used as a remote sensing tool for determining crack density. The effect of varying crack density on the P and S wave velocities and elastic properties under confining pressure were quantified. The evolution of P and S wave velocities were monitored as a suite of dry Westerly granite samples were taken to 60%, 70%, 80% and 90% of the unconfined uniaxial strength of the sample. The induced microcrack damage samples were then subjected to hydrostatic confining pressure up to 200MPa to quantify the effect of varying crack density on the P and S wave velocities and elastic properties under confining pressure.

Strong stress-dependency of P and S wave velocities, V_p/V_s , Young's modulus and Poisson's ratio exist in the uniaxial compressive and hydrostatic confining conditions due to closure of microcracks. The opening and propagation of microcracks predominantly parallel to the loading direction caused the S wave to decrease dramatically while the P wave decreased at a near constant rate. This resulted in a rapid decrease in the Young's modulus and a rapid increase in the V_p/V_s and Poisson's ratio. The results show that anomalously high Poisson's ratio and V_p/V_s and low Young's modulus can serve as a sensitive indicator of the amount of crack damage in the upper crust.

The elastic wave velocities and Young's modulus of samples that have a greater amount of microcrack damage required higher confining pressure to be equal to those of samples with no induced microcrack damage. The crack closure pressure for the Westerly granite samples is about 130MPa and is independent of the amount of microcrack damage induced into the samples.

4.2 Introduction

Cracks are one of the most important physical properties of rocks, as they affect rock quality by reducing the strength and increasing the permeability of the rock, providing routes for the passage of fluids and gas. For that reason, they play an essential role in many geomechanical issues (stability of boreholes, stimulation of oil and geothermal reservoirs, the design of civil structures, tunnels and hazardous waste disposals), and in understanding a number of processes in the Earth's crust such as magmatic intrusions, plate tectonics, fault mechanics and sedimentary basins.

More accurate interpretations of seismic reflection and refraction records require a better understanding of the effects of cracks on P and S waves. Birch (1960), and Kern (1978; Kern, 1990) found that the P wave velocities of various rock samples increase rapidly in a nonlinear manner below a critical point, referred to as the crack-closing pressure, as the confining pressure increases. They also found that there is a linear dependence of P wave velocities on confining pressure above the crack closing pressure (Figure 4-1). Below this pressure, microcrack closure is responsible for the non linear rapid increase of the velocities and above this pressure, the intrinsic properties (elastic compaction of a crack-free rock) are observed.

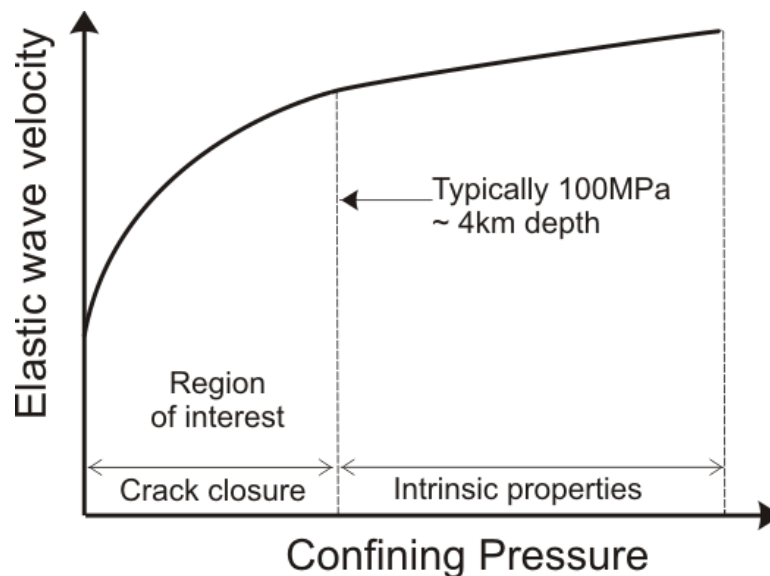
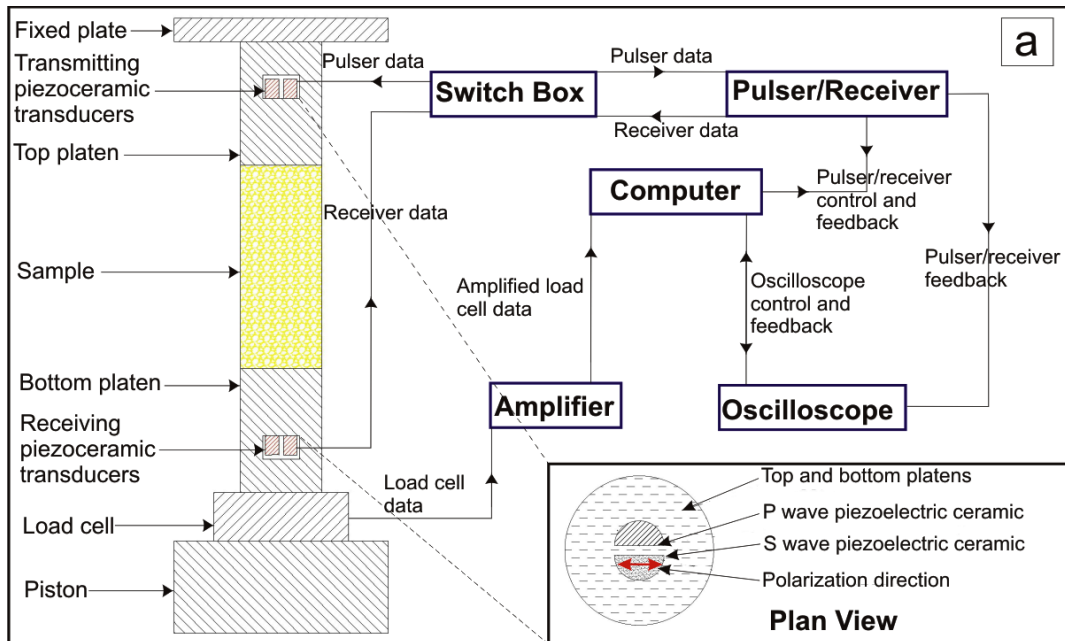


Figure 4-1. Schematic diagram showing the effect of confining pressure on elastic wave velocity.

Many researchers measured the P and S wave velocities of different rock samples that contain unknown amount of microcracks and different microstructure, as a function of confining pressure (Benson et al., 2005; Benson et al., 2006a; Benson et al., 2006b; Birch, 1960; Birch, 1961; Christensen, 1965; Christensen, 1974; Christensen and Wang, 1985; Kern, 1978; Kern, 1990; Kitamura et al., 2010; Nur and Simmons, 1969; Peacock et al., 1994; Schubnel et al., 2006; Simmons, 1964; Wang and Ji, 2009). However, there is not much information about the effect of confining pressure on the P and S wave velocities of rocks that contain a controlled amount of microcrack damage. The aim of this study is to quantify the effect of varying crack density on the P and S wave velocities and elastic properties under confining pressure. The evolution of P and S wave velocities were monitored as a suite of dry Westerly granite samples were taken to 60%, 70%, 80% and 90% of the unconfined uniaxial stress. The induced microcrack damage samples were then subjected to hydrostatic confining pressure up to 200MPa and the evolution of P and S wave velocities were also monitored. The methodology used during the experiments is first presented, and then the results obtained are shown. Possible explanations for the trends observed in the data are discussed.

4.3 Experimental Methodology



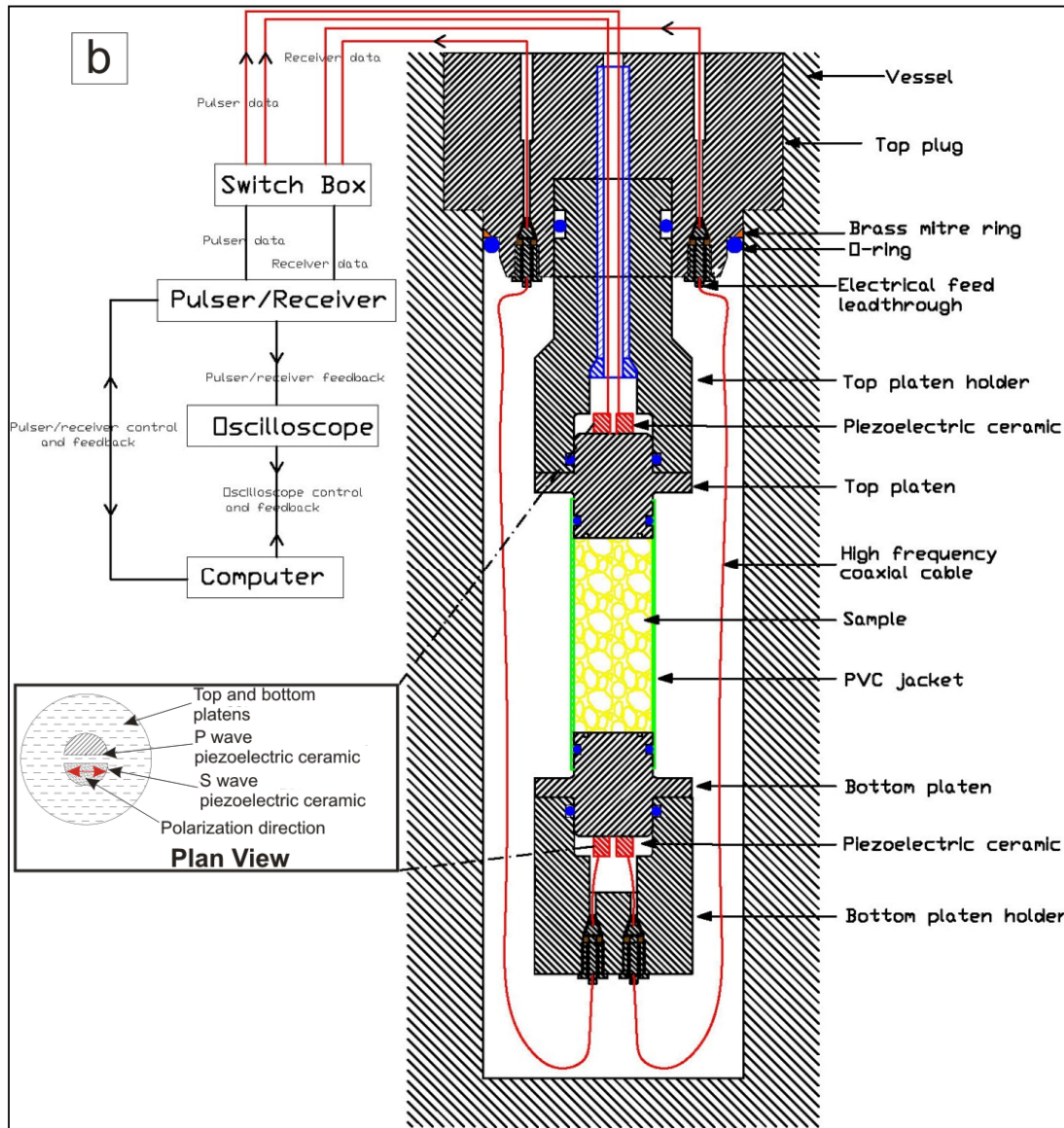


Figure 4-2. Schematic diagram of the uniaxial (a) and hydrostatic (b) experimental setup

A standard uniaxial press, where the sample is compressed unconfined ($\sigma_2 = \sigma_3 = 0$) between a fixed rigid plate and a manually controlled moving hydraulic piston, was used to induce microcrack damage into Westerly granite samples (Figure 4-2a). P and S wave piezoelectric ceramics that have a fundamental frequency of 1.5MHz are housed in the loading platens to measure P and S wave velocities simultaneously as axial load is applied to the samples. Chapter 3 gives full details of the uniaxial apparatus setup. The unconfined strength (UCS) of the samples was taken to be 221MPa differential stress (Table

1). Sample WGUH1, WGUH2, WGUH3, and WGUH4 were taken to 60% $\pm 5.0\%$, 70% $\pm 5.8\%$, 80% $\pm 6.6\%$, and 90% $\pm 7.5\%$ respectively of the UCS. The loading and unloading rates were kept at $\sim 1\text{MPa}/\text{min}$. The load was held constant at every $\sim 6\text{MPa}$ for a period of ~ 10 seconds to record the P and S wave data.

The microcrack induced samples were then placed in a hydrostatic apparatus, (*See Armitage, 2008 for details of the hydrostatic apparatus*) (Figure 4-2b), to investigate the effect of confining pressure (depth) on the P and S wave velocities in variably controlled fractured rocks. The hydrostatic rig is capable of performing experiments at confining pressures up to 200MPa. A PVC jacket was used to separate the samples from the confining low viscosity (10 cs) silicon oil. The pore pressure within the samples was vented to laboratory conditions. The pressurization and depressurization rate were kept at $\sim 1\text{MPa}/\text{min}$ and the confining pressure was held constant at every 10MPa for a period of ~ 10 seconds to record the P and S wave data. Electrical lead-throughs are placed in the top plug and bottom platen holder to feed the high frequency coaxial cables. PEEK material is used to seal and insulate the electrical lead-throughs from the body of the top plug and bottom platen holder. Two different types of piezoelectric ceramics, one P wave and one S wave with fundamental frequency of 1.5MHz, are glued to the upper and lower platens. The schematic arrangement is shown in the Figure 4-2b. The piezoelectric ceramics are separated from the confining pressure by the use of the top and bottom platen holder. The pulsing P and S wave piezoelectric ceramic is aligned with the receiving P and S wave piezoelectric ceramic respectively, and both S wave crystals were polarized in the same direction. Through transmission method was employed to measure simultaneously the P and S wave velocity of the sample. Sintered stainless steel, 0.125" thick with 0.5 micron nominal pore size, was used as a backing material on the piezoelectric ceramic (VanValkenburg, 1983). The elastic wave impedance of the backing matched the elastic wave impedance of the piezoelectric ceramic resulting in a heavily damped piezoelectric ceramic with wider bandwidth that displays good range resolution. The standard for using ultrasonic testing to determine pulse velocities (ASTM, 1997a) was adhered to for accurate and reliable measurement of P and S wave velocity (see figure 4-3 for a representative example of P and S wave arrival collected on sample WG1

for this study). A negative spike pulser / receiver (JSR DPR300 Pulser / Receiver) was used for excitation of the piezoelectric ceramics and detection of the pulse. The choice of piezoelectric ceramics to excite or receive is manually controlled by a switch box. A 300MHz bandwidth digital oscilloscope with 20ppm time based accuracy (Tektronix TDS 3032B) is employed for recording and display of the received pulse which is synchronized with the pulser/receiver. The oscilloscope was also used to average 512 signals to reduce noise. The pulser/receiver and oscilloscope are coupled to a computer for storage of data, and processing of the recorded waveforms for analysis.

All measurements were made on oven dry (at 80°C) intact Westerly granite samples under ambient laboratory conditions, with temperatures approximately 20°C. Westerly granite from south-east Rhode Island, USA, has low initial crack density, small grain size (average 1mm), has an extensive history of laboratory testing, can provide a high level of repeatability under carefully controlled test conditions, and generally considered to be isotropic [Lockner, 1998; Haimson and Chang, 2000]. For viable data set, the samples were cored, 20mm diameter, from the same block, in the same orientation to allow results to be comparable, cut so their length-to-diameter ratios were in excess of 2.5 but less than 3 and precision-ground to strict tolerances (± 0.02 mm) as to the squareness of their ends (Paterson and Wong, 2005).

From the P and S wave velocities, elastic constants such as Young's modulus, E , and Poisson's ratio can be estimated from the well-known relationships of isotropic materials as follows (e.g. Kuttruff, 1991):

$$E = \frac{\rho V_s^2 (3V_p^2 - 4V_s^2)}{V_p^2 - V_s^2} \quad \text{Equation 4-1}$$

$$\nu = \frac{V_p^2 - 2V_s^2}{2(V_p^2 - V_s^2)} \quad \text{Equation 4-2}$$

where V_p is the P wave velocity, V_s is the S wave velocity and ρ is the density. Density changes during the experiments were considered to have a negligible effect on the P and S wave velocities. In fact, density and length changes for Westerly granite samples loaded up to its failure strength under uniaxial

compression were found to account for less than 0.08% of the Young's modulus. The length changes only accounted for less than 0.003%. This is due to the fact that Westerly granite has a total porosity of less than 1% (Brace, 1965; Meredith and Atkinson, 1985; Nur and Simmons, 1969; Walsh and Brace, 1972).

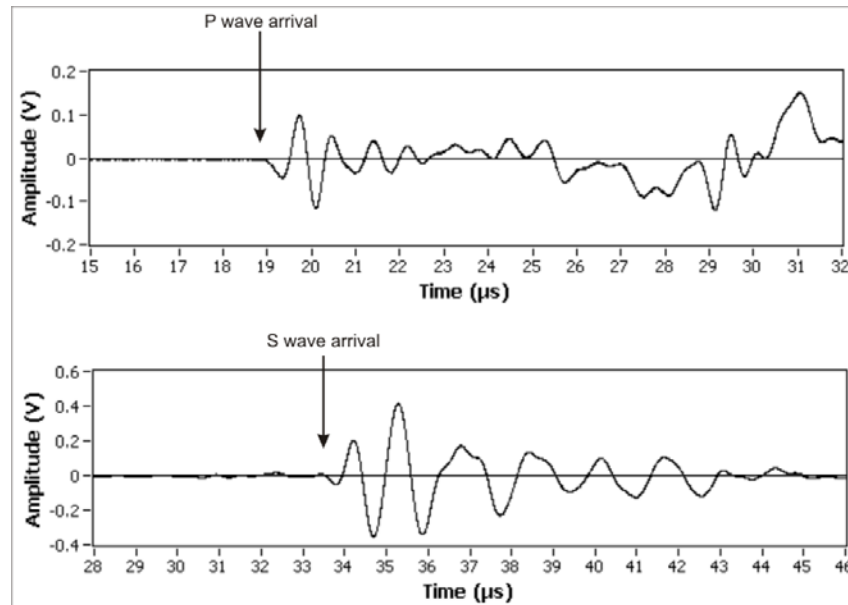


Figure 4-3. Typical P and S wave arrivals (from sample WGA). Top: Pulsing with P wave piezoelectric ceramic and receiving with P piezoelectric ceramic trace. Bottom: Pulsing with S piezoelectric ceramic and receiving with S piezoelectric ceramic trace. Excitation pulse is at 0 μ s.

Sample	Experiment type	Failure Stress (MPa)	Note
WG-SDC	UCS	205.86	To determine UCS
WG-SDB	UCS	217.88	To determine UCS
WG-SDG	UCS	223.81	To determine UCS
WG-SDE	UCS	239.34	To determine UCS
WGA	Hydrostatic	NA	No induced microcrack damage
WGB	Hydrostatic	NA	No induced microcrack damage
WGD	Hydrostatic	NA	No induced microcrack damage
WGUH1	Uniaxial and Hydrostatic	NA	Loaded to 60% \pm 5.0% of UCS
WGUH2	Uniaxial and Hydrostatic	NA	Loaded to 70% \pm 5.8% of UCS
WGUH3	Uniaxial and Hydrostatic	NA	Loaded to 80% \pm 6.6% of UCS
WGUH4	Uniaxial and Hydrostatic	NA	Loaded to 90% \pm 7.5% of UCS

Table 4-1. Summary of experiments.

4.4 Results

4.4.1 Uniaxial Compressive condition

Increasing the differential stress during the uniaxial compressive condition closes the initial microcracks present in the sample. This resulted in strong stress-dependency for the elastic wave velocities, their ratio (V_p/V_s), Young's modulus and Poisson's ratio (Figure 4-4). If sample WGUH2 is considered, there was an increase in the P (5.2 km/s to 5.7 km/s) and S wave velocities (3km/s to 3.2 km/s), V_p/V_s (1.74 to 1.78), Young's modulus (60GPa to 68GPa) and Poisson's ratio (0.25 to 0.27) as the differential stress increased from 12MPa to 155MPa. As sample WGUH4 approached failure, the S wave velocity decreased by 2% from 148MPa to 184MPa differential stress and then decreased rapidly by 4% to 200MPa differential stress. The P wave velocity decreased by 0.5% at a near constant rate from 148MPa to 200MPa differential stress. This resulted in a decrease in the Young's modulus (9%) and increase in the Poisson's ratio (13%) and V_p/V_s (6%) from 148MPa to 200MPa differential stress.

The samples accumulate microcrack damage when they exceed the perfectly elastic deformation region (about a 1/3 to 2/3 of the UCS (Bieniawski, 1967a; Brace et al., 1966)), which is seen in the unloading curves (Figure 4-4). At a constant stress level (66MPa differential stress in this example), the microcrack damage caused an overall decrease in the P (3%) and S wave (10%) velocities and Young's modulus (16%) and an overall increase in the Poisson's ratio (17%) and V_p/V_s (7%) (Figure 4-5).

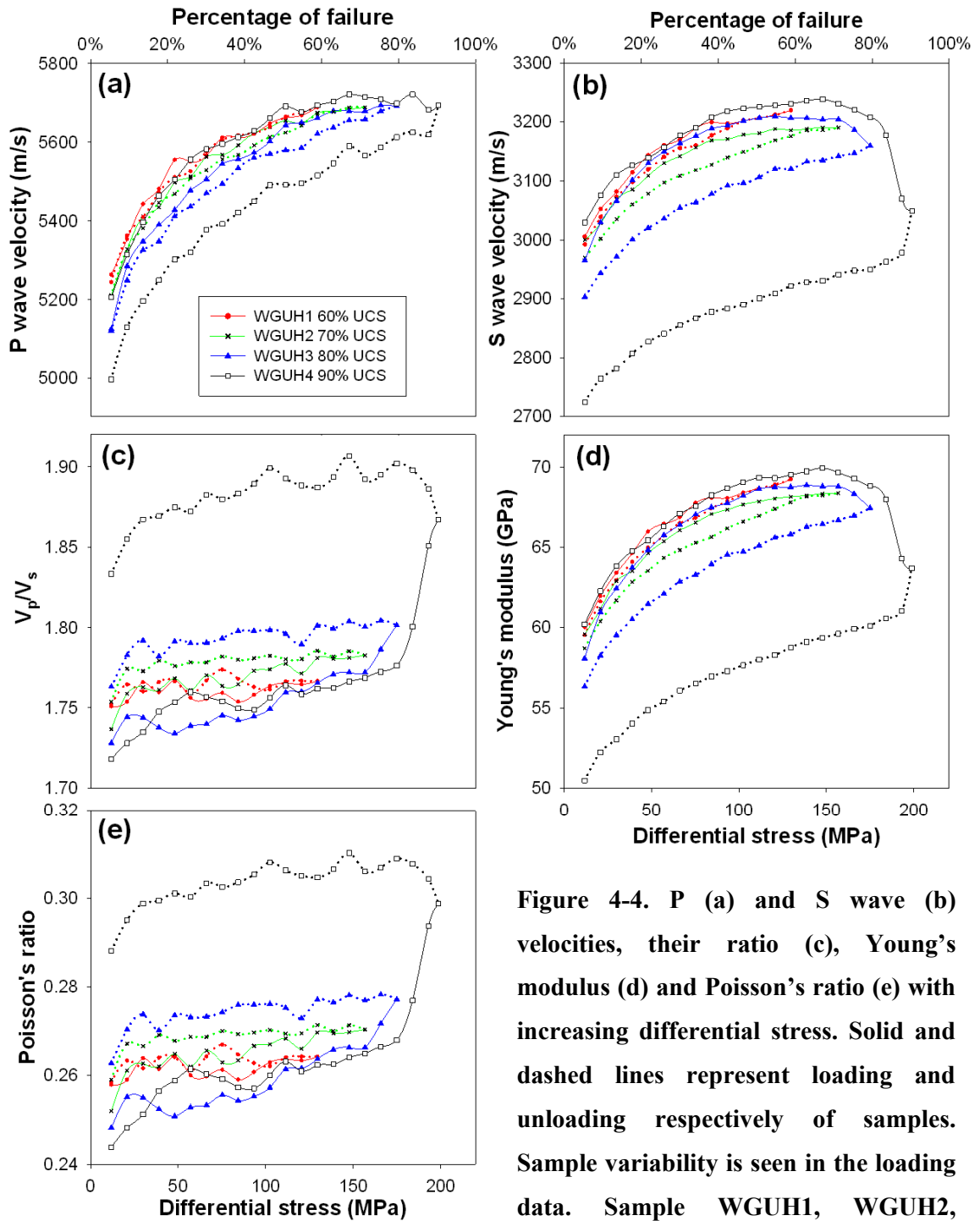


Figure 4-4. P (a) and S wave (b) velocities, their ratio (c), Young's modulus (d) and Poisson's ratio (e) with increasing differential stress. Solid and dashed lines represent loading and unloading respectively of samples. Sample variability is seen in the loading data. Sample WGUH1, WGUH2, WGUH3, and WGUH4 was taken to 60%, 70%, 80% and 90% respectively of the UCS.

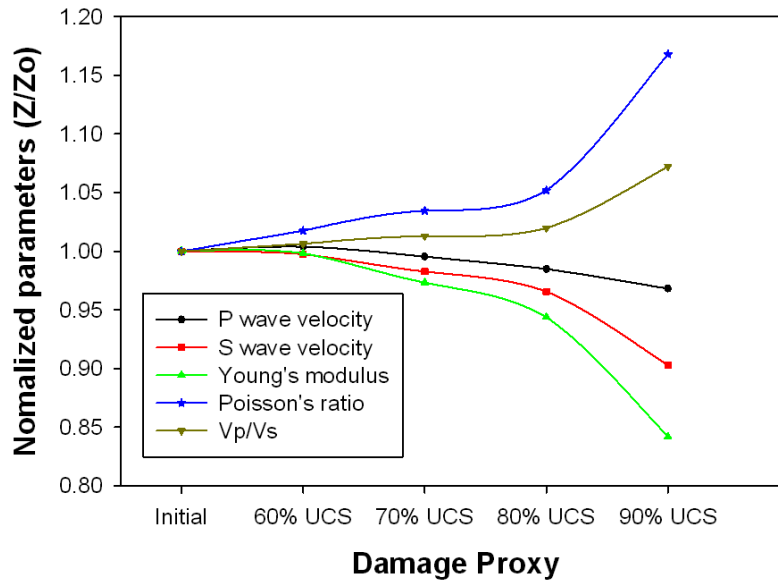


Figure 4-5. Summary of results showing normalized parameters as a function of microcrack damage. Z is the P or S wave velocity, V_p/V_s , Young's modulus, or Poisson's ratio at a given damage level. Z_o is the P or S wave velocity, V_p/V_s , Young's modulus, Poisson's ratio at an initial damage level. The initial damage is the microcrack present in the sample before any other microcracks were induced. These parameters were taken at 66MPa differential stress during uniaxial compression.

4.4.2 Hydrostatic confining condition

During hydrostatic pressurization, the microcracks within the samples that have no induced microcrack damage (WGA, WGB, and WGD) are closed resulting in a rapid non-linear increase in the P and S wave velocities and Young modulus (Figure 4-6 a and c), up to about 130MPa, and then a gentle linear increase up to 200MPa. The elastic wave velocities are higher than those measured during the uniaxial compressive condition. The P wave velocity increased from 5.1km/s to 6km/s, S wave velocity increased from 3km/s to 3.5km/s and the Young's modulus increased from 60GPa to 80GPa. The V_p/V_s and Poisson's ratio increased rapidly from 1.668 to 1.707 and 0.219 to 0.237 respectively, as the confining pressure increased to 10MPa, and then increased slightly to 1.714 and 0.242 respectively as the confining pressure increased to 120MPa. Above 120MPa confining pressure, the V_p/V_s and Poisson's ratio are

fairly constant. The induced microcrack damage within the samples (WGUH1, WGUH2, WGUH3, and WGUH4) is also closed as the confining pressure increases. The elastic wave velocities and Young's modulus of samples that have a greater amount of microcrack damage required higher confining pressure to be equal to those of samples with no induced microcrack damage. The P and S wave velocities of samples with high microcrack damage (WGUH3 and WGUH4) are equal to those of the samples with no induced microcrack damage at 120MPa and 60MPa respectively. There is not much difference between the V_p/V_s and Poisson's ratio of samples with and without induced microcrack damage (Figure 4-6 g and h). During depressurization, the elastic wave velocities, V_p/V_s , Young's modulus, and Poisson's ratio increased slightly compared to those during pressurization.

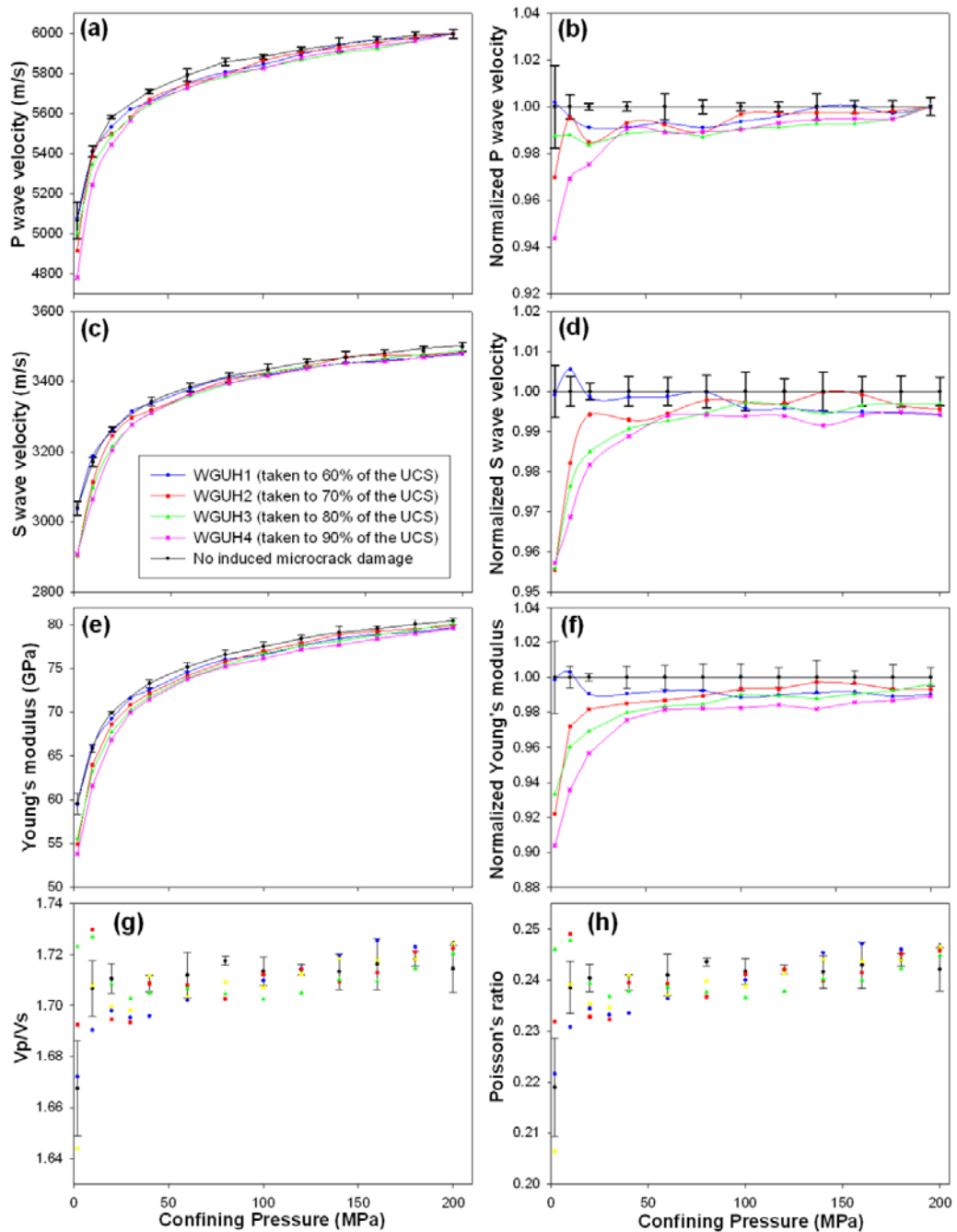


Figure 4-6. P (a) and S wave (c) velocity, their ratio (g), Young's modulus (e) and Poisson's ratio (h) with increasing confining pressure. Errors in velocity are estimated from repetition of measurements from samples without induced microcrack damage (WGA, WGB, and WGD). The P and S wave velocities and Young's modulus of the samples with induced microcrack damage are normalized to the P and S wave velocities and Young's modulus of the samples without microcrack damage (b, d, and f).

4.5 Discussion

4.5.1 The effect of P and S wave velocities and elastic properties subjected to uniaxial compressive condition

There are several stages in the brittle failure of rocks: crack closure, elastic deformation, stable crack propagation, and unstable crack propagation (Bieniawski, 1967a; Bieniawski, 1967b; Bieniawski, 1967c; Brace et al., 1966) (Figure 4-9). Crack closure takes place, as soon as the rock is stressed, in cracks oriented perpendicular and oblique to the applied compressive stress. In the case of uniaxial compression, the compressive stress is clearly in uniaxial loading direction. This caused the P and S wave velocities, V_p/V_s and elastic properties (Young's modulus and Poisson's ratio) to increase. However, this region is about 6% of the UCS for hard rocks (for example Westerly granite). After the crack closure region has occurred, elastic deformation takes place. The P and S wave velocities, V_p/V_s and elastic properties also increased in this stage. If the applied load is removed during this stage, the P and S wave velocities, V_p/V_s and elastic properties will follow the same path as the loading path. Bieniawski [1967a] found that the crack faces slides against each other in this stage which resulted in the formation of smaller stable vertical cracks along the length of the initial crack. Bieniawski [1967a] also found that this stage finishes at ~35% of the UCS of the sample, while Brace (1966) found this stage can end at one-third to two-third of the UCS of the sample. In the stable crack propagation stage, the cracks propagate predominantly in the direction of the applied stress and cause the rock to become dilatant. The rate of increase of the P and S wave velocities decreased and the velocities tend to a constant value (see sample WGUH2 in Figure 4-4). This stage ends at ~80% of the UCS of the sample (Bieniawski, 1967a). In the final stage, unstable crack propagation, the cracks continues to propagate in the direction of the applied stress at a faster rate compared to stable crack propagation, and the volumetric strain increased significantly. As the sample approaches failure, the microcracks coalesce to form shear fracture zone. This resulted in a slight decrease of the P wave velocity and a dramatic decrease of the S wave velocity (see sample WGUH4 in Figure 4-4). The S wave velocity is much more sensitive than the P wave velocity because the S wave is polarized

perpendicular to the loading direction and hence perpendicular to the cracks' orientation, meanwhile the P wave is polarized parallel to the cracks' orientation. Bieniawski [1967a] found that there is considerable damage in the rock samples through shattering of its grains.

The rock accumulates microcrack damage in the stable crack propagation and unstable crack propagation stages. The higher the applied stress in these regions, the more microcrack damage the samples accumulates. The applied stress is non-linear to microcrack damage. If the applied load is removed in these stages, the P and S wave velocities during unloading of the sample are less than those during loading at any given stress level (see unloading curves in Figure 4-4). The accumulated microcrack damage is greater in this data set compared the data set in Chapter 3 (Figure 4-7), because the loading threshold is not exactly the same. Samples taken to 60%, 70%, 80% and 90% of the UCS have a standard deviation of up to $\pm 7.5\%$ of the UCS. Any difference in the UCS threshold, especially close to failure of the sample, will result in a higher accumulation of microcrack damage.

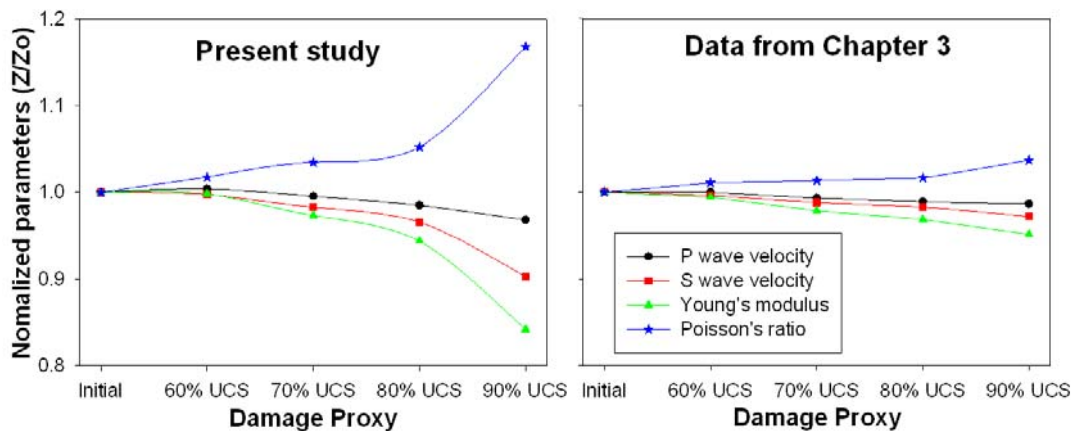


Figure 4-7. Summary of results showing normalized parameters as a function of microcrack damage for: (left) present study; and (right) data from chapter 3. Z is the P or S wave velocity, V_p/V_s , Young's modulus, or Poisson's ratio at a given damage level. Z_o is the P or S wave velocity, V_p/V_s , Young's modulus, Poisson's ratio at an initial damage level. The initial damage is the microcrack present in the sample before any other microcracks were induced. These parameters were taken at 66MPa differential stress during uniaxial compression.

4.5.2 The effect of P and S wave velocities and elastic properties subjected to hydrostatic confining condition

The microcrack and induced microcrack damage within the sample are closed when they are placed under confining pressure. There is a rapid non linear increase in the elastic wave velocities, followed by a gentle linear increase. This response of the elastic waves velocity with increasing confining pressure are similar to those observed by Birch (1960) and Kern (1978; Kern, 1990). The crack closure pressure for the Westerly granite samples is about 130MPa. Birch (1960; Birch, 1961) measured P wave velocities for some 250 rock specimens, mainly igneous and metamorphic rocks, up to 1000MPa confining pressure and found that for typical holocrystalline igneous rocks the crack closure pressure is of the order of 100MPa. Kern (1978) measured P wave velocities in granite, amphibolites, and peridotite specimens under confining pressure up to 600MPa and found that the crack closure pressure is generally in the range 100MPa–250MPa. During depressurization, the microcracks take time to reopen and therefore the P and S wave velocities increase.

4.5.3 Comparison between the effect of P and S wave velocities subjected to hydrostatic confining and uniaxial compressive condition

It is seen, from increasing-amplitude cyclic loading experiments in an uniaxial compressive condition (in Chapter 3), that the P and S wave velocities during loading follows the same path as the previous unloading cycle. However, the P and S wave velocities loading paths during hydrostatic confining condition are generally higher than those in the uniaxial compressive condition. The difference between the elastic wave velocities during the hydrostatic confining and uniaxial compressive conditions is greater for samples taken to higher percentage of the UCS (Figure 4-8). The elastic wave velocities are higher in the hydrostatic confining condition because the confining pressure closes cracks in all direction whereas the cracks are mainly closed in the direction parallel to the loading direction in the uniaxial compressive condition.

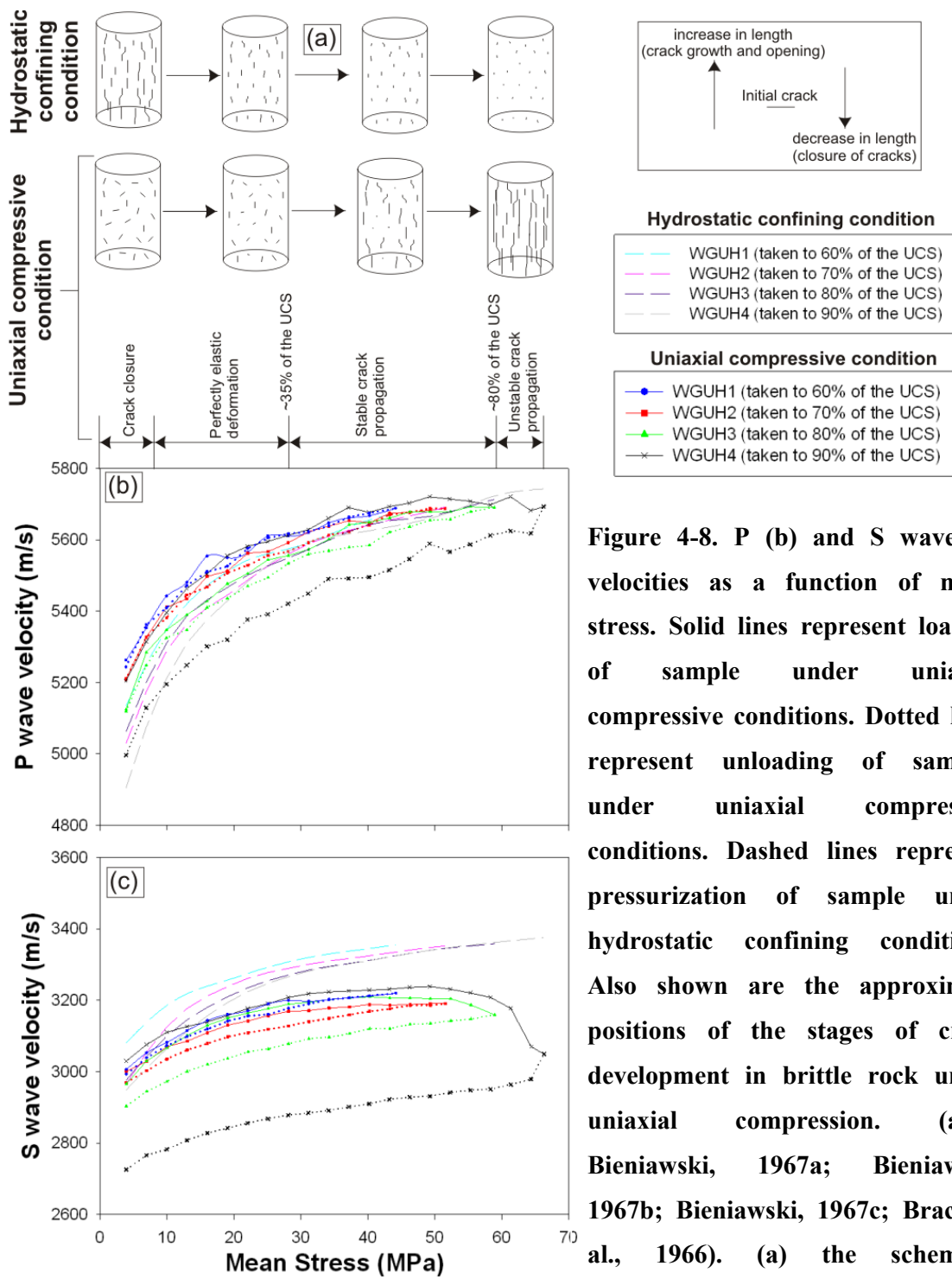


Figure 4-8. P (b) and S wave (c) velocities as a function of mean stress. Solid lines represent loading of sample under uniaxial compressive conditions. Dotted lines represent unloading of samples under uniaxial compressive conditions. Dashed lines represent pressurization of sample under hydrostatic confining conditions. Also shown are the approximate positions of the stages of crack development in brittle rock under uniaxial compression. (after Bieniawski, 1967a; Bieniawski, 1967b; Bieniawski, 1967c; Brace et al., 1966). (a) the schematic illustration of crack orientation and growth are referred to a sample that has been through all the stages involved in the brittle failure of rocks (e.g. WGUH4)

4.6 Conclusion

We presented laboratory data on the evolution of P and S wave velocities, V_p/V_s , and elastic properties (Young's modulus and Poisson's ratio) as: (1) dry Westerly granite samples were taken to 60%, 70%, 80% and 90% of the unconfined uniaxial strength and, (2) the induced microcrack damage samples were subjected to hydrostatic confining pressure up to 200MPa. Strong stress-dependency exists in the uniaxial compressive and hydrostatic confining conditions due to closure of microcracks. In the uniaxial compressive condition, the microcracks are closed mainly in the direction of the applied stress, whereas the microcracks are closed in all direction in the hydrostatic confining condition. Closure of microcracks caused an increase in the P and S wave velocities, V_p/V_s , Young's modulus and Poisson's ratio.

It is well established that changes in V_p/V_s and Poisson's ratio are usually related to changes in the fluid transport properties (Nur and Simmons, 1969; O'Connell and Budiansky, 1974), fluid pressure (Christensen and Wang, 1985), and macrofracture (Moos and Zoback, 1983). The opening and propagation of microcracks predominantly parallel to the loading direction caused the S wave to decrease dramatically while the P wave decreased at a near constant rate which resulted in a rapid decrease in the Young's modulus (from ~67GPa to 56GPa) and a rapid increase in the V_p/V_s (~1.76 to 1.88) and Poisson's ratio (0.26 to 0.30). This shows that anomalously high Poisson's ratio and V_p/V_s and low Young's modulus can also serve as a sensitive indicator of the amount of crack damage in the upper crust.

The elastic wave velocities and Young's modulus of samples that have a greater amount of microcrack damage required higher confining pressure to be equal to those of samples with no induced microcrack damage. The crack closure pressure for the Westerly granite samples is about 130MPa and is independent of the amount of microcrack damage induced into the samples.

5 Attenuation measurements of crystalline rocks under hydrostatic confining and uniaxial compressive conditions

5.1 Abstract

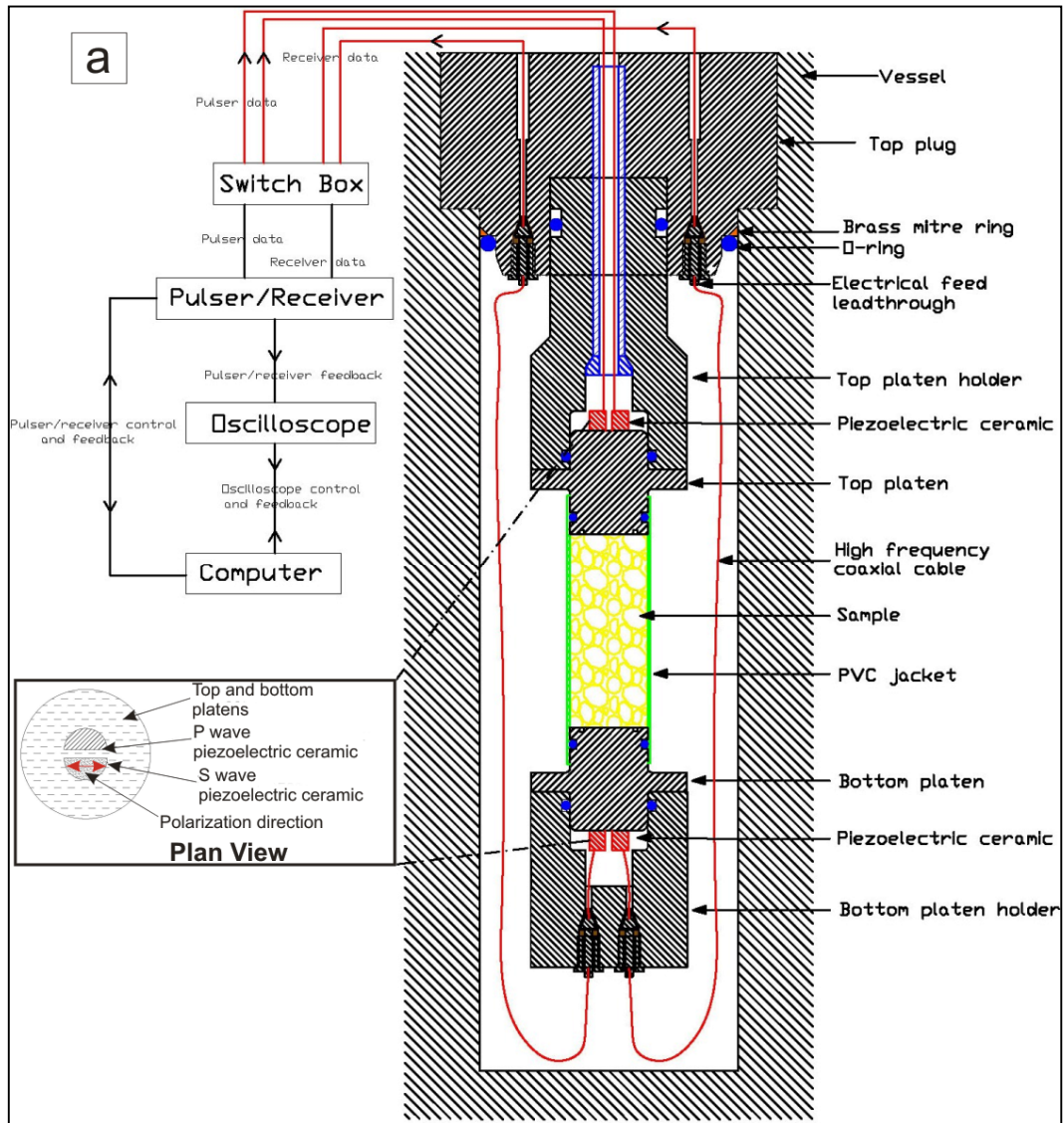
Seismic wave propagation in rocks is characterized by velocity and attenuation. The through transmission and spectral ratio techniques were used to measure P and S wave velocities and attenuation respectively of oven dried crystalline rock samples. Two suites of samples were subjected to different conditions: hydrostatic confining, up to 200MPa, and uniaxial compressive. Microcrack damage was induced in samples during increasing-amplitude cyclic loading experiments under uniaxial compressive condition. Attenuation measurements were made in the frequency range of 0.8MHz to 1.7MHz. In our experiments, frictional dissipation and scattering are the likely attenuation mechanisms. Closure of cracks due to increasing confining pressure and differential stress resulted in an increase in velocity and decrease in attenuation. Increasing-amplitude stress cycling caused an increase in the density of microcrack damage which resulted in a decrease in velocities and increase in attenuation as the number of cycles increased. Our results show that seismic wave attenuation is more sensitive to the effects of microcrack closure and microcrack damage than seismic wave velocity.

5.2 Introduction

A fundamental parameter associated with seismic wave propagation in rock is attenuation, which usually results in a change of the amplitude and shape of the transient waveform. Seismic wave attenuation consist of intrinsic attenuation (absorption of energy through conversion into heat due to interaction between the propagating wave and the rock) and extrinsic attenuation (the lost of energy due to beam spreading, transmission loss and scattering). However, it is difficult to differentiate between the two types of attenuation (O'doherty and Anstey, 1971; Schoenberger and Levin, 1978; Spencer et al., 1982).

Seismic wave velocities and attenuation are affected by the presence of cracks (Friedman and Bur, 1974; Johnston and Toksöz, 1980; Murphy III, 1984; Pyrak-Nolte et al., 1990; Tao et al., 1995; Xu and King, 1990). In dry cracks, the mechanisms responsible for attenuation are frictional dissipation and scattering (Gordon and Davis, 1968; Lockner et al., 1977; Meglis et al., 1996; Walsh, 1966; Wulff et al., 1999). The quality factor, Q , which is dimensionless, is used as a measure of attenuation. The higher the Q factor, the lesser attenuating the rock is. The range of Q factor values in crystalline rocks from laboratory and seismic experiments is scarce. Moreover, a knowledge of Q factor in crystalline rocks is important because the use of high-resolution seismic methods is becoming increasingly common in such rocks for engineering, environmental and mining purposes (Juhlin, 1995; Milkereit et al., 1994). In this paper, oven dried crystalline rocks were subjected to hydrostatic confining and uniaxial compressive conditions to close microcracks and induce microcrack damage respectively. We aim to quantify the changes in P and S wave attenuation due to frictional dissipation and scattering as the microcracks and microcrack damage varies. The spectral ratio technique was used to measure attenuation. The technique relies on the fact that signal amplitude decreases with increasing frequency more rapidly for a lossy medium than for an 'elastic' reference. Forming the ratio of spectral amplitudes for the reference and rock sample gives a measure of the relative attenuation from which the Q factor can be calculated.

5.3 Experimental methodology



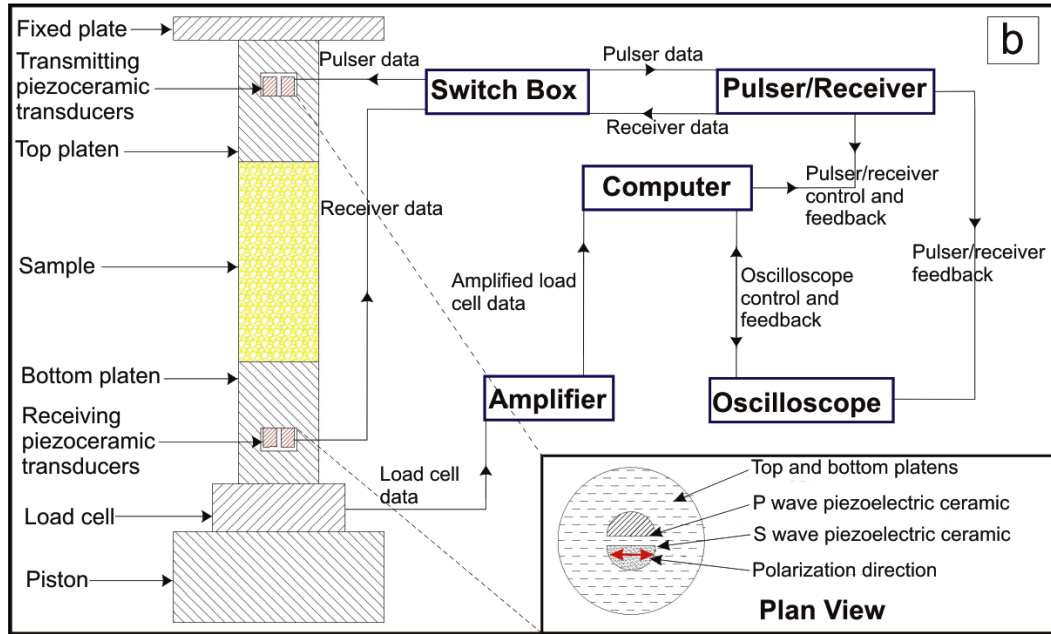


Figure 5-1. Schematic diagram of the hydrostatic (a) and uniaxial (b) experimental setup

P and S wave velocities and attenuation measurements were made as two suites of samples were subjected to different conditions: hydrostatic confining and uniaxial compressive. A hydrostatic apparatus was used to measure P and S wave velocity and attenuation of samples WGA, WGB, and WGD up to 200MPa confining pressure (Figure 5-1a). Chapter 4 gives full details of the hydrostatic apparatus setup. The pressurization rate was kept at $\sim 1\text{MPa}/\text{min}$ and the confining pressure was held constant at every 10MPa for a period of ~ 10 seconds to record the P and S wave data. Increasing-amplitude cyclic loading experiments were carried out in a standard uniaxial press, where the sample is compressed unconfined ($\sigma_2=\sigma_3=0$) between a fixed rigid plate and a manually controlled moving hydraulic piston (Figure 5-1b). Chapter 3 gives full details of the uniaxial apparatus setup. In the first cycle of the increasing-amplitude cyclic loading experiments, sample WG-SDD, WG-SDI and WG-SDH were taken to $50\% \pm 4\%$ of its unconfined compression strength (UCS) and the stress was then reduced to zero. For the second cycle the sample was taken to $60\% \pm 4.5\%$ of its UCS and then reduced to zero. This pattern was continued until a maximum of $90\% \pm 7\%$ of its UCS was reached. Cycle number is a non-linear proxy for the

amount of microfracture damage. An average of 221MPa differential stress was taken as the UCS of the cored Westerly granite samples (see Table 1). The loading and unloading rates were kept at ~1MPa/min. The load was held constant at every ~6MPa and 10MPa respectively for a period of ~10 seconds to record the P and S wave data. Time-dependent effects are almost negligible to the evolution of static elastic properties of dry Westerly granite for hold time up to 6 hours (Heap and Faulkner, 2008)

The hydrostatic and uniaxial apparatus has two different types of piezoelectric ceramics, one P wave and one S wave with fundamental frequency of 1.5MHz, which are housed in the top and bottom loading platens. Through transmission method was employed to measure simultaneously the P and S wave velocities and attenuation of the samples. The pulsing P and S wave piezoelectric ceramic is aligned with receiving P and S wave piezoelectric ceramic respectively, and both S wave crystals were polarized in the same direction. The standard for using ultrasonic testing to determine pulse velocities (ASTM, 1997a) was adhered to for accurate and reliable measurement of P and S wave velocity (see figure 5-2 for a representative example of P and S wave arrival collected on sample WGA for this study). Sintered stainless steel, 0.125" thick with 0.5 micron nominal pore size, was used as a backing material on the piezoelectric ceramic (VanValkenburg, 1983). The elastic wave impedance of the backing matched the elastic wave impedance of the piezoelectric ceramic resulting in a heavily damped piezoelectric ceramic with wider bandwidth that displays good range resolution. A negative spike pulser / receiver (JSR DPR300 Pulser / Receiver) was used for excitation of the piezoelectric ceramics and detection of the pulse. The choice of piezoelectric ceramics to excite or receive is manually controlled by a switch box. A 300MHz bandwidth digital oscilloscope with 20ppm time based accuracy (Tektronix TDS 3032B) is employed for recording and display of the received pulse which is synchronized with the pulser/receiver. The oscilloscope can also average up to 512 signals to reduce noise. The pulser/receiver and oscilloscope are coupled to a computer for storage of data, and processing of the recorded waveforms for analysis.

All measurements were made on oven dry (at 80°C) intact Westerly granite samples under ambient laboratory conditions, with temperatures approximately 20°C. Westerly granite from south-east Rhode Island, USA, has low initial crack density, small grain size (average 1mm), has an extensive history of laboratory testing, can provide a high level of repeatability under carefully controlled test conditions, and generally considered to be isotropic [Lockner, 1998; Haimson and Chang, 2000]. For viable data set, the samples were cored, 20mm diameter, from the same block, in the same orientation to allow results to be comparable, cut so their length-to-diameter ratios were in excess of 2.5 but less than 3 and precision-ground to strict tolerances (± 0.02 mm) as to the squareness of their ends (Paterson and Wong, 2005). A surface finish of approximately 0.1Ra on the ends of the samples was achieved.

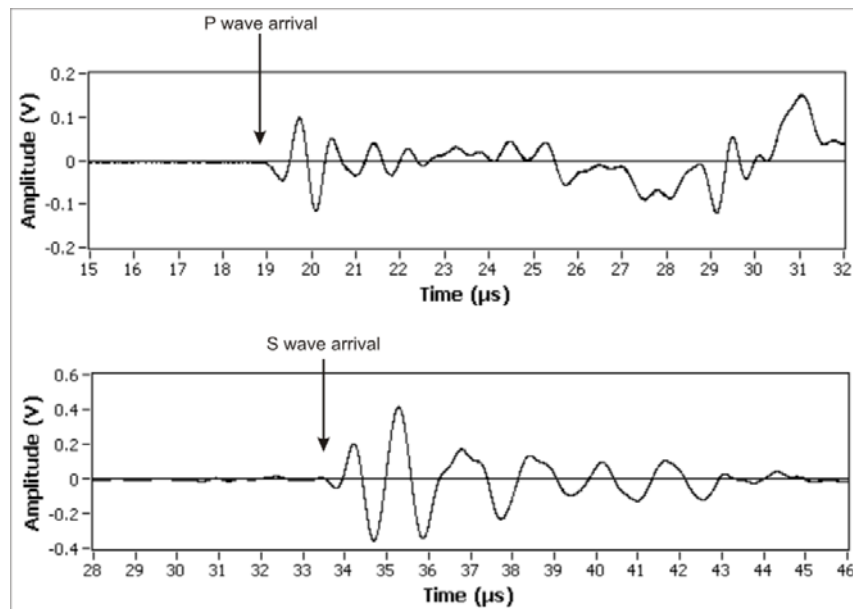


Figure 5-2. P and S wave arrival of sample WGA. Top: Pulsing with P wave piezoelectric ceramic and receiving with P piezoelectric ceramic trace. Bottom: Pulsing with S piezoelectric ceramic and receiving with S piezoelectric ceramic trace. Excitation pulse is at 0 μ s.

Sample	Experiment type	Failure Stress (MPa)	No. Of cycles	Note
WG-SDC	UCS	205.86	NA	To determine UCS
WG-SDB	UCS	217.88	NA	To determine UCS
WG-SDG	UCS	223.81	NA	To determine UCS
WG-SDE	UCS	239.34	NA	To determine UCS
WGA	Hydrostatic	NA	NA	For repeatability
WGB	Hydrostatic	NA	NA	For repeatability
WGD	Hydrostatic	NA	NA	For repeatability
WG-SDD	Increasing-amplitude cyclic loading	NA	5	For repeatability
WG-SDI	Increasing-amplitude cyclic loading	NA	5	For repeatability
WG-SDH	Increasing-amplitude cyclic loading	NA	5	For repeatability

Table 5-1. Summary of experiments.

Absolute measurement of attenuation is a formidable task as seismic wave amplitude is affected by geometric spreading, reflections, scattering, and intrinsic damping. The main laboratory techniques used to measure attenuation is spectral ratio and rise of time technique. Tarif and Bourbie (1987) estimated the relative accuracies of the spectral ratio and rise time techniques and found that the spectral ratio technique is reliable and easy to implement for Q values between 5 and 50, the rise time technique enables high attenuations ($Q < 5$) to be measured, and both techniques lack precision for low attenuation ($Q > 100$). In the procedure outlined by Toksöz *et al.* (1979), the amplitudes of plane seismic waves for the reference and the sample are expressed as:

$$A_1(f) = G_1(x)e^{-\alpha_1(f)x}e^{i(2\pi ft - K_1x)} \quad \text{Equation 5-1}$$

and

$$A_2(f) = G_2(x)e^{-\alpha_2(f)x}e^{i(2\pi ft - K_2x)} \quad \text{Equation 5-2}$$

where A is the amplitude, f is the frequency, x is the distance, $K = 2\pi f/v$ is the wave number, v is velocity and $G(x)$ is a geometrical factor which includes beam spreading, reflections etc., and $\alpha(f)$ is the frequency dependent attenuation coefficient. The subscripts 1 and 2 refer to the reference and the sample

respectively. It is assumed that α is a linear function of frequency, although the method itself tests this assumption (Jackson and Anderson, 1970; Knopoff, 1964; McDonal et al., 1958).

According to *Toksöz et al. (1979)*, the following relationship can be established:

$$\alpha(f) = \gamma f \quad \text{Equation 5-3}$$

where γ is a constant and is related to the quality factor, Q, by

$$Q = \pi/\gamma\nu \quad \text{Equation 5-4}$$

When the same geometry is used for both the sample and reference (i.e. same sample dimensions, piezoelectric ceramic holders, and arrangements), then G_1 and G_2 are frequency-independent scale factors. The ratio of the Fourier amplitudes is

$$\frac{A_1}{A_2} = \frac{G_1}{G_2} e^{-(\gamma_1 - \gamma_2)fx} \quad \text{Equation 5-5}$$

or

$$\ln \left(\frac{A_1}{A_2} \right) = (\gamma_1 - \gamma_2)xf + \ln \left(\frac{G_1}{G_2} \right) \quad \text{Equation 5-6}$$

When G_1/G_2 is independent of frequency, $(\gamma_2 - \gamma_1)$ can be found from the slope of the line fitted to $\ln (A_1/A_2)$ versus frequency (Figure 5-3). If the Q of the standard reference is known, γ_2 of the sample can be determined. When the Q of the standard is high (i.e. $Q \approx \infty$), then $\gamma_1 = 0$, and γ_2 of the rock sample can be determined directly from the slope. In fact, a reference material with a Q factor value greater than 1000 introduces an error less than 1%. Mild steel is used as the reference which has a Q value much greater than 1000 (between 7000 to 16000) (Burnyshev et al., 2005). A more serious concern is the validity of the assumption that the geometric factors G_1 and G_2 have the same frequency dependence, and G_1/G_2 is independent of frequency. With polished rock surfaces and good coupling between the piezoelectric ceramic holder and sample, one would not expect frequency-dependent reflection coefficients at the interface.

In our calculation of the Q factor, the linear region is taken in the frequency range of 0.8MHz – 1.7MHz. A Hanning window was applied to the averaged signals to minimize Gibbs' phenomenon (a distortion or leakage due to

discontinuities in the frequency domain) (Hamming 1977). Fast Fourier transform is then performed on the first 2 periods of the P and S wave arrivals, of the reference and sample (Figure 3).

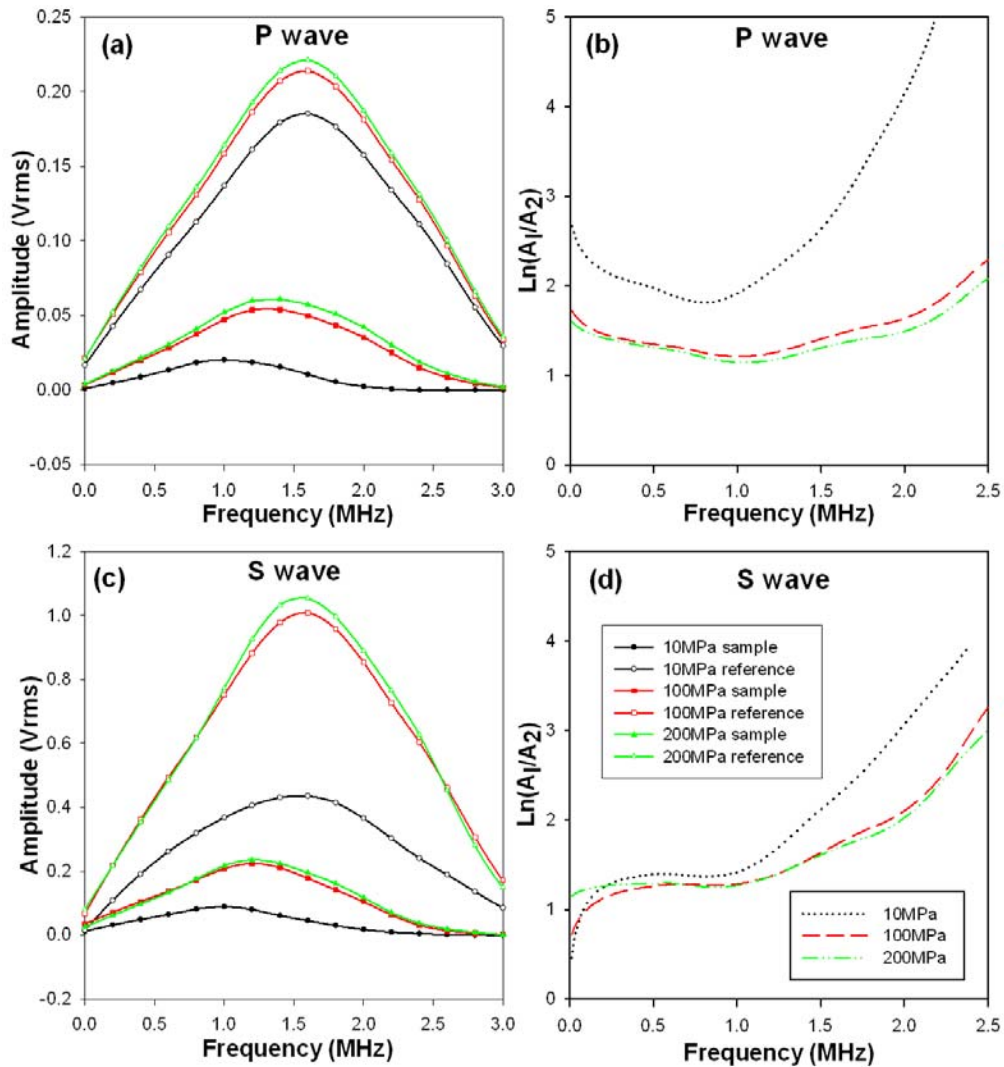


Figure 5-3. Attenuation characteristics of the sample and reference at different hydrostatic confining pressure. Left: The magnitude of the fast Fourier transform of the first 2 periods of the P (a) and S wave (c) arrivals. Right: The spectral amplitude ratio of the reference to the sample of the P (b) and S wave (d). The linear portion is taken between 0.8MHz to 1.7MHz where a linear least square fit line is drawn through the data points. This verifies the linearity assumption made in the calculation.

5.4 Results

In the hydrostatic confining condition, the P and S wave velocities and attenuation showed stress dependency. The P and S wave velocities increased from 5.1km/s to 6km/s and 3km/s to 3.5km/s respectively as the confining pressure increased (Figure 5-4 a and c) from 2MPa to 200MPa. In the first 130MPa confining pressure, the P and S wave velocities increased rapidly in a non-linear manner and as the confining pressure increased to 200MPa the velocities increased linearly with gentle slope. The Q factor of the P wave increased linearly with a steep slope, from 23 to 54 for confining pressure up to 100MPa, and then a gentle slope, from 54 to 60 for confining pressure up to 200MPa. Whereas, the Q factor of the S wave increased gradually from 39 to 54 as the confining pressure increased from 10MPa to 200MPa. In our experiments, the Q factor of the S wave was not reliable when the confining pressure was at 2MPa.

Figure 5-5 shows the P and S wave velocities and attenuation of sample WG - SDD under increasing-amplitude cyclic loading. Stress dependency of the P and S wave velocities and attenuation is also seen. If a single cycle is considered in Figure 5-5 (cycle 3 in this example), the P and S wave velocity increased from 4.9km/s to 5.6km/s and 2.9km/s to 3.1km/s respectively. Above ~140MPa differential stress, the P and S wave velocity tend to stabilize. The Q factor of the P wave increased rapidly from 14 to 41 for differential stress up to 60MPa (Figure 5-5b). Above 60MPa differential stress, the Q factor increased nominally to 47. The Q factor for the S wave also increased rapidly from 11 to 31 for differential stress up to 30MPa (Figure 5-5d). Above 30MPa differential stress, the Q factor increased nominally to 33. The samples accumulate microcrack damage when they exceed the perfectly elastic deformation region (about a 1/3 to 2/3 of the UCS (Bieniawski, 1967a; Brace et al., 1966)). At a constant stress level (58MPa differential stress in this example), there is a decrease in velocity (~2% for P wave and ~3% for S wave) and increase in attenuation (~14% for P wave and ~24% for S wave) (Figure 5-6) as the number of cycle increased.

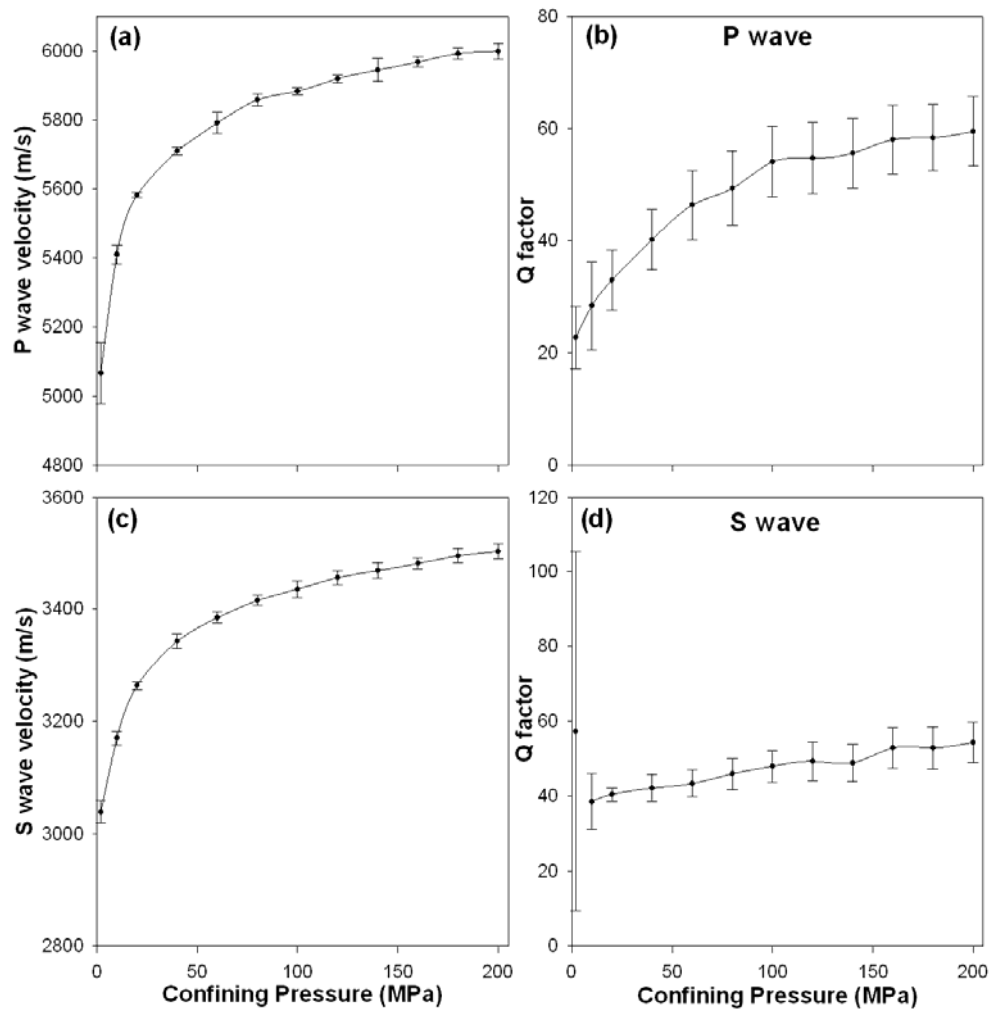


Figure 5-4. P (a) and S wave (c) velocities and attenuation (b and d) as a function of confining pressure. Errors are calculated from repetition of measurements from samples WGA, WGB, and WGD.

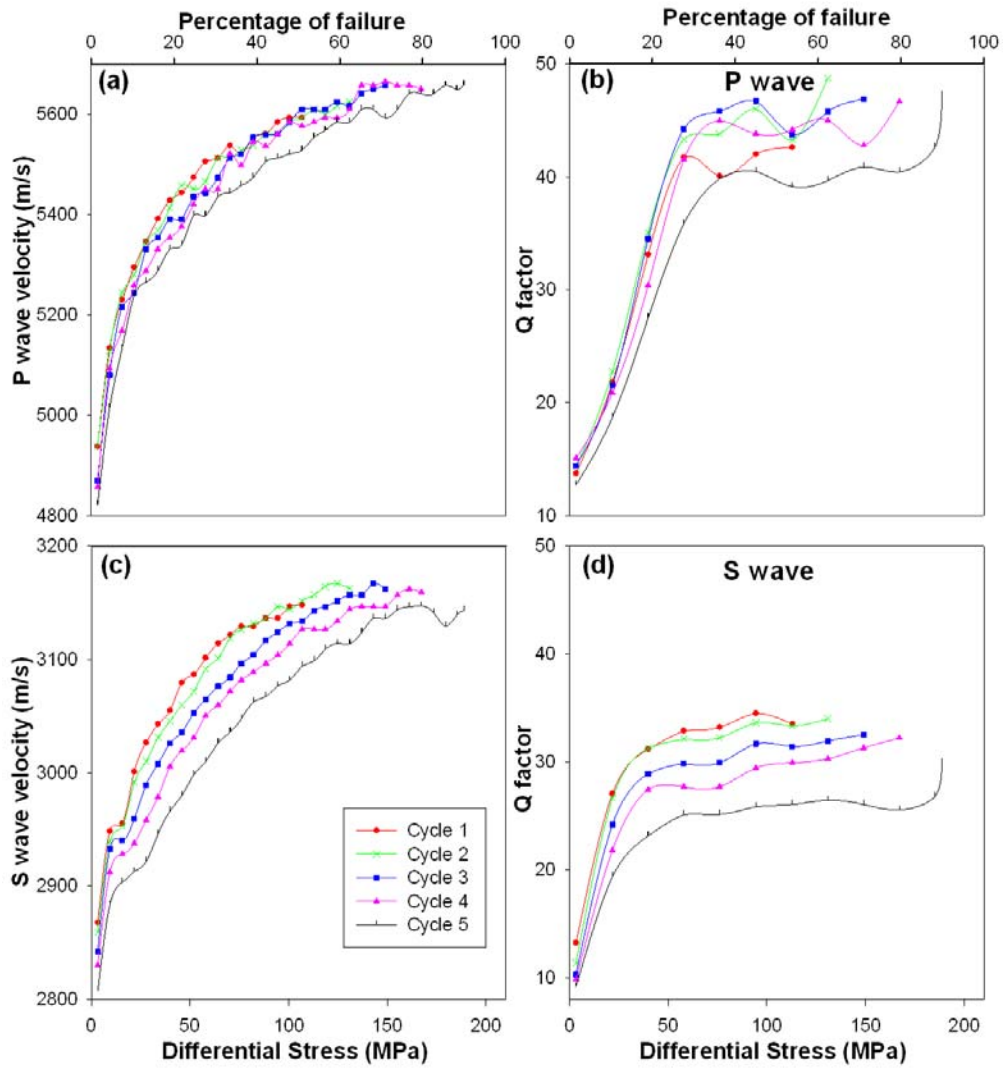


Figure 5-5. P (a) and S wave (c) velocities and attenuation (b and d) of sample WG-SDD under increasing-amplitude cyclic loading . The unloading measurements are shown.

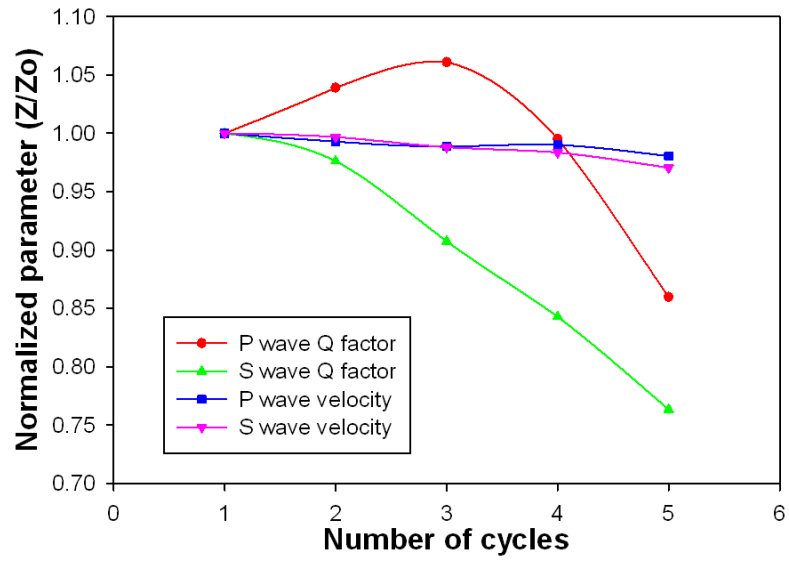


Figure 5-6. Normalized parameters as a function of number of cycles. Z is the P or S wave velocity, or P or S wave Q factor at a given cycle number. Z_0 is the P or S wave velocity, or P or S wave Q factor at the first cycle. These parameters were taken at 58MPa differential stress.

5.5 Discussion

The main mechanisms responsible for attenuation in crustal rocks are:

1. Frictional dissipation due to sliding on crack surfaces and grain boundaries (Gordon and Davis, 1968; Lockner et al., 1977; Walsh, 1966). The Q factor is generally independent of frequency.
2. Scattering, a geometrical effect, where energy is lost from the interaction of seismic wave with cracks and pores. Scattering effects can be important, if not dominant, at high ultrasonic frequencies (frequency > 1 MHz). At seismic frequencies, scattering due to pores is negligible (Johnston et al., 1979).
3. Viscosity of saturating fluids, where attenuation peaks due to viscous relaxation developing at frequencies dependent both on pore geometry and fluid viscosity (Kuster and Toksöz, 1974; Solomon, 1973; Walsh, 1968; Walsh, 1969).
4. Flow of saturating fluids, where fluid flow between pores induced by seismic waves resulting in attenuation. This mechanism falls into two groups: inertial flow (Biot, 1956a; Biot, 1956b) which is important at ultrasonic frequencies; and squirting flow (Mavko and Nur, 1975; O'Connell and Budiansky, 1977a), more prominent at lower frequencies.

In our experiments, the mechanisms responsible for attenuation are frictional dissipation and scattering. *Johnston et al.* (1979) modelled the behaviour of attenuation as a function of differential pressure for dry and saturated rocks, and found that friction on grain boundaries and thin cracks is the primary mechanism for attenuation.

The stress dependency of the P and S wave velocities and attenuation during the hydrostatic confining and uniaxial compressive conditions can be explained by crack closure. In the uniaxial compressive conditions, cracks that are oriented transversely and obliquely to the axial loading direction are closed during loading of the sample, whereas cracks are closed in all direction during pressurization in the hydrostatic confining condition. This caused the velocities and Q factors to be lesser in the uniaxial compressive condition compared to those in the hydrostatic condition. The rapid nonlinear increase in the

velocities below 130MPa, in the hydrostatic confining condition, is referred to as the crack-closing pressure. Below this pressure, microcrack closure is responsible for the non linear rapid increase of the velocities and above this pressure, the intrinsic properties (elastic compaction of a crack-free rock) are observed (Birch, 1960; Kern, 1978; Kern, 1990). The crack-closing pressure can also be seen in the P wave Q factor where the gradient of the linear increase changes from steep to gentle. However, this change of gradient occurs at 100MPa. *Meglis et al.*(1996) and *Toksöz et al.* (1979) also found that cracks are closed with increasing confining pressure which results in an increase in velocity and decrease in attenuation. The results of the range of the P wave attenuation are oddly similar to the in situ results, at 50 – 1500Hz, measured by *Holliger and Bühnemann* (1996) as it is expected that attenuation at ultrasonic frequencies is higher than at seismic frequencies. *Holliger and Bühnemann* (1996) studied the attenuation of high-quality, broad-band (50-1500Hz) borehole-to-tunnel seismic data acquired inside a granite body cut by brittle faults. They reported Q-values, estimated from P-wave first arrivals by the spectral ratio and rise time techniques, ranging from about 20 to 60 with a median value of 35 and a standard error of 20% or less. Macrocracks and fluid saturation of the granite body are likely responsible for the high attenuation.

The standard deviation of the P and S wave velocities is very small compared to those of the P and S wave attenuation. The large standard deviation of the P and S wave attenuation are likely due to coupling between the sample and the loading platens. A non-uniform air gap between the sample and loading platens exists which alters the transmission characteristics of the ultrasonic waves. To reduce the effect of a non-uniform air gap, an elastic wave couplant such as water, glycerin, grease, petroleum jelly, or oil can be used (Krautkramer and Krautkramer, 1990). The couplant should be kept as thin as possible, as increasing the thickness will degrade the transmitted signal. We found that elastic wave couplant improved the P wave arrival and made it difficult to pick the S wave arrival as the couplant increases the amplitude of the P to S and S to P conversion waves. These conversion waves arrive before the S wave arrival.

Increasing-amplitude cyclic loading experiments caused an increase in microcrack damage. During each cycle of the experiment, the elastic limit of the rock sample was exceeded which results in permanent deformation. The majority of the newly initiated microcracks and crack growth are oriented in the same direction as the applied stress, which is evident in a ~3% decrease in S wave velocity compared to ~2% decrease in P wave velocity; as the S wave is polarized normal to the loading direction. This is also corroborated by thin section analysis done by [Heap and Faulkner (2008)]. Attenuation is much more sensitive to microcrack damage than velocity, as our results show that attenuation increased by ~14% for P wave and ~24% for S wave.

The assumption that G_1/G_2 (Equation 5) is independent of frequency may not be strictly valid and hence diffraction corrections are necessary (Klimentos, 1991). Diffraction corrections are outlined by Seki *et al.* (1956) and extended by Papadakis (1975). If these corrections are not considered, the measured attenuation will be overestimated (Sears and Bonner, 1981). However, broadband pulses (i.e. generated by spiked or rectangular voltage pulses applied to heavily dampened transducers) tend to average out the effect of diffraction because they contain spectrum of frequencies, each of which experiences diffraction effects at a different distance from the transducer (Papadakis, 1975). Hence, the negative spike pulser and heavily damped piezoelectric ceramic used in our methodology averaged out the effect of any possible diffraction.

5.6 Conclusion

Laboratory experiments were carried out on crystalline rocks using piezoelectric ceramic that has a fundamental frequency of 1.5MHz under hydrostatic confining and uniaxial compressive conditions. Attenuation measurements were made in the frequency range of 0.8MHz to 1.7MHz. In our experiments, the mechanisms responsible for attenuation are frictional dissipation and scattering. The effect of these mechanisms was minimized with the closure of microcracks and maximized when microcrack damage was induced in the sample. Increasing confining pressure closed microcracks in all directions which resulted in an overall 18% and 17% increase in the P and S wave velocity respectively, and a 161% and 38% decrease in P and S wave attenuation respectively. In the case of the increasing-amplitude cyclic loading experiments, cracks that are oriented transversely and obliquely to the axial loading direction are preferentially closed during loading of the sample, which resulted in an overall ~14% and 7% increase in the P and S wave velocity respectively, and a ~236% and 200% decrease in P and S wave attenuation respectively. The Q factor of the P wave is greater than the Q factor of the S wave in the hydrostatic confining and uniaxial compressive conditions.

Increasing-amplitude cyclic loading experiments caused an increase in microcrack damage. At a constant stress level, there is a decrease in velocity (~1% for P wave and ~2.2% for S wave) and increase in attenuation (~14% for P wave and ~25% for S wave) as the number of cycles increased. Our results showed that seismic wave attenuation is more sensitive than seismic wave velocity to the effect of increasing confining pressure and differential stress, and microcrack damage.

6 Summary and further work

The primary aims of this thesis and the specific issues to be addressed were outlined in the first chapter. These issues were addressed in chapters 3 to 5 and hence will not be discussed in detail here. This chapter presents a summary of these results, implications for use of seismic waves to assess degree of fracture in the crust and outlines suggestions for further work.

6.1 Summary of results

Strong stress-dependency of P and S wave velocities and attenuation, V_p/V_s and elastic properties exists in the uniaxial compressive and hydrostatic confining conditions due to closure of microcracks. In the uniaxial compressive condition, cracks that are orientated oblique and perpendicular to the compression direction are closed with increasing differential stress. This resulted in a marked increase in the P and S wave velocities, dynamic and static Young's modulus, and static Poisson's ratio. The dynamic Poisson's ratio and V_p/V_s increased slightly. The P and S wave Q factors also exhibited a larger increase compared to the other parameters. Moreover, the Q factor of the P wave is greater than the Q factor of the S wave. In the case of hydrostatic confining condition, all the cracks are closed with increasing confining pressure. The changes in velocities, V_p/V_s , dynamic elastic properties, and attenuation follow similar trends to those in the uniaxial compressive condition. However, the P and S wave velocities and Q factors and dynamic Young's modulus are higher and the dynamic Poisson's ratio and V_p/V_s are lower. The P and S wave velocities and Young's modulus of samples that have a greater amount of induced microcrack damage required higher confining pressure to be equal to those of samples with no induced microcrack damage. The crack closure pressure, where cracks are totally closed, for the Westerly granite samples is about 130MPa and is independent of the amount of microcrack damage induced into the samples.

The rock accumulates microcrack damage when the applied stress exceeds the elastic region. Bieniawski [1967a] found that this stage finishes at ~35% of the UCS of the sample, while Brace [1966] found this stage can end at one-third to two-third of the UCS of the sample. The higher the applied stress

above the elastic region, the more microcrack damage the samples accumulates. The applied stress is non linear to microcrack damage. The accumulation of microcrack damage caused: a decrease in the P and S wave velocities and static and dynamic Young's modulus; a small increase in the dynamic Poisson's ratio and V_p/V_s ; and a large increase in the static Poisson's ratio, and P and S wave attenuation.

Increasing-amplitude cyclic loading experiments showed that at low differential stress, the dynamic Young's modulus is greater than the static Young's modulus. Both moduli are equal at intermediate differential stress. At high differential stress level the static Young's modulus is greater than the dynamic Young's modulus. A linear relationship was established between the static and dynamic Young's modulus. The gradient and intercept of the linear relationship between static and dynamic Young's modulus change as the number of cycle increases. The static Poisson's ratio is much greater than the dynamic Poisson's ratio with exception to the first cycle. Bulging of the sample during the experiment affected the static Poisson's ratio but cannot completely describe the difference seen between static and dynamic properties. Several other factors contribute to the difference between the static and dynamic elastic properties: (1) microcracks - dynamic properties are calculated from wave propagation that interacts with microcracks within the propagating path, while the static properties are influenced by the overall micocracks within the sample; (2) frequency – static elastic properties can be considered to be measured quasi-statically, whereas the dynamic elastic properties were measured at a much higher frequency (1.5MHz); (3) strain amplitude – static elastic measurements were accompanied by large strain amplitudes (10^{-2}), whereas dynamic elastic properties are determined by wave propagation with extremely small strain amplitude (10^{-6}).

6.2 Implications for use of seismic waves to access rock fracture state in the crust

Assessment of the degree of fracture in rocks is important as they play an essential role: in many geomechanical issues such as stability of boreholes,

stimulation of oil and geothermal reservoirs, the design of civil structures, tunnels and hazardous waste disposals; and in understanding a number of processes in the Earth's crust such as magmatic intrusions, plate tectonics, fault mechanics and sedimentary basins. Seismic waves velocity and attenuation can be use to assess the degree of fracture. Seismic wave attenuation is much more sensitive to fractures than seismic wave velocity. Our results showed that the change in attenuation due to an increase in fracture density is 14 times more than the change in P wave velocity and 11 times more than the change in S wave velocity.

Fractures within rocks are closed when they are subjected to increasing hydrostatic confining pressure (depth). We found that fractures are completely closed at ~5km in dry crystalline rocks. At shallow depth (less than 5km), fracture density affects seismic wave velocities. We observed an overall 6% and 4% reduction in P and S wave velocities respectively due to an increase in the fracture density. The overall reduction in the P and S wave decreased to 2% and 1% at ~2km. Consequently, assessing the degree of fracture between 2km and 5km using seismic wave velocities may be difficult. Assessing the degree of fracture in this region is possible by using seismic wave attenuation data as attenuation is much more sensitive than velocity. We were not able to assess the effect of fracture density on seismic wave attenuation under hydrostatic confining pressure because attenuation is also affected by the air gaps between the interfaces of the sample and loading platens. It is very difficult to keep the air gap between the samples with different amount of fracture density uniform. To reduce the effect of the non-uniform air gap, an elastic wave couplant such as water, glycerin, grease, petroleum jelly, or oil can be used [Krautkramer and Krautkramer, 1990]. However, using an elastic wave couplant presents its own problems (see Chapter 2, section 2.6.3)

The dynamic elastic properties that are derived from the seismic wave velocities do not fully reflect the static elastic properties. The static elastic properties are more susceptible to the effect of fractures.

6.3 Scope for further work

In our experiments, we were able to control and provide a qualitative assessment of the fracture density. Numerous models which predict properties of materials as a function of damage have been developed in the framework of effective medium theories (e.g. Anderson et al., 1974; Cheng and Toksöz, 1979; Henyey and Pomphrey, 1982; Hudson, 1981; Hudson, 1986; Hudson, 1990; Kachanov, 1994; Nishizawa, 1982; O'Connell and Budiansky, 1974; O'Connell and Budiansky, 1977b; Sayers and Kachanov, 1991; Soga et al., 1978; Walsh, 1965a; Walsh, 1965b). The major limitations of these models are that they do not account for: (1) interaction of cracks, (2) cracks that are not uniformly distributed spatially, and (3) complex shapes of fractures. However, they provide useful insight into the micromechanics of brittle failure of rocks and can be used with the inversion of the measured P and S wave velocities and elastic properties to provide a quantitative approximation of the crack density and crack aspect and ratio (width to length).

The majority of the newly initiated microcracks and crack growth are oriented in the same direction as the applied stress. In our calculation of the dynamic elastic properties, we assumed isotropy which will lead to uncertainties in the dynamic elastic properties, especially as the number of cycles increases. Furthermore, if cracks are closed in some directions but are opened in other directions, the rock will exhibit a directional dependence of the effective elastic parameters and are, in general, anisotropic. However, it is much more difficult to experimentally characterize the elastic properties of an anisotropic rock. Additional piezoelectric ceramics could be attached to the outer diameter of the core sample to measure the seismic velocities in three orthogonal directions simultaneously. This would enable the measurement of seismic velocity anisotropy and transverse isotropy evolution as microcracks are induced in the sample.

Investigations of the dynamic Poisson's ratio are rare due to the difficulties in determining the shear wave velocity. Consequently, very limited data relating the static and dynamic Poisson's ratio have been published. We

were able to measure P and S wave velocities accurately and reliably, but yet we could not establish a relationship between the static and dynamic Poisson's ratio. We attribute the differences in the static and dynamic elastic properties to the size distribution of the crack population relative to the amplitude and frequency of the applied stress, bulging of the sample due to the uniaxial configuration, and the assumption of isotropic elasticity in the sample. Future work should concentrate on quantifying the effect of these parameters and investigate the significant discrepancy between the static and dynamic Poisson's ratio.

In this thesis, laboratory measurements of velocities, attenuation and elastic properties of rocks were made in uniaxial compressive and hydrostatic confining conditions. Measurements of these parameters could be also made in a triaxial stress state to replicate fully true crustal conditions. The advantages of using a triaxial include:

- Measuring attenuation and velocities as a function of microfracture damage at depth. Controlled microfractures can be induced while the rock sample is at depth.
- Independent measurement of the static Young's modulus, Poisson's ratio and bulk modulus. Then a comparison of the static and dynamic elastic properties can be established at depth.

The presence of fluid is common in the Earth's crust. In our experiments the condition of the microfractures was dry in order to remove the complexity of saturation and fluid type. Similar experiments with different degree of saturation and fluid types could be carried out and then compared with these results to evaluate the coupled effect of saturation and fluid types in fractures on velocities, attenuation and elastic properties.

7 References

- Adam, L. and Batzle, M., 2008, Elastic properties of carbonates from laboratory measurements at seismic and ultrasonic frequencies. *The Leading Edge*, 27: 1026-1032.
- Adelinet, M., Fortin, J., Guéguen, Y., Schubnel, A. and Geoffroy, L., 2010, Frequency and fluid effects on elastic properties of basalt: Experimental investigations. *Geophys. Res. Lett.*, 37: L02303.
- Aki, K. and Richards, P., 2002, *Quantitative seismology*. University Science Books, Sausalito, CA.
- Anderson, D.L., Minster, B. and Cole, D., 1974, The effect of oriented cracks on seismic velocities. *J. geophys. Res.*, 79: 40111-44015.
- Armitage, P., 2008, Petrological and petrophysical characteristics of a siliciclastic caprock, Unpublished PhD thesis, University of Liverpool, Liverpool
- ASTM, 1997a, Standard test method for laboratory determination of pulse velocities and ultrasonic elastic constants of rock (D2845-95). 1997 Annual Book of ASTM Standards, Vol. 4.08. American Society for Testing and Materials (ASTM), Philadelphia, Pa.254–259.
- Batzle, M., Hofmann, R., Han, D.-H. and Castagna, J., 2001, Fluids and frequency dependent seismic velocity of rocks. *The Leading Edge*, 20: 168-171.
- Batzle, M., Han, D.H. and Hofmann, R., 2006, Fluid mobility and frequency-dependent seismic velocity-Direct measurements. *Geophysics*, 71: N1-N9.
- Benson, P.M., Meredith, P.G., Platzman, E.S. and White, R.E., 2005, Pore fabric shape anisotropy in porous sandstones and its relation to elastic wave velocity and permeability anisotropy under hydrostatic pressure.

International Journal of Rock Mechanics and Mining Sciences, 42: 890-899.

Benson, P.M., Meredith, P.G. and Schubnel, A., 2006a, Role of void space geometry in permeability evolution in crustal rocks at elevated pressure. J. Geophys. Res., 111: B12203.

Benson, P.M., Schubnel, A., Vinciguerra, S., Trovato, C., Meredith, P.G. and Young, R.P., 2006b, Modeling the permeability evolution of microcracked rocks from elastic wave velocity inversion at elevated isostatic pressure. J. Geophys. Res., 111: B04202.

Bieniawski, Z.T., 1967a, Mechanism of brittle fracture of rock: Part I - theory of the fracture process. International Journal of Rock Mechanics and Mining Sciences & Geomechanics Abstracts, 4: 395-406.

Bieniawski, Z.T., 1967b, Mechanism of brittle fracture of rock: Part II - experimental studies. International Journal of Rock Mechanics and Mining Sciences & Geomechanics Abstracts, 4: 407-423.

Bieniawski, Z.T., 1967c, Mechanism of brittle fracture of rock: Part III - fracture in tension and under long-term loading. International Journal of Rock Mechanics and Mining Sciences & Geomechanics Abstracts, 4: 425-430.

Bieniawski, Z.T., 1974, Estimating the strength of rock materials. Journal of the South African Institute of Mining and Metallurgy: 312-320.

Biot, M., 1956a, Theory of propagation of elastic waves in a fluid-filled porous solid. I. Low-frequency range. Journal of the Acoustical Society of America, 28: 168-178.

Biot, M., 1956b, Theory of propagation of elastic waves in a fluid-saturated porous solid. II. Higher frequency range. Journal of the Acoustical Society of America, 28: 179-191.

- Birch, F., 1960, The Velocity of Compressional Waves in Rocks to 10-Kilobars .1. *Journal of Geophysical Research*, 65: 1083-1102.
- Birch, F., 1961, Velocity of Compressional Waves in Rocks to 10 Kilobars, .2. *Journal of Geophysical Research*, 66: 2199-2224.
- Blair, D. and Spathis, A., 1982, Attenuation of explosion-generated pulse in rock masses. *Journal of Geophysical Research*, 87: 3885-3892.
- Brace, W.F., 1965, Some new measurements of linear compressibility of rocks. *Journal of Geophysical Research*, 70: 391-398.
- Brace, W.F., Paulding Jr, B. and Scholz, C., 1966, Dilatancy in the fracture of crystalline rocks. *Journal of Geophysical Research*, 71: 3939-3953.
- Brignoli, E., Gotti, M. and Stokoe, K., 1996, Measurement of shear waves in laboratory specimens by means of piezoelectric transducers. *ASTM geotechnical testing journal*, 19: 384-397.
- Bruhn, R.L., Parry, W.T., Yonkee, W.A. and Thompson, T., 1994, Fracturing and hydrothermal alteration in normal fault zones. *Pure and Applied Geophysics*, 142: 609-644.
- Budiansky, B. and O'Connell, R.J., 1976, Elastic moduli of a cracked solid. *International Journal of Solids and Structures*, 12: 81-97.
- Burnyshev, I., Valiakhmetova, O. and Lys, V., 2005, Acoustic quality of hydrogenated low carbon steels. *Technical Physics Letters*, 31: 274-276.
- Caine, J.S., Evans, J.P. and Forster, C.B., 1996, Fault zone architecture and permeability structure. *Geology*, 24: 1025 - 1028.
- Cheng, C.H. and Toksöz, M.N., 1979, Inversion of seismic velocities for the pore aspect ratio spectrum of a rock. *Journal of Geophysical Research*, 84: 7533-7544.

- Cheng, C.H. and Johnston, D.H., 1981, Dynamic and static moduli. *Geophysical Research Letters*, 8: 39-42.
- Christensen, N.I., 1965, Compressional wave velocities in metamorphic rocks at pressures to 10 kilobars. *Journal of Geophysical Research*, 70: 6147-6164.
- Christensen, N.I., 1974, Compressional wave velocities in possible mantle rocks to pressures of 30 kilobars. *Journal of Geophysical Research*, 79: 407-412.
- Christensen, N.I. and Wang, H., 1985, The influence of pore pressure and confining pressure on dynamic elastic properties of Berea sandstone. *Geophysics*, 50: 207-213.
- Ciccotti, M. and Mulargia, E., 2004, Differences between static and dynamic elastic moduli of a typical seismogenic rock. *Geophysical Journal International*, 157: 474-477.
- Coulson, J., 1979, Suggested methods for determining in situ deformability of rock. *Int. J. Rock Mech. Min. Sci. & Geomech. Abstr*, 16: 195-214.
- Crampin, S., Gao, Y. and Peacock, S., 2008, Stress-forecasting (not predicting) earthquakes: A paradigm shift? *Geology*, 36: 427-430.
- David, C., Menéndez, B. and Darot, M., 1999, Influence of stress-induced and thermal cracking on physical properties and microstructure of La Peyratte granite. *International Journal of Rock Mechanics and Mining Sciences*, 36: 433-448.
- Dyvik, R. and Madshus, C., Year, Laboratory measurements of Gmax using bender elements. *American Society of Civil Engineers Conference on Advances in the Art of Testing Soils under Cyclic Conditions*, Detroit, October 24, 186 -196.

- Eberhardt, E., Stead, D. and Stimpson, B., 1999, Quantifying progressive pre-peak brittle fracture damage in rock during uniaxial compression. *International Journal of Rock Mechanics and Mining Sciences*, 36: 361-380.
- Faulkner, D.R., Mitchell, T.M., Healy, D. and Heap, M.J., 2006, Slip on 'weak' faults by the rotation of regional stress in the fracture damage zone. *Nature*, 444: 922-925.
- Friedman, M. and Bur, T., 1974, Investigations of the relations among residual strain, fabric, fracture and ultrasonic attenuation and velocity in rocks. *International Journal of Rock Mechanics and Mining Sciences & Geomechanics Abstracts*, 11: 221-234.
- Gladwin, M. and Stacey, F., 1974, Anelastic degradation of acoustic pulses in rock. *Physics of The Earth and Planetary Interiors*, 8: 332-336.
- Gordon, R. and Davis, L., 1968, Velocity and attenuation of seismic waves in imperfectly elastic rock. *Journal of Geophysical Research*, 73: 3917-3935.
- Haimson, B. and Chang, C., 2000, A new true triaxial cell for testing mechanical properties of rock, and its use to determine rock strength and deformability of Westerly granite. *International Journal of Rock Mechanics and Mining Sciences*, 37: 285-296.
- Hajnal, Z., Stauffer, M., King, M., Wallis, P., Wang, H. and Jones, L., 1983, Seismic characteristics of a Precambrian pluton and its adjacent rocks. *Geophysics*, 48: 569-581.
- Hamiel, Y. and Fialko, Y., 2007, Structure and mechanical properties of faults in the North Anatolian Fault system from InSAR observations of coseismic deformation due to the 1999 Izmit (Turkey) earthquake. *J. Geophys. Res.*, 112: B07412.

- Hawkes, I. and Mellor, M., 1970, Uniaxial testing in rock mechanics laboratories. *Engineering Geology*, 4: 179-285.
- Healy, D., 2008, Damage patterns, stress rotations and pore fluid pressures in strike-slip fault zones. *Journal of Geophysical Research*, 113: B12407.
- Heap, M.J. and Faulkner, D.R., 2008, Quantifying the evolution of static elastic properties as crystalline rock approaches failure. *International Journal of Rock Mechanics and Mining Sciences*, 45: 564-573.
- Henye, F.S. and Pomphrey, N., 1982, Self-consistent elastic moduli of a cracked solid. *Geophysical Research Letters*, 9: 903–906.
- Heuze, F.E., 1983, High-temperature mechanical, physical and Thermal properties of granitic rocks - A review. *International Journal of Rock Mechanics and Mining Sciences & Geomechanics Abstracts*, 20: 3-10.
- Heuze, F.E., 1984, Suggested Method for Estimating the In-Situ Modulus of Deformation of Rock Using the NX-Borehole Jack. *Geotechnical Testing Journal*, 7: 205-210
- Holcomb, D.J. and Costin, L.S., 1986, Detecting damage surfaces in brittle materials using acoustic emissions. *Journal of Applied Mechanics*, 53: 536.
- Holcomb, D.J., 1993, General theory of the Kaiser effect. *International Journal of Rock Mechanics and Mining Sciences & Geomechanics Abstracts*, 30: 929-935.
- Holliger, K. and Bühnemann, J., 1996, Attenuation of broad band (50–1500 Hz) seismic waves in granitic rocks near the Earth's surface. *Geophysical Research Letters*, 23: 1981-1984.
- Hooker, M., 1998, Properties of PZT-Based Piezoelectric Ceramics Between–150 and 250°C.

- Hudson, J.A., 1981, Wave speeds and attenuation of elastic waves in material containing cracks. *Geophysical Journal of the Royal Astronomical Society*, 64: 133-150.
- Hudson, J.A., 1986, A higher order approximation to the wave propagation constants for a cracked solid. *Geophysical Journal of the Royal Astronomical Society*, 87: 265-274.
- Hudson, J.A., 1990, Overall elastic properties of isotropic materials with arbitrary. *Geophysical Journal International*, 102: 465-469.
- Jackson, D. and Anderson, D., 1970, Physical mechanisms of seismic-wave attenuation. *Reviews of Geophysics*, 8: 1-63.
- Jaeger, J.C., Cook, N.G.W. and Zimmerman, R.W., 2007, *Fundamentals of rock mechanics*. Wiley-Blackwell
- Johnston, D., Toksöz, M. and Timur, A., 1979, Attenuation of seismic waves in dry and saturated rocks: II. Mechanisms. *Geophysics*, 44: 691-711.
- Johnston, D. and Toksöz, M., 1980, Ultrasonic P and S wave attenuation in dry and saturated rocks under pressure. *Journal of Geophysical Research*, 85: 925-936.
- Juhlin, C., 1995, Imaging of fracture zones in the Finnsjön area, central Sweden, using the seismic reflection method. *Geophysics*, 60: 66-75.
- Kachanov, M., 1994, Elastic Solids with Many Cracks and Related Problems. In: John, W.H. and Theodore, Y.W. (eds.), *Advances in Applied Mechanics*. Elsevier 259-445.
- Kaiser, J., 1950, An investigation into the occurrence of noises in tensile tests, or a study of acoustic phenomena in tensile tests. Ph. D. thesis, Technische Hochschule, München, Germany.
- Karakus, M., Kumral, M. and Kilic, O., 2005, Predicting elastic properties of intact rocks from index tests using multiple regression modelling.

International Journal of Rock Mechanics and Mining Sciences, 42: 323-330.

Kern, H., 1978, The effect of high temperature and high confining pressure on compressional wave velocities in quartz-bearing and quartz-free igneous and metamorphic rocks. *Tectonophysics*, 44: 185-203.

Kern, H., 1990, Laboratory seismic measurements: an aid in the interpretation of seismic field data. *Terra Nova*, 2: 617-628.

King, M.S., 1983, Static and Dynamic Elastic Properties of Rocks from the Canadian Shield. *International Journal of Rock Mechanics and Mining Sciences*, 20: 237-241.

Kitamura, K., Takahashi, M., Mizoguchi, K., Masuda, K., Ito, H. and Song, S.-R., 2010, Effects of pressure on pore characteristics and permeability of porous rocks as estimated from seismic wave velocities in cores from TCDP Hole-A. *Geophysical Journal International*, 182: 1148-1160.

Kjartansson, E., 1979, Constant Q-wave propagation and attenuation. *Journal of Geophysical Research*, 84: 4737-4748.

Klimentos, T., 1991, Geometric Corrections in Attenuation Measurements. *Geophysical Prospecting*, 39: 193-218.

Knopoff, L., 1964, Solid-earth geophysics. *Q. Rev. Geophys*, 2: 625–660.

Krautkramer, J. and Krautkramer, H., 1990, *Ultrasonic testing of materials*. Springer-Verlag, Berlin, Heidelberg, and New York.

Kurita, K. and Fujii, N., 1979, Stress memory of crystalline rocks in acoustic emission. *Geophysical Research Letters*, 6: 9-12.

Kuster, G. and Toksöz, M., 1974, Velocity and attenuation of seismic waves in two phase media: Part I. Theoretical formulations. *Geophysics*, 39: 587 - 606.

- Kuttruff, H., 1991, Ultrasonics fundamentals and applications. Elsevier Science & Technology
- Lama, R. and Vutukuri, V., 1978, Handbook on mechanical properties of rocks: testing techniques and results. Trans Tech Publ
- Lau, J.S.O. and Chandler, N.A., 2004, Innovative laboratory testing. International Journal of Rock Mechanics and Mining Sciences, 41: 1427-1445.
- Li, X.S. and Nakagawa, K., 1997, Pulse transmission system for measuring wave propagation in soils. Journal of Geotechnical & Geoenvironmental Engineering, 123: 883.
- Lockner, D., Walsh, J. and Byerlee, J., 1977, Changes in seismic velocity and attenuation during deformation of granite. Journal of Geophysical Research, 82: 5374-5378.
- Lockner, D., 1998, A generalized law for brittle deformation of Westerly granite. J. geophys. Res, 103: 5107-5123.
- Loureiropinto, J., 1986, Suggested Method for Deformability Determination Using a Large Flat Jack Technique. International Journal of Rock Mechanics and Mining Sciences, 23: 131-140.
- Martin, C.D. and Chandler, N.A., 1994, The Progressive Fracture of Lac Du Bonnet Granite. International Journal of Rock Mechanics and Mining Sciences & Geomechanics Abstracts, 31: 643-659.
- Mavko, G. and Nur, A., 1975, Melt squirt in the asthenosphere. Journal of Geophysical Research, 80: 1444-1448.
- McDonal, F., Angona, F., Mills, R., Sengbush, R., Van Nostrand, R. and White, J., 1958, Attenuation of shear and compressional waves in Pierre Shale. Geophysics, 23: 421 - 433.

- Meglis, I., Greenfield, R., Engelder, T. and Graham, E., 1996, Pressure dependence of velocity and attenuation and its relationship to crack closure in crystalline rocks. *Journal of Geophysical Research*, 101: 17523–17533.
- Meredith, P.G. and Atkinson, B.K., 1985, Fracture toughness and subcritical crack growth during high-temperature tensile deformation of Westerly granite and Black gabbro. *Physics of The Earth and Planetary Interiors*, 39: 33-51.
- Michihiro, K., Fujiwara, T. and Yoshioka, H., Year, Study on estimating geostresses by the Kaiser effect of AE.
- Milkereit, B., Green, A., Wu, J., White, D. and Adam, E., 1994, Integrated seismic and borehole geophysical study of the Sudbury Igneous Complex. *Geophysical Research Letters*, 21: 931-934.
- Mockovčiaková, A. and Pandula, B., 2003, Study of the Relation Between the Static and Dynamic Moduli of Rocks. *Metalurgija*, 1: 37-39.
- Moos, D. and Zoback, M., 1983, In situ studies of velocity in fractured crystalline rocks. *Journal of Geophysical Research*, 88: 2345-2358.
- Murphy III, W.F., 1984, Seismic to ultrasonic velocity drift: Intrinsic absorption and dispersion in crystalline rock. *Geophysical Research Letters*, 11: 1239-1242.
- Nakagawa, K., Soga, K. and Mitchell, J., 1996, Pulse transmission system for measuring wave propagation in soils. *Journal of Geotechnical Engineering*, 122: 302 – 308.
- Nasser, M.H.B., Schubnel, A. and Young, R.P., 2007, Coupled evolutions of fracture toughness and elastic wave velocities at high crack density in thermally treated Westerly granite. *International Journal of Rock Mechanics and Mining Sciences*, 44: 601-616.

- Nishizawa, O., 1982, Seismic velocity anisotropy in a medium containing oriented cracks: Transversely isotropic case. *Journal of Physics of the Earth*, 30: 331–347.
- Nur, A. and Simmons, G., 1969, The effect of saturation on velocity in low porosity rocks. *Earth and Planetary Science Letters*, 7: 183-193.
- O'Connell, R. and Budiansky, B., 1977a, Viscoelastic properties of fluid-saturated cracked solids. *Journal of Geophysical Research*, 82: 5719-5736.
- O'Connell, R.J. and Budiansky, B., 1974, Seismic Velocities in Dry and Saturated Cracked Solids. *Journal of Geophysical Research*, 79: 5412-5426.
- O'Connell, R.J. and Budiansky, B., 1977b, Viscoelastic properties of fluid-saturated cracked solids. *Journal of Geophysical Research*, 82: 5719-5736.
- O'doherty, R. and Anstey, N., 1971, Reflections on amplitudes. *Geophysical Prospecting*, 19: 430-458.
- Papadakis, E., 1975, Ultrasonic diffraction from single apertures with application to pulse measurements and crystal physics. *Physical Acoustics*, 11: 151-211.
- Paterson, M. and Wong, T., 2005, *Experimental rock deformation--the brittle field*. Springer Verlag
- Peacock, S., McCann, C., Sothcott, J. and Astin, T., 1994, Seismic velocities in fractured rocks: an experimental verification of Hudson's theory. *Geophysical Prospecting*, 42: 27-80.
- Pyrak-Nolte, L., Myer, L. and Cook, N., 1990, Anisotropy in seismic velocities and amplitudes from multiple parallel fractures. *Journal of Geophysical Research*, 95: 11345 - 11358.

- Safari, A. and Akdoğan, E.K., 2008, Piezoelectric and acoustic materials for transducer applications. Springer Science+Business Media, LLC
- Saleh, B., Malkawi, A.I.H. and Blum, P.A., 1996, In situ determination of a rock mass modulus using a high resolution tiltmeter. Canadian geotechnical journal, 33: 350-355.
- Sayers, C.M. and Kachanov, M., 1991, A simple technique for finding effective elastic constants of cracked solids for arbitrary crack orientation statistics. International Journal of Solids and Structures, 27: 671-680.
- Schmerr Jr, L. and Song, S., 2007, Ultrasonic Nondestructive Evaluation Systems - Models and Measurements. Springer
- Schoenberger, M. and Levin, F., 1978, Apparent attenuation due to intrabed multiples, II. Geophysics, 43: 730-737.
- Schubnel, A., Nishizawa, O., Masuda, K., Lei, X., Xue, Z. and Guégen, Y., 2003, Velocity measurements and crack density determination during wet triaxial experiments on Oshima and Toki granites. Pure and Applied Geophysics, 160: 869-887.
- Schubnel, A., Benson, P.M., Thompson, B.D., Hazzard, J.F. and Young, R.P., 2006, Quantifying damage, saturation and anisotropy in cracked rocks by inverting elastic wave velocities. Pure and Applied Geophysics, 163: 947-973.
- Sears, F. and Bonner, B., 1981, Ultrasonic attenuation measurement by spectral ratios utilizing signal processing techniques. IEEE Transactions on Geoscience and Remote Sensing, GE-19: 95-99.
- Seki, H., Granato, A. and Truell, R., 1956, Diffraction effects in the ultrasonic field of a piston source and their importance in the accurate measurement of attenuation. The Journal of the Acoustical Society of America, 28: 230-238.

- Simmons, G., 1964, Velocity of shear waves in rocks to 10 kilobars, 1. *Journal of Geophysical Research*, 69: 1123-1130.
- Soga, N., Mizutani, H., Spetzler, H. and Martin III, R., 1978, The effect of dilatancy on velocity anisotropy in Westerly granite. *Journal of Geophysical Research*, 83: 4451-4458.
- Solomon, S., 1973, Shear wave attenuation and melting beneath the Mid-Atlantic Ridge. *Journal of Geophysical Research*, 78: 6044-6059.
- Sondergeld, C.H. and Estey, L.H., 1981, Acoustic emission study of microfracturing during the cyclic loading of Westerly granite. *J. geophys. Res.*, 86: 2915-2924.
- Spencer, T., Sonnad, J. and Butler, T., 1982, Seismic Q—Stratigraphy or dissipation. *Geophysics*, 47: 16-24.
- Stewart, R., 1984, Q and the rise and fall of a seismic pulse. *Geophysical Journal of the Royal Astronomical Society*, 76: 793-805.
- Strassburger, E., 1982, Use of piezoelectric transducers for stiffness and density measurements of soils., M.S. Thesis, University of Texas
- Sukmono, S., Santoso, D., Samodra, A., Waluyo, W. and Tjiptoharsono, S., 2006, Integrating seismic attributes for reservoir characterization in Melandong Field, Indonesia. *The Leading Edge*, 25: 532.
- Szilard, J., 1982, Techniques using dry coupling or non-contact coupling. In: Szilard, J. (ed.), *In Ultrasonic testing*. John Wiley & Sons Ltd., New York. 381–409.
- Tao, G., King, M. and Nabi Bidhendi, M., 1995, Ultrasonic wave propagation in dry and brine saturated sandstones as a function of effective stress: laboratory measurements and modelling. *Geophysical Prospecting*, 43: 299-327.

- Tarif, P. and Bourbie, T., 1987, Experimental Comparison Between Spectral Ratio and Rise Time Techniques for Attenuation measurement. *Geophysical Prospecting*, 35: 668-680.
- Thompson, B., Young, R. and Lockner, D., 2006, Fracture in Westerly Granite under AE Feedback and Constant Strain Rate Loading: Nucleation, Quasi-static Propagation, and the Transition to Unstable Fracture Propagation. *Pure and Applied Geophysics*, 163: 995-1019.
- Toksöz, M., Johnston, D. and Timur, A., 1979, Attenuation of seismic waves in dry and saturated rocks: I. Laboratory measurements. *Geophysics*, 44: 681 - 690.
- Tutuncu, A.N., Podio, A.L., Gregory, A.R. and Sharma, M.M., 1998, Nonlinear viscoelastic behavior of sedimentary rocks, Part I: Effect of frequency and strain amplitude. *Geophysics*, 63: 184-194.
- Vanheerden, W.L., 1987, General Relations between Static and Dynamic Moduli of Rocks. *International Journal of Rock Mechanics and Mining Sciences & Geomechanics Abstracts*, 24: 381-385.
- VanValkenburg, H., 1983, Backing for ultrasonic transducer crystal. Automation Industries, Inc., Greenwich Conn. .
- Viggiani, G. and Atkinson, J., 1995a, Interpretation of bender element tests. *Géotechnique*, 45: 149–154.
- Viggiani, G. and Atkinson, J., 1995b, Stiffness of fine-grained soil at very small strains. *Géotechnique*, 45: 249-266.
- Walsh, J.B., 1965a, Effect of Cracks on Compressibility of Rock. *Journal of Geophysical Research*, 70: 381-&.
- Walsh, J.B., 1965b, The effect of cracks on the uniaxial elastic compression of rocks. *Journal of Geophysical Research*, 70: 399-411.

- Walsh, J.B., 1965c, The effect of cracks in rocks on Poisson's ratio. *Journal of Geophysical Research*, 70: 5249-5257.
- Walsh, J.B., 1966, Seismic wave attenuation in rock due to friction. *Journal of Geophysical Research*, 71: 2591-2599.
- Walsh, J.B., 1968, Attenuation in partially melted material. *Journal of Geophysical Research*, 73: 2209-2216.
- Walsh, J.B., 1969, New analysis of attenuation in partially melted rock. *Journal of Geophysical Research*, 74: 4333-4337.
- Walsh, J.B. and Brace, W.F., 1972, Elasticity of rock in uniaxial strain. *International Journal of Rock Mechanics and Mining Sciences & Geomechanics Abstracts*, 9: 7-15.
- Wang, Q. and Ji, S., 2009, Poisson's ratios of crystalline rocks as a function of hydrostatic confining pressure. *Journal of Geophysical Research*, 114: 1-21.
- Wang, Z., 2000, Dynamic versus static elastic properties of reservoir rocks. . *Society of Exploration Geophysicists: Seismic and acoustic velocities in reservoir rocks*, 3: 531 – 539.
- Wasley, R.J., 1973, *Stress wave propagation in solids*. Marcel Dekker, Inc., New York
- Wulff, A., Hashida, T., Watanabe, K. and Takahashi, H., 1999, Attenuation behaviour of tuffaceous sandstone and granite during microfracturing. *Geophysical Journal International*, 139: 395-409.
- Xu, S. and King, M., 1990, Attenuation of elastic waves in a cracked solid. *Geophysical Journal International*, 101: 169-180.
- Zhang, B.C., Hong, L.I., Li, F.Q. and Koichi, S., 1998, Kaiser effect tests on orientated rock core. *Series on rock and soil mechanics*: 211-224.

Zimmerman, R.W., 1985, The effect of microcracks on the elastic moduli of brittle materials. *Journal of materials science letters*, 4: 1457-1460.

Zisman, W.A., 1933, Comparison of the statically and seismologically determined elastic constants of rocks. *Proceedings of the National Academy of Sciences of the United States of America*, 19: 680-686.

8 Appendix

8.1 Electronic copy of labview program used to display and process the recorded P and S wave data.

The program was made using Labview version 8.5 and can perform the following tasks (version 2):

(1) For velocity

- View P and S data file that has a .csv extension and 2 arrays (2 columns – time and voltage).
- Pick time of flight and amplitude (voltage) level of P and S wave using the crosshairs.

(2) For Attenuation

- Apply a Hanning window to the P and S wave data.
- Select the portion of data that is of interest by using the crosshairs (the time of flight from the yellow crosshair must be less than that from the red crosshair).
- Perform FFT **only** on the selected data.
- Display frequency and phase spectrum of selected data.
- Output unfiltered frequency spectrum data to file
 - Data file must be saved with a .csv extension

(3) For filtering

- Apply a Hanning window to the P and S wave data.
- Select the portion of data that is of interest by using the crosshairs (the time of flight from the yellow crosshair must be less than that from the red crosshair).
- Filter data using the Butterworth filter (High Pass, Low pass, and band width)
 - The data is filtered then reversed and filter again (to remove the time delay in filtered data (Li and Nakagawa, 1997))
- Display frequency and phase spectrum of selected data.

- Display frequency and phase data of filtered data

A simpler version of the labview program is also available (version 1) that can only perform the following tasks:

- View P and S data file that has a .csv extension and 2 arrays (2 columns – time and voltage).
- Pick time of flight and amplitude (voltage) level of P and S wave using the crosshairs.
- Filter data using the Butterworth filter (High Pass, Low pass, and band width)
 - Data windowed by the use of Hanning window
 - The data is filtered then reversed and filter again (to remove the time delay in filtered data (Li and Nakagawa, 1997))
- Display frequency and phase spectrum of selected data
- Display frequency and Phase data of filtered data

Labview 8.5 should be installed before using this program.

8.2 Electronic copy of 'isf to csv' conversion script.

This program is used to convert the P and S wave data that is saved from the oscilloscope in a .isf extension to a .csv extension. The follow command should be executed in MS-Dos:

```
cnvrtwfm -l -8- myfile.isf
```

Executing this command will generate a file called myfile.csv

It is highly recommended to use a batch file for numerous data files. An example of a batch file is shown in Figure 7.1. The batch file and files to be converted must be placed in the same folder as the 'isf to csv' script when being executed.

```
@echo off
cnvrtwfm -l -8- p-p-M10-25.isf
cnvrtwfm -l -8- p-p-M10-50.isf
cnvrtwfm -l -8- p-p-M10-70.isf
cnvrtwfm -l -8- p-s-M10-25.isf
cnvrtwfm -l -8- p-s-M10-50.isf
cnvrtwfm -l -8- p-s-M10-70.isf
cnvrtwfm -l -8- s-p-M10-25.isf
cnvrtwfm -l -8- s-p-M10-50.isf
cnvrtwfm -l -8- s-p-M10-70.isf
cnvrtwfm -l -8- s-s-M10-25.isf
cnvrtwfm -l -8- s-s-M10-50.isf
cnvrtwfm -l -8- s-s-M10-70.isf
```

Figure 8-1. Example of a batch file. A text editor (Notepad or Wordpad in Windows) can be used to create the batch file. The file extension of the file should be saved as .bat.